Investigation of Supersonic Gas Flows into Nanochannels Using an Unstructured 3D Direct Simulation Monte Carlo Method

By
Wael G. Al-Kouz
A Dissertation
Submitted to the Faculty of
WORCESTER POLYTECHNIC INSTITUTE
in partial fulfillment of the requirement for the degree of
Doctor of Philosophy
In
Mechanical Engineering
By
Wael G. Al-Kouz
June 2009

APPROVED:

Nikolaos A. Gatsonis
Dr. Nikolaos A. Gatsonis, Advisor
Professor, Mechanical Engineering Department

Dr. John J. Blandino, Committee Member
Associate Professor, Mechanical Engineering Department

Dr. Gretar Tryggvason, Committee Member
Professor, Mechanical Engineering Department

Dr. Nicolas G. Hadjiconstantinou, Committee Member
Associate Professor, Department of Mechanical Engineering,
Massachusetts Institute of Technology, Cambridge

Cosme Furlong
Dr. Cosme Furlong, Graduate Committee Representative
Associate Professor, Mechanical Engineering Department

ABSTRACT

This dissertation is devoted to the computational investigation of supersonic gas flows in rectangular nanochannels with scales between 100 nm and 1000 nm, using an unstructured three-dimensional Direct Simulation Monte Carlo (U3DSMC) methodology. This dissertation also contributes to the computational mathematics background of the U3DSMC method with validations and verifications at the micronscale and nanoscale, as well as with the investigation of the statistical fluctuations and errors associated with U3DSMC simulations at the nanoscale.

The U3DSMC code is validated by comparisons with previous two dimensional DSMC simulations of flows in micron-scale rectangular channels. The simulation involves the supersonic flow of nitrogen into a microchannel with height of 1.2 μm and width of 6 μm. The free stream conditions correspond to a pressure of 72,450 Pa, Mach number $M_\infty = 4.15$, Knudsen number $Kn = 0.062$ and mean free path $\lambda_\infty = 74.4$ nm. The U3DSMC centerline temperature, heat flux to the wall, and mean velocity as a function of the transverse direction are in very good agreement with previous 2D results.

Statistical fluctuations and errors in U3DSMC have added significance in nanoscale domains because the number of real particles can be very small inside a computational cell. The effect of the number of samples, the number of computational particles in a Delaunay cell, and the Mach number on the fractional errors of density, velocity and temperature are investigated for uniform and pressure-driven nanoscale flows. The uniform nanoflow is implemented by applying a $M_\infty = 0.1$ and $M_\infty = 10$ free stream boundary condition with $n_\infty = 2.69 \times 10^{25}$ m^{-3}, $T_\infty = 273$ K, $\lambda_\infty = 48.1$ nm in a domain that requires resolution of a characteristic length scale $L = 50$ nm. The pressure-driven flows consider a nanochannel of 500 nm height, 100 nm width and 4 μm length. Subsonic boundary conditions are applied with inlet pressure 101,325 Pa and outlet pressure of 10132.5 Pa. The analysis shows that U3DSMC simulations at nanoscales featuring 10-30 particles per Delaunay cell result in statistical errors that are consistent with theoretical estimates.

The rarefied flow of nitrogen with speed ratio of $S_\infty = 2$, 5, and 10, pressure of 10.132 kPa into rectangular nanochannels with height of 100, 500 and 1000 nm is investigated using U3DSMC. The investigation considers rarefaction effects with Kn =0.481, 0.962, 4.81, geometric effects with nanochannel aspect ratios of (*L*/*H*) from AR=1, 10, 100 and back-pressure effects with imposed pressures from 0 to 200 kPa. The computational domain features a buffer region upstream of the inlet and the nanochannel walls are assumed to be diffusively reflecting at the free stream temperature of 273 K. The analysis is based on the phase space distributions as well as macroscopic flow variables sampled in cells along the centerline. The phase space distributions show the formation of a disturbance region ahead of the inlet due to slow particles backstreaming through the inlet and the formation of a density enhancement with its maximum inside the nanochannel. The velocity phase-space distributions show a low-speed particle population generated inside the nanochannel due to wall collisions which is superimposed with the free stream high-speed population. The mean velocity decreases, while the number density increases in the buffer region. The translational temperature increases in the buffer region and reaches its maximum near the inlet. For AR=10 and 100 nanochannels the gas reaches near equilibrium with the wall temperature. The heat transfer rate is largest near the inlet region where non-equilibrium effects are dominant. For Kn=0.481, 0.962, 4.81, vacuum back pressure, and AR=1, the nanoflow is supersonic throughout the nanochannel, while for AR=10 and 100, the nanoflow is subsonic at the inlet and becomes sonic at the outlet. For Kn=0.962, AR=1, and imposed back pressure of 120 kPa and 200 kPa, the nanoflow becomes subsonic at the outlet. For Kn=0.962 and AR=10, the outlet pressure nearly matches the imposed back pressure with the nanoflow becoming sonic at 40 kPa and subsonic at 100 kPa. Heat transfer rates at the inlet and mass flow rates at the outlet are in good agreement with those obtained from theoretical free-molecular models. The flows in these nanochannels share qualitative characteristics found in microchannels ad well as continuum compressible flows in channels with friction and heat loss.

The rarefied flow of nitrogen with speed ratio of $S_\infty = 2$, 5, 10, at an atmospheric pressure of 101.32 kPa into rectangular nanochannels with height of 100 and 500 nm is investigated using U3DSMC. The investigation considers rarefaction effects with Kn=0.0962 and 4.81, geometric effects with nanochannel aspect ratios of (*L*/*H*) of AR=1 and 10 and vacuum back-pressure. Phase plots and sample-averaged macroscopic parameters are used in the analysis. Under vacuum back pressure the centerline velocity decreases in the buffer region from its free stream value. For $Kn_\infty = 0.481$, 0.0962 and AR=1 the Mach number is supersonic at the inlet and remains supersonic throughout the nanochannel. For $Kn_\infty = 0.481$, 0.0962 and AR=10, the flow becomes subsonic at the inlet and shows a sharp increase in pressure. The Mach number, subsequently, increases and reaches the sonic point at the outlet. For $Kn_\infty = 0.481$, 0.0962 and AR=1 the translational temperature reaches a maximum near the inlet and decreases monotonically up to the outlet. For $Kn_\infty = 0.481$, 0.0962 and AR=10, the translational temperature reaches a maximum near the inlet and then decreases to come in near equilibration with the wall temperature of 273 K.

ACKNOWLEDGEMENTS

Praise is Due to Allah, the Beneficent, the Merciful. First and foremost, I would like to thank God for his help and blessings that He has bestowed not only through the period of my graduate studies but also throughout my entire life.

I would like to express my sincerest appreciation to my advisor, Professor Gatsonis. I have learned a lot from him through the years that I had spent at the Computational Gas and Plasma Dynamics laboratory (CGPL). Professor Gatsonis had shaped me in a way so that engineering and scientific inquiry has become a central part of my thinking. I have learned a lot from him not only regarding technical and scientific issues but also regarding professional issues, and regarding life overall. I feel that through the years, he has also become “an older brother” for me. I would like to thank him for his help, advice, and support.

I would like to thank the members of my committee for their time, patience, and expertise. Their feedback and recommendations have strengthened my work as well as my understanding.

I also would like to thank my friends throughout the years that I had spent at WPI, Ryan Chamberlin, James Partridge, Anton Spirkin, Raffaele Potami, Sangheum Kim, Wael El Khateb, Conn Dickson, Elie Karam and Jeff Court. The time we spent together will become memories that will never be forgotten.

I would like to thank my professors back in Jordan, Prof. Mohammad Al-Nimr, Prof. Montasir Hader and Prof. Osama Haddad for their support and encouragement.

I also would like to thank Prof. Hassan from Concordia University in Canada for his help and encouragement.

Gratitude is extended to the Mechanical Engineering Department, and specially to Barbara Edilberti, Barbara Furhman and Pam St. Louis.

I would like to thank Sia Najafi and Randy Robertson for their expertise, continued support and endless patience with the Linux system as well as the code problems and errors.

I would like to thank all of my teachers back in Jordan, and especially those in the United Nations (UN) schools.

Special thanks go to my family. Their continued love, support, and admiration are empowering. From my parents, I learned the value of education both from their instruction and influence. I will never forget the time my mother spent teaching and helping me with homework while in the elementary school. My success is a reflection of their hard work and sacrifice. I thank them for all that I am and all that they have done for me.

I would like to thank my brothers and sisters, Lana, Nael, Mohammad, Rania, Maha, Reem, Mohannad and Amr as well as my brothers in law, Sulaiman, Mahmoud and Mustafa for their encouragement and care.

Very special thanks go to my brother in law, Dr. Essam Shihadeh for his continuous help and support throughout the years that I had spent at WPI.

Most importantly, I would like to thank my wife, Dr. Ferial Shihadeh for her help, support, encouragement, patience and endless love. This work will not have been possible without her and my love for her will be there forever.

This work was partially supported by AFOSR’s Computational Mathematics Program through Grant FA9550-06-1-0236. I would also like to acknowledge the support obtained through Teaching Assistantships obtained from the Mechanical Engineering Department at WPI.

This work is dedicated to my wife, kid, mother, father, brothers and sisters.

Table of Contents

LIST OF FIGURES

LIST OF TABLES

NOMENCLATURE

Boldface denotes a vector. The magnitude of a vector is denoted using the same symbol as the vector, but without boldface. Duplicate use of a symbol, or usage not defined below, will be clarified within the text.

a	Sound speed
A	Surface area
c_s	Thermal velocity of the specie based on the mass-average drift velocity
c_s^*	Thermal velocity of the specie based on the specie average drift velocity
$\bar{c}$	Mean square molecular speed
c_s^m	Most probable speed
d	molecular diameter
E	Statistical error
f	Distribution function
F_N	Particle numerical weight
G_D	Number of Delaunay tetrahedral cells
H	Height of the nanochannel
k, k_B	Boltzmann constant
Kn	Knudsen number
L	Characteristic length
L_B	Buffer region length
m	Mass of molecule
M, Ma	Mach number
M	Number of samples
n	Number density
$\mathbf{n}$	Normal vector
N_D	number of computational particles in the Delaunay cell

N_d	Number of computational particles in the super Delaunay cell
$\dot{N}$	Number flux
N_D	Number of real particles in the Delaunay cell
p	pressure
q	Heat flux
$\mathbf{r}$	Position vector
R	Gas constant
Re	Reynolds number
S	Speed Ratio
s	Specie
T	Temperature
V_∞	Free stream speed
v	Molecular velocity
V	Mass-average drift velocity
V_s	Thermal velocity
W_s	Diffusion specie velocity
w	Characteristic variable
W	Characteristic vector
β	Reciprocal of most probable speed
$\Delta\tau$	Elapsed time (time step)
τ_{coll}, τ	Mean collision time
Γ_d	Voronoi volume
ε	Diffuse fraction
λ	Mean free path
Ω_D	Delaunay cell volume
Ω_d	Super Delaunay cell volume
ρ	Number density

σ_T	Total collision cross section
σ	Standard Deviation
δ	Mean molecular spacing
υ_o	Mean collision rate
κ_T	Isothermal compressibility
γ	Specific heat ratio
ε	Percentage of having a fully diffuse reflection.

1 INTRODUCTION

Microscale gaseous flows with characteristic lengths of greater than 1 μm and less than 1 mm are found in a wide range of microfluidic systems. Examples include sensors, actuators, flow control devices, pumps, valves, power devices, spacecraft propulsion devices, drug delivery devices, microfiltration devices. Applications are found in biomedical, environmental areas, aeronautical, and space areas. (Karniadakis and Beskok, 2003; Karniadakis *et al*., 2005; Liou and Fang, 2005; Gad-el-Hak, 2002). The proliferation and advances in MEMS (Micro Electromechanical Systems) and the emergence of NEMS (Nano Electromechanical Systems) open new applications at the nanoscales which are below 1 μm. While there have been great advances in the study of microscale gaseous flows, our understanding and prediction ability of nanoscale flows is more limited and the reasons behind that will be discussed in details in later sections of this dissertation. The goal of this work is to contribute to the understanding of rarefied supersonic gas flows into nanochannels, a geometry found in many MEMS and proposed NEMS devices.

Micro and nanoscale flows are characterized through the use of the dimensionless Knudsen number (Kn), this number which is the ratio of the mean free path (λ) to the characteristic length (L) of the geometry of interest is a measure of the degree of rarefaction of the fluid.

The mean free path for the simple hard-sphere collision model is given in terms of the number density (n), molecular diameter (d) of the fluid as (Sec. 4.3, Bird, 1994)

$$\lambda = \frac{1}{\sqrt{2}\pi d^2 n} \tag{1.1}$$

The Knudsen number can also be related to the Mach number (M) and Reynolds number (Re) by

$$Kn = \frac{\lambda}{L} = \sqrt{\frac{\gamma\pi}{2}}\frac{M}{\mathrm{Re}} \tag{1.2}$$

where

$$M = V \Big/ \sqrt{\frac{\gamma k T}{m}} \tag{1.3}$$

where γ is the specific heat ratio.

The speed ratio is defined as

$$S = V \Big/ \sqrt{\frac{2kT}{m}} \tag{1.4}$$

The Knudsen number physically represents an indication of the degree of rarefaction of the gas of interest. Based on the Knudsen number, the respective flow regimes can be classified (Schaaf and Chambre, 1961; Cercignani and Lampis, 1974) according to:

$Kn < 0.01$	Continuum Flow
$0.01 < Kn < 0.1$	Slip Flow
$0.1 < Kn < 10$	Transitional Flow
$10 < Kn$	Free-Molecular Flow

For the continuum and slip flows, one can use Navier-Stokes equations to solve for the physics of the flow. In the slip flows, the slip boundary condition is applied at the surfaces, Also if there is a temperature jump at the surface, then this condition is utilized as a boundary condition at the surface of interest.

Figure 1-1 plots the mean free path (λ) as a function of the number density (n) for different gases, Helium, Argon and Krypton where the standard number density is $n_0 = 2.69 \times 10^{25}$ m^{-3}. The figure shows that as the number density is increasing then the mean free path is decreasing. It shows also, that when the molecular diameter is increasing (maximum for krypton and minimum for helium), then the mean free path is decreasing for the same number density.

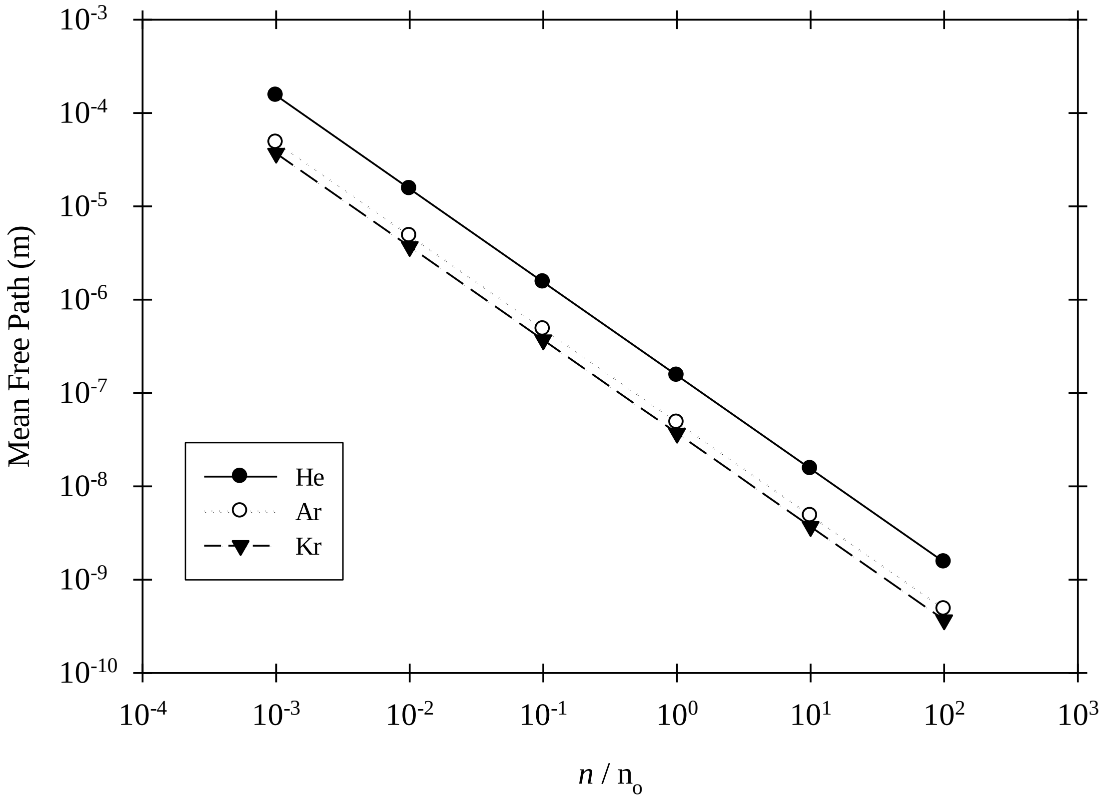

Figure 1-1. Mean free path as a function of the number density for different gases.

The range of validity of continuum based modeling is plotted in Figure 1-2. This figure also shows the dilute gas limit where the ratio of the mean molecular spacing (δ) to the molecular diameter (d) is greater than 7. It also shows the region of significant statistical fluctuations. For many gaseous flows occurring in MEMS and NEMS, the Knudsen number is in the range of 0.1 to 10. As a result, the typical continuum based fluid modeling tools, based on solving the Navier-Stokes equations cannot be used for modeling such rarefied flow regimes.

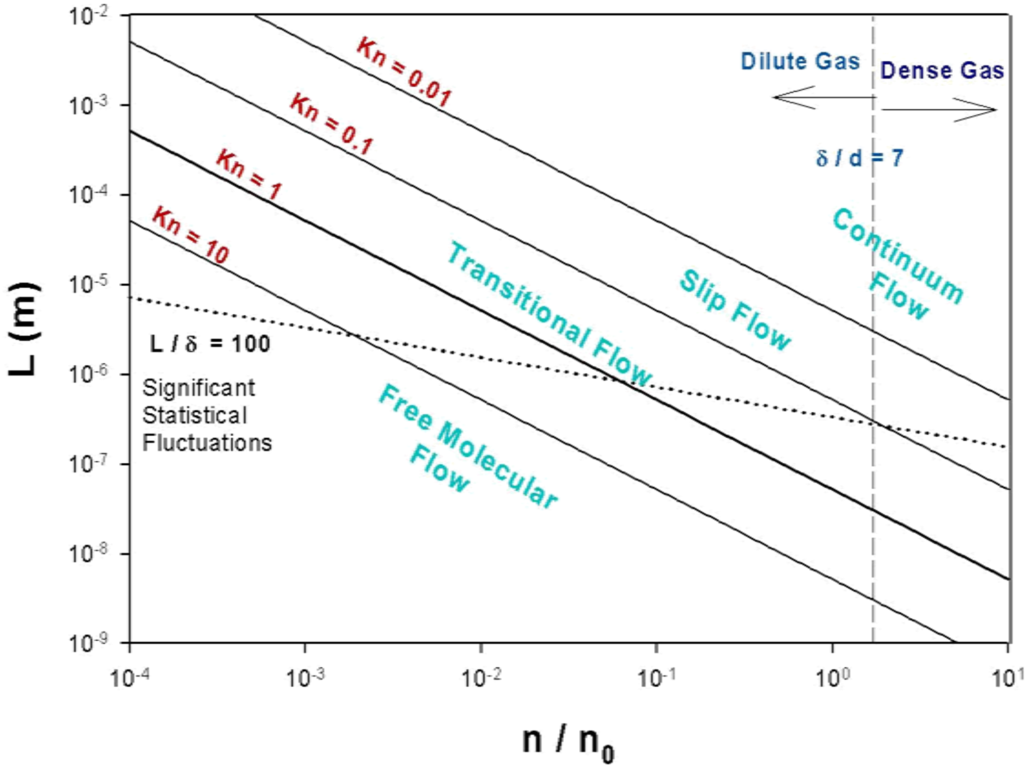

Figure 1-2. Flow regimes for various Knudsen numbers. $n_0 = 2.68 \times 10^{25} m^{-3}$ for ideal gas at T=273 K (adapted from Chamberlin, 2007).

The Direct Simulation Monte Carlo (DSMC) method introduced by Bird (Bird, 1994) is widely used to simulate gas flows in microscale domains (Karniadakis *et al.*, 2003; Liou and Fang, 2005). To improve the modeling ability of complex devices an unstructured three-dimensional DSMC method has been developed (Chamberlin, 2007; Gatsonis and Spirkin, 2009).

The methodology has been implemented in a code (U3DSMC) and has been applied to the study of micronozzles (Hammel *et al*., 2001; Chamberlin and Gatsonis, 2007), micropitot tubes in rarefied flows (Chamberlin and Gatsonis, 2006), and to flows through microtubes (Chamberlin and Gatsonis, 2008). There are two primary goals in this work:

First, to investigate the supersonic flows incoming into sub-micron channels by applying the U3DSMC method and thus, extend the applicability of Bird's (Bird, 1994) DSMC approach as implemented in U3DSMC, to nanoscale domains with scales between 100 nm-1000 nm;

Second, to contribute to the computational mathematics background of U3DSMC method by validating the U3DSMC and by investigating the statistical fluctuations and errors associated with this unstructured DSMC approach at the micron/nanoscale.

1.1 Review of Supersonic Microflows

Rarefied supersonic flows through channels and tubes has been studied analytically (Clausing, 1932; Hughes and De Leeuw, 1965), and computationally using DSMC due to its importance in many technical applications (Moss and Bird, 1988; Kannenberg and Boyd, 1996; Gatsonis *et al.*, 1997; Kannenberg and Boyd, 1999; Wu *et al.*, 2002; Gatsonis *et al*., 2003; Wang and Li, 2004). For microchannels the two dimensional DSMC computations so far have addressed the slip to transitional regimes for nitrogen and helium gases (Oh *et al*., 1997; Mavriplis *et al*, 1997, Liou and Fang, 2001; Le and Hassan, 2007; Le *et al*., 2007). The review of literature of rarefied supersonic flows into micro and small-scale channels shows that the internal flow into a microchannel with height H and length L, is affected by the rarefaction and compressibility effects (Knudsen number); geometric effects (aspect ratio $\mathrm{AR} = H/L$), the wall temperature, the nature of reflection; and the boundary conditions at the inlet and the exit (back pressure). The following review summarizes the literature along these findings.

Oh *et al.* (1997) considered the $M_{\infty} = 5$ flow of Helium gas at 1 atm with $n = 2.456 \times 10^{25}\,\mathrm{m}^{-3}$, $T_{\infty} = 298$ K into two dimensional microchannels with $H =$0.88-2.4 μm and AR=5. Knudsen numbers were 0.07, 0.14 and 0.19 covering the slip and early translational regimes. The computational domain used in the simulations consists of the buffer region ahead of the microchannel in which the walls are assumed to be of specular reflection while the microchannel walls are assumed to be of a diffuse type of reflection with a full thermal accommodation factor and the wall temperature assumed to be the same as the temperature of the free stream ($T_{w} = 298$ K). The 2D DSMC method was combined with the monotonic Lagrangian grid data structure. The outflow boundary conditions were treated using virtual templates and particles, with prescribed back pressure, allowing for supersonic or subsonic exit conditions. Simulations provide pressure, temperature, and Mach number distributions that show the interactions among the oblique shocks and the boundary layer. The flow behavior is found to be similar to a Fanno flow. The slip velocities are increased with increasing Kn and is approximately constant behind the shock. The temperature jump is reduced after the shock.

Mavriplis *et al.* (1997), considered the $M_{\infty} =$ 4.03 of nitrogen with $n_{\infty} = 1.75 \times 10^{20}$-$7 \times 10^{22}\,\mathrm{m}^{-3}$ and $T_{\infty} =$300 K into 2D microchannels with $H =$0.26-104 μm and AR=2.5. The Kn were 0.00462-0.01849 covering the slip regime.

Mavriplis *et al.* (1997) had embedded the microchannels inside a large simulation domain and applied the free stream conditions far from the inlet. The microchannel walls considered to be of a diffuse type of reflection with a full thermal accommodation factor with

$T_\infty = T_w = 300$ K. The heat transfer as well as the flow fields inside and outside the microchannel were investigated using the DSMC method. In the study, Knudsen number effects are very obvious on the evolution of the flow fields along the channel as well as on the heat transfer to the wall of the microchannel. The results were in qualitative agreement with other computational and experimental results. A very good agreement is seen between the results from the simulations near the continuum limit and the classical theories, such as Fanno/Rayleigh flow and boundary layer interactions with shocks. It has been also shown that the heat fluxes at the channel surface depend on the length of the channel as well. It has been found that as the Knudsen number increases the shock broadens and the heat flux decreases monotonically along the channel wall, with the flow becoming subsonic in the channel. They also found that the pressure at the inlet increases with increasing the Knudsen number. The simulation results also show that by increasing the channel length then the flow inside the channel becomes subsonic and the heat transfer through the channel wall will decrease monotonically. The inlet pressure to the channel will also increase as the channel length increases because of increasing the retarding force.

Liou and Fang (2001), considered the $M_\infty =$ 4.15 flow of nitrogen with $n = 1.75 \times 10^{25}$ and $T_\infty =$300 K into 2D microchannels with $H =$0.4 -2.4 μm and AR=5. The Kn were in the range of 0.031-0.186 covering the slip and the early transitional regimes. The 2D DSMC simulations utilized a computational domain that includes a buffer region of specular solid walls in front of the microchannel in order to achieve supersonic conditions at the inlet. The microchannel walls were assumed to be of a diffuse type with a full thermal accommodation factor and T_w=323 K. At the exit of the microchannels that were studied, a vacuum pressure boundary condition was applied so that the exiting particles from the domain will not come back again. The results show that as Knudsen number is increases, both the temperature jump at the wall and the heat transfer to the isothermal wall increase.

The 2D DSMC simulations carried out by Le and Hassan (2006) studied flows of nitrogen at $n_\infty = 1.75 \times 10^{25}$ m^{-3}or helium $n_\infty = 3.569 \times 10^{25}$ m^{-3}, at $M_\infty =$ 4.15 into microchannels with $H =$0.1-1.2 μm and AR=5. The Kn were in the range of 0.062-0.744. The temperature of the free stream T_∞ was either 300 or 350 K and the wall temperature of the microchannel was $T_w = 323$ K. In order to generate the free stream boundary conditions at the inlet, the computational domain includes a buffer region with specularly reflecting walls and the microchannel walls are considered to be of a diffuse reflection with a full thermal accommodation factor. A vacuum pressure was imposed at the exit of the channels that were studied, therefore not allowing particles that leave the domain to enter again. The results show that viscous effects produced by varying the Knudsen number influence the development of both the flow and thermal boundary layers. The bulk flow has a high temperature due to the wall friction and shows a deceleration as it enters the narrow channels. The results show that the species affects the flow and heat transfer rates. For the case of helium flow, the centerline temperature, temperature jump at the wall and the heat flux to the wall are higher than those of nitrogen flow. It had also been shown that by varying the wall temperature from 323 to 350 K, there will no significant effects on the amount of heat transfer between the bulk flow and the channel walls.

Le *et al*. (2007) expanded their previous investigation using 2D microchannels with $H =$ 1 μm, $H =$1.2 μm with AR of 5 or 10. They studied flows of nitrogen at $n_\infty = 1.75 \times 10^{25}$ m^{-3} or Helium $n_\infty = 3.569 \times 10^{25}$ m^{-3}, at M_∞ of 3.39 and 4.15. The free stream temperature

$T_\infty = 300\,\mathrm{K}$ while the wall temperature T_w was varied from 300-353 K in order to study the heat transfer rates. In their investigation, the effects of the outlet pressure boundary conditions were accounted for by implementing a characteristics-based method developed by Nance *et al*., (1997). It was found that the finite pressures at the outlet are more physical than the vacuum pressure. These incoming supersonic flows showed features similar to a Fanno flow. For the $M_\infty = 4.15$ case the increase in back pressure affects the flow inside the microchannel, it was found that when the back pressure is increasing then the pressure inside the microchannel will increase and will match the back pressure at the exit of the microchannel and the flow will be subsonic, also the temperature increases at a given location when increasing the back pressure, the reason behind that is the energy conservation in which the kinetic energy is converted to internal thermal energy and the flow will decelerate due to the wall friction and results in an increased heat flux. The $M_\infty = 3.39$ flow results in smaller heat flux to the wall. The DSMC using a variable wall temperature carried out by this study show that there is no significant impact on the heat transfer rates to the wall of the microchannel for the two types of gases that were used in the simulations, the single atomic and the diatomic gases, namely nitrogen and helium.

An important aspect in DSMC simulation of microchannel flows involves the implementation of the inlet and outlet boundary conditions. In rarefied flows through channels there exist molecules that exit the channel's inlet and propagate upstream. Such molecules constitute a population with a distribution that can be very distinct from the incoming population. The flow field outside the channel becomes therefore the superposition of the incoming and the outgoing through the inlet flow. The DSMC simulations of (Oh *et al*., (1997); Liou and Fang, (2001); Le and Hassan, (2006)) so far have implemented a buffer region of specular reflecting walls as shown in Figure 1-3. On the left, such an implementation has the potential to generate near supersonic conditions at the inlet but limits the physical realization. The implementation found in Mavriplis *et al*. (1997) provides a more physical realization where the microchannel is embedded in the flow fields as shown in Figure 1-3 on the right, and the conditions at the inlet are allowed to develop. The boundary condition at the outlet has been shown to affect drastically a flow in a microchannel. A vacuum boundary in a DSMC simulation does not allow molecules to enter the domain through the outlet and is easy to implement (Liou and Fang, 2001; Le and Hassan, 2006; Le *et al*, 2007). Finite pressure at an outlet provides a more physical realization and has been implemented in various forms. In Oh *et al*. (1997), the outflow boundary conditions was treated using virtual templates and particles, while Le *et al*. (2007), had made use of the theory of characteristics to treat the boundary conditions at the exit.

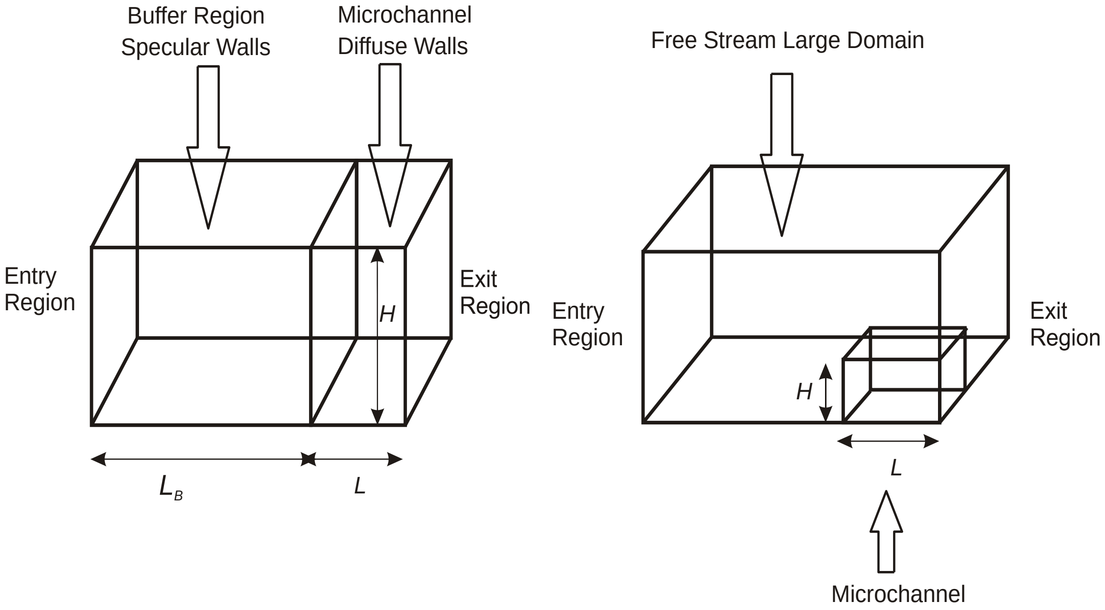

Figure 1-3. Typical computational domain in 2D DSMC simulations (Left): (Oh *et al*., (1997), Liou and Fang, (2001), Le and Hassan, (2006)), (Right): Mavriplis *et al*., (1997)

While there are outstanding issues in DSMC simulation of supersonic rarefied gaseous flows into microchannels, our review shows that there is a good understanding of the flow phenomena at the macro- and micro-scales.

The goal of this dissertation is to provide a comprehensive insight on supersonic rarefied flows into nanoscale channels and extend the applicability of the 3D DSMC method to nanoscales by implementing an unstructured three dimensional direct simulation Monte Carlo methodology (U3DSMC).

1.2 Review for the Statistical Fluctuations in DSMC

The role of fluctuations and statistical errors in DSMC has been addressed since the early applications of the method (Sec. 1.4, Bird, 1994). The errors in DSMC are influenced by the physical parameters such as the Knudsen number, speed ratio (or Mach number) as well as computational parameters such a time step, scale of cell, and particle weight. We review below recent work involving primarily DSMC implementations on structured rectangular grids to summarize the current understanding covering both low- and high-speed flow regimes.

Mansour *et al*. (1987) studied the hydrodynamic fluctuations in a dilute gas subjected to a constant heat flux using the DSMC method and the Landau-Lifshitz theory. Good agreement was demonstrated between the theory and the DSMC results. The hydrodynamic fluctuation equations proposed are valid for length scales of few mean free paths even in the presence of strong non-equilibrium constraints.

Chen and Boyd (1996) studied the statistical error associated with the DSMC method for non-equilibrium hypersonic and nozzle flows. They utilized the root mean square (rms) error to measure the fluctuations. They found that there is a limit on the minimum number of the particles in the domain in order to model it adequately. The effects of the time step as well as the type of collision on the statistical error were analyzed.

In the work by Alexander *et al*. (1998), the effects of the cell size on error associated with the DSMC method have been investigated. They used the planar Couette flow problem and found that by increasing the cell size, the error associated with the normalized transverse momentum flux decreases.

Garcia and Wagner (2000) investigated the effects of time step on the statistical error associated with the DSMC methodology. In their DSMC simulations, the domain considered was 2D rectangular channel with periodic boundary condition in the z direction. The boundary conditions imposed are those of a planar Couette flow with specified velocities, the heat with specified wall temperatures or the tagged-particle diffusion. The truncation error in wall drag force and parallel momentum flux was found to increase by increasing the time step. The authors evaluated the fluid velocity as well as the temperature and found that the error is increased by increasing the time step.

Hadjiconstantinou *et al*. (2003) studied the statistical fluctuations associated with the DSMC computation for dilute gases and the molecular dynamics computation for fluids. They investigated the effects of the number of particles in a DSMC cell, sample size, and Mach number on the statistical fractional errors of sampled flow properties such as temperature, density, velocity and the pressure. They investigation involved the simulation of Poisuelle flow of argon into 2D microchannels. They also provided comparisons between the DSMC fluctuations and estimates obtained through statistical mechanics. The results show that there is good agreement between the theoretical and the DSMC fractional errors. The investigation involved also the simulation of Couette flow of argon into 2D microchannels and the evaluation of the statistical error for fluxal quantities, such as the shear stress and the heat flux. They found that the statistical error from the DSMC is in agreement with the theoretical error. The results show that the statistical error in the shear stress is directly proportional to the statistical error in the velocity and the statistical error in the heat flux is directly proportional to the statistical error in the temperature. The results show also that the statistical errors associated with the fluxal quantities are inversely proportional to the Knudsen number of the flows.

Tysanner and Garcia (2004) evaluated the mean and the statistical error of fluid velocity in molecular simulations such as DSMC method. They used two different schemes to calculate this bias. In the sample average measurement (SAM) method, the mean fluid properties are computed by measuring the particle mean property in a cell and averaging over samples. In the cumulative average method (CAM) method, the mean fluid properties are computed by evaluating the cumulative property over all particles in a cell over all samples, then dividing this cumulative total by the cumulative number of the particles in the cell. Tysanner and Garcia (2003) obtained an analytical expression for predicting the bias and identified computational parameters, such as number of particles per cell, that can increase or reduce the error. In their simulations, they used a monatomic gas in a simple closed system bounded by thermal walls in the x-direction with periodic boundaries in the y and z directions. The temperature and y-velocity was specified on the left and the right walls and they were different on the sides. By altering the temperature difference or y-velocity component of the walls they investigated their effect on the SAM or CAM calculated mean velocity. The results show that as the differences in the temperature or the velocity are increasing, the error of the mean fluid velocity increases. Tysanner and Garcia (2003) studied the effects of the sampling size and found that by increasing the sampling size then the error in the mean fluid velocity decreases.

Shen *et al*. (2003) studied the effect of the time step on the mass flux and the pressure evolution obtained by the information-preservation DSMC simulation of rarefied gas flow through three dimensional microchannels. The simulation used parameters based on microchannels experiments of Pong *et al*. (1994), Shih *et al*. (1996), Arkilic *et al*. (1997) and Arkilic (1997). They investigated nitrogen, helium and argon flows where the inlet pressure $P_\infty = 1.01 \times 10^5$ Pa for the case of comparison with Pong *et al*. (1994) and Arkilic *et al*. (1997), $P_\infty = 1.0 \times 10^5$ Pa for the case of comparison with Shih *et al*. (1996), and $P_\infty = 6.5 \times 10^3$ Pa for the case compared to Arkilic (1997). The microchannels simulated have heights of 1.2 or 1.33 μm, widths of 40 or 52.3 μm with length varied from 3000-7490 μm. The resulting Knudsen number are in the range of 0.05-2. The walls of the microchannels were specified as either fully diffuse or partially diffuse reflection. Comparisons of the DSMC results with those from Navier Stokes with slip solvers show good agreement. The results shows that low-speed flows in long microchannels require large sample sizes in order to reduce the statistical error and present difficulty of regulating the subsonic boundary conditions at the inlet and outlet.

In Baker and Hadjiconstantinou (2005), a variance reduction method for the Monte Carlo simulations is proposed for flows with very low Mach number, $M_\infty \ll 1$. They show that by considering the deviation from equilibrium, significant computational savings can be obtained in the DSMC implementation for low-speed flows. The advantage of the variance reduction is that the relative statistical uncertainty in the flow velocity is almost constant for the cases where the M is very small and this uncertainty is much smaller than the one obtained from typical DSMC results. The implementation involved pressure driven and the unsteady Couette flow problems.

Garcia (2006) estimated the hydrodynamic quantities such as the number density, velocity, temperature and the pressure in the presence of microscopic fluctuations. A DSMC study for dilute gas argon flow in a 2D microchannel using structured grids where the left and right walls are of different temperatures was performed. In the study, the number of particles was changed for two different scenarios and the DSMC results found to be in good agreement with the analytical theory both at the thermal equilibrium and non equilibrium steady state cases.

The review of these recent works, and the numerous references within them, shows that the study of fluctuations covers comprehensively various forms of DSMC implementations in rarefied gas flows. There is need for study of statistical fluctuations and errors in unstructured, 3D DSMC computations and particularly, those covering the nanoscale flow regimes.

1.3 Computational Issues of DSMC Application at the Nanoscale.

The DSMC computation of nanoscale flow characterized by a scale $L \simeq 10-10000$ nm faces two challenges to the implementation of the method. Those challenges are depicted in Figure 1-4 which shows the number of real particles inside the domain as well as Knudsen number as function of the characteristic length of the domain L. The first challenge relates to the small number of real particles (N) available in a nanoscale domain, this number is increasing by increasing the scale of the domain. Figure 1-4 shows the real number of particles of N2 in a domain L^3 with number density in the range of $n_0 = 2.688 \times 10^{25}$ m-3 at a pressure of 1 atm to $0.0001\,n_0$. Figure 1-4 shows that the number of real particles for $L \simeq 100$ nm decrease from $\sim 10^4$ at $1\,n_0$ to ~ 3 at $0.0001\,n_0$. For $L \simeq 1000$ nm the number of particles becomes $\sim 10^7$ at $1n_0$ and reduces to $\sim 10^3$ at $0.0001n_0$. Also the graph shows that for 0.1 atm pressure which will give a mean free path of 481 nm then the volume L^3 of $L \simeq 100$ nm will contain 2690 real gas particles, since the DSMC cells are required to scale with the mean free path. The DSMC simulation therefore, may require particle weights F_N (which is the ratio of the number of real particles to the number of simulated particles) to be much smaller when compared with those used traditionally in typical macro or micro applications.

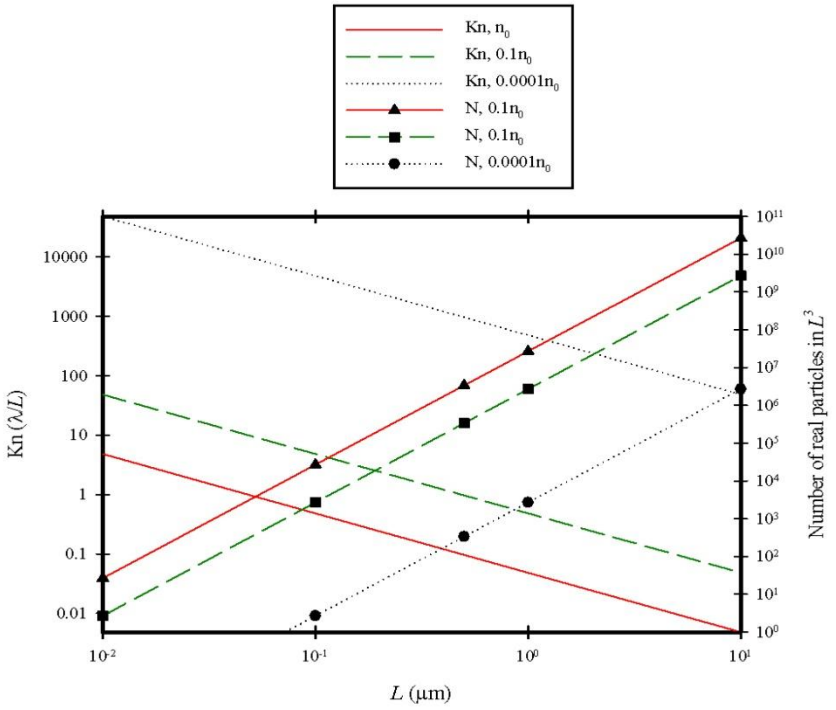

Figure 1-4. Physical parameters in nanoscale domains.

The second challenge relates to the fact that nanoscale flow domains can be of the order or smaller than λ. Figure 1-4 shows that for $L \simeq 10-10000$ nm the flow is expected to be in the transitional to free-molecular regime for all densities considered. For sub-atmospheric densities $0.1\,n_0$ it is shown that the flow will exhibit $Kn \geq 1$ for most scales considered covering the transitional and free molecular regimes. While this condition is encountered in rarefied microscale or macroscale flows, it is also the case that in such flows the characteristic scale L often represents a feature or subscale of the entire domain of interest.

However, at the nanoscale the entire domain characterized by L can be of the order or smaller than λ. A DSMC simulation therefore, requires discretization with computational cells that have volumes of the order of the entire flow domain. The small number of real particles in a nanoscale domain and the large Knudsen number, present a compounded computational requirement for DSMC simulations that is addressed in this dissertation.

1.4 Goals, Objectives and Approach

This dissertation has the following two primary goals:

1. To investigate supersonic flows into sub-micron channels by applying the U3DSMC method and thus, demonstrate the applicability to nanoscale domains of Bird's (1994) DSMC approach as implemented in U3DSMC. The generic geometry considered in this work in shown in Figure 1-5.
2. To contribute to the computational mathematics background of U3DSMC by investigating the fluctuations and the statistical errors associated with the U3DSMC approach and, by developing a formal mathematical background for the subsonic boundary conditions implemented in U3DSMC.

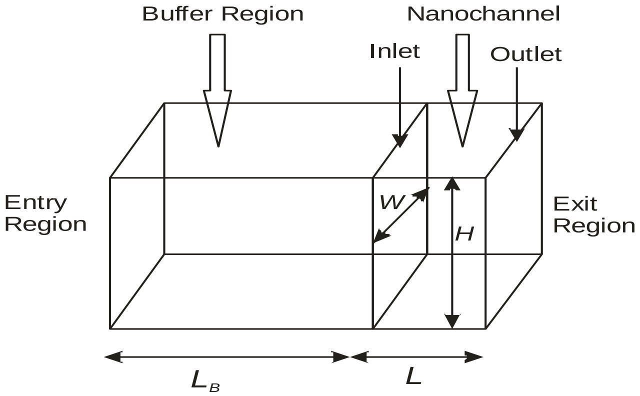

Figure 1-5. Typical nanochannel geometry used in U3DSMC simulations.

The Objectives used to accomplish the Goals are:

1. Verify and validate the U3DSMC method by comparisons with previous simulation results from flows in microchannels as well as theoretical estimates.
2. Further develop the computational mathematics background of U3DSMC by
   a. Developing the mathematical formulation for the subsonic boundary condition implementation used in U3DSMC.
   b. Investigating the statistical fluctuations that are associated with the U3DSMC method resulting both from the sampling of the average macroscopic properties and from decreasing the scale of the domain of interest.
3. Apply U3DSMC to explore physical phenomena in supersonic sub-atmospheric and atmospheric gas flows into nanochannels and establish the applicability of U3DSMC at the nanoscale.

The Approaches used to accomplish each of the Objectives are provided below.

1. Validation and Verification of U3DSMC.
   a. Compare U3DSMC results from simulation of supersonic flows into microchannels with 2D DSMC results (Liou and Fang, 2001; Le and Hassan, 2007). The simulation involves the supersonic flow of nitrogen into a microchannel with height of 1.2 μm and width of 6 μm. The depth used in the simulation was the same as the mean free path of the free stream flow. The free stream conditions correspond to $P_\infty = 72450$ Pa, $M_\infty = 4.15$, $Kn = 0.062$ and $\lambda_\infty = 74.4$ nm. The first 0.1 L of the microchannel is assumed to be specularly reflecting in order to generate the uniform free stream condition inside the microchannel and the outlet is assumed to be vacuum. The comparisons are based

   on the centerline temperature, the heat flux to the wall of the microchannel, as well as the stream velocity as a function of the transverse direction evaluated at $x = 0.5L$.

   b. Compare heat transfer rates obtained with U3DSMC at the upper wall of the nanochannel for cases where the Knudsen number is near that of free molecular flow with theoretical estimates applicable to free-molecular flows.
   c. Compare mass flux at the outlet with the results from the semi-analytical theory developed by Hughes and De Leeuw (1965) for free-molecular tube flows. In this comparison, we calculate the exit mass flux from the nanochannel and compare the results to the theory.
   d. Perform a grid sensitivity analysis to investigate the effects of the grid element size on the U3DSMC results. The simulations involve flows into nanochannels of height 0.1 μm, aspect ratio of 10 and height of 0.5 μm and aspect ratio of 1. The investigation is accomplished by doubling the Delaunay edge length while keeping all other computational parameters.
2. Further development of the computational mathematics background of the U3DSMC.
   a. Subsonic boundary conditions at an inlet or outlet have been implemented in U3DSMC by Chamberlin (2007). The formal mathematical background of this approach is established in this dissertation using the characteristics approach.
   b. The statistical error in number density, mean velocity and translational temperature obtained from U3DSMC simulations are compared with theoretical estimates from statistical mechanics. This investigation considers the effects of

    the number of computational particles per Delaunay cell and Mach number on the fractional error for uniform and the pressure driven flows in nanochannels.

3. Investigation of nanoflows using U3DSMC and applicability of DSMC to nanoscales.
    a. Characterize the effects Knudsen number on gaseous atmospheric and sub-atmospheric supersonic flows into sub-micron channels by studying the resulting phase-space plots and the centerline mean properties,
    b. Investigate the geometrical effects by considering aspect rations of 1, 10, 100
    c. Study the effect of the incoming speed by considering speed ratios of 2, 5 and 10.
    d. Study heat transfer by considering fully diffuse reflection of the walls and a wall temperature equal to the free stream.
    e. Study the impact of boundary conditions. At the inlet we incorporate a buffer region where the free stream boundary conditions are applied, and at the outlet we impose pressure in the range from 0 to 200 kPa.
    f. Perform the analysis using phase-space distributions resulting from the U3DSMC simulations as well as the centerline macroscopic properties.

The presentation of this work is organized in the following manner. In Chapter 2, a review for the U3DSMC method is presented and validation of the code is established. In Chapter 3, the U3DSMC statistical fluctuations and errors are presented. In Chapter 4, the sub-atmospheric supersonic incoming flows into sub-micron channels are presented and the effects of the aspect ratio, back pressure, speed ratio and Knudsen number are investigated. In Chapter 5, the atmospheric supersonic incoming flows into sub-micron channels are presented and the effects of the aspect ratio, speed ratio and Knudsen number are investigated. Conclusions and recommendations for future work are discussed in Chapter 6.

2 REVIEW OF THE U3DSMC METHODOLOGY

The Direct Simulation Monte Carlo (DSMC) method was developed by Bird (1994) and is considered the most widely used technique to simulate rarefied gaseous flows including those in micro domains (Bird, 1981; Rubinstein, 1981). We review in this chapter the basic elements of the unstructured 3D Direct Simulation Monte Carlo (U3DSMC) used for this study along with numerical challenges associated with the DSMC computations of nanoscale physical domains. The details of the U3DSMC method have been presented by Chamberlin (2007). Algorithmic features of U3DSCM, such as loading, injection, particle-tracing, and sampling of macroscopic variables are shared by a methodology developed for the simulation of fully ionized flows (Spirkin, 2006; Gatsonis and Spirkin, 2009). U3DSMC had been validated by comparison to results from literature including both internal and external flows such as flow over flat plate and the pressure driven flows (Chamberlin, 20007). In this chapter, validation for the U3DSMC will be accomplished by comparisons with previous DSMC results of Liou and Fang, (2001) and Le *et al*. (2007) for 2D supersonic flows into microchannels.

2.1 Unstructured 3d Direct Simulation Monte Carlo (U3DSMC) Method

We consider a gas occupying a volume Ω consisting of several species denoted by the species index s each with N_s particles each with a velocity $\mathbf{v} = (v_x, v_y, v_z)$. The single-particle distribution function for species particle s gives the average number of particles in a volume $d^3rd^3v \equiv d\mathbf{r}\,d\mathbf{v}$ of the phase-space centered at a point $(\mathbf{r},\mathbf{v})$ as

$$f_s\left(\mathbf{r},\mathbf{v},t\right)d^3rd^3v = d^6\mathrm{N}_s(t) \tag{2.1}$$

and the local number density is then

$$n_s(r,t) = \int f_s\left(\mathbf{r},\mathbf{v},t\right) d^3 v \tag{2.2}$$

The equation that describes the evolution of the distribution function represented in eq. (2.1) is Boltzmann's equation

$$\frac{\partial f_s}{\partial t} + \mathbf{v}_s \cdot \frac{\partial f_s}{\partial \mathbf{r}} + \mathbf{a}_s \cdot \frac{\partial f_s}{\partial \mathbf{v}_s} = \sum_{q=1}^{s} \int_{-\infty}^{\infty} \int_{0}^{4\pi} \left(f_s * f_q * - f_s f_q \right) v_{r,sq} \sigma_{T,sq} \, d\Omega \, d\mathbf{v}_q \tag{2.3}$$

where, $\mathbf{a}_s$ is the is the resulting acceleration due to an external force, $d\Omega$ is the solid angle, $\sigma_{T,sq}$ is the total collision cross section and $v_{r,sq}$ is the relative velocity. The right hand side of the equation is commonly referred to as the collision term (Sec. 5, Gombosi, 1994; Sec. 3.2, Bird. 1994).

Using eq. (2.1) we define the species-mean particle velocity $\mathbf{V}_s = \left\{ V_{sx}, V_{sy}, V_{sz} \right\}$ by

$$\mathbf{V}_s(\mathbf{r},t) \equiv \left\langle \mathbf{v} \right\rangle_s = \int_{-\infty}^{\infty} \mathbf{v} f_s\,(\mathbf{r},\mathbf{v},t) d\mathbf{v} \Big/ n_s(\mathbf{r},t) \tag{2.4}$$

The mass-average velocity $\mathbf{V} = \left\{ V_x, V_y, V_z \right\}$ used to represent the gas as a single fluid is

$$\mathbf{V}(\mathbf{r},t) = \sum_s n_s m_s \mathbf{V}_s \Big/ \sum_s n_s m_s \ . \tag{2.5}$$

The species diffusion velocity is defined as

$$\mathbf{W}_s = \mathbf{V}_s - \mathbf{V} . \tag{2.6}$$

The species s thermal (or peculiar or random) velocity is given with respect to the species mean velocity as

$$\mathbf{C}_s^* = \mathbf{v}_s - \mathbf{V}_s \tag{2.7}$$

or with respect to the mass-averaged velocity as

$$\mathbf{C}_s = \mathbf{v}_s - \mathbf{V} = \mathbf{C}_s^* + \mathbf{W}_s \tag{2.8}$$

Physically significant moments of the distribution (macroscopic properties) can be derived using as the reference velocity either the species-average velocity or the mass-average velocity (Gombosi, 1994; Burgers, 1969).

The translational temperature is defined in the species-mean system as T_s^* and in the mass-average system as T_s by,

$$\frac{3}{2} k_B T_s^{(*)}(\mathbf{r}, t) = \frac{1}{2} m_s \left\langle C_s^{(*)2} \right\rangle \tag{2.9}$$

with

$$T_s^* = T_s + m_s W_s^2 / 3k_B \tag{2.10}$$

where the Boltzmann constant is $k_B = 1.38 \times 10^{-23}$ (m^2 kg s^{-2} K^{-1}). Similarly, the scalar pressure is

$$p_s^{(*)}(\mathbf{r}, t) = n_s m_s \left\langle C_s^{(*)2} \right\rangle \Big/ 3, \tag{2.11}$$

the pressure tensor

$$\mathbf{P}_s^{(*)}(\mathbf{r}, t) = n_s m_s \left\langle \mathbf{C}_s^{(*)} \mathbf{C}_s^{(*)} \right\rangle \tag{2.12}$$

and the heat flux vector is

$$\mathbf{q}_s^{(*)}(\mathbf{r}, t) = n_s m_s \left\langle C_s^{(*)2} \mathbf{C}_s^{(*)} \right\rangle \Big/ 2 \tag{2.13}$$

We define also single-fluid macroscopic variables for the gas as follows:

$$\mathbf{J}(\mathbf{r}, t) = \sum_s n_s m_s \mathbf{V}_s = \rho \mathbf{V} + \sum_s n_s m_s \mathbf{W}_s \tag{2.14}$$

where $\mathbf{J}(\mathbf{r}, t)$ is the mass flux.

$$T(\mathbf{r},t) = \sum_s n_s T_s^* \,/ \sum_s n_s = \left(1 \Big/ \sum_s n_s \right) \sum_s n_s T_s \;+ n_s m_s W_s^2 \,/\, 3k_B \tag{2.15}$$

$$p(\mathbf{r},t) = \sum_s p_s^* = \sum_s p_s \;+ \sum_s n_s m_s W_s^2 \,/\, 3 \tag{2.16}$$

$$P(\mathbf{r},t) = \sum_s P_s^* = \sum_s P_s \;+ \sum_s n_s m_s \mathbf{W}_s \mathbf{W}_s \tag{2.17}$$

$$\mathbf{q}(\mathbf{r},t) = \sum_s \mathbf{q}_s^* = \sum_s \mathbf{q}_s \;+ (3\,/\,2) p_s \mathbf{W}_s + \mathbf{W}_s . \mathbf{P}_s + (1\,/\,2) n_s m_s W^2{}_s \mathbf{W}_s \tag{2.18}$$

Other transport properties and macroscopic equations can be defined using either reference frame.

Bird’s DSMC method (Bird, 1994) simulates the Boltzmann equation (2.3) using a number of computational particles, each representing F_N real particles. The major assumption behind the DSMC method is that the molecular motion is uncoupled from the inter-molecular collisions

$$\Delta\tau << \tau_{coll} \tag{2.19}$$

where, $\Delta\tau$ is the time step and τ_{coll} is the mean collision time. For a hard-sphere gas in equilibrium a simple expression for the mean collision rate provides

$$\tau_{coll} \equiv \left(\nu_0\right)^{-1} = \left(4\sqrt{\pi} d^2 n \sqrt{\frac{kT}{m}} \right)^{-1} \tag{2.20}$$

Also, the method assumes the overwhelming majority of the collisions will be binary. Under these assumptions, the DSMC method is limited to model dilute gases only. The dilute gas is valid when the mean molecular spacing (δ) is much greater than the effective molecular diameter (d_{mol})

$$\delta \gg d_{mol} \tag{2.21}$$

where the mean molecular spacing is related to the number density of the gas as

$$\delta = n^{-1/3} \tag{2.22}$$

The computational cells in DSMC scale with the local λ so for a gas with mean thermal speed $\left\langle C_s \right\rangle$ the requirement expressed in (2.19) results in

$$\left\langle C_s \right\rangle \Delta\tau < \lambda \tag{2.23}$$

The U3DSMC method implements Bird's DSMC method and algorithms onto an unstructured tetrahedral mesh.

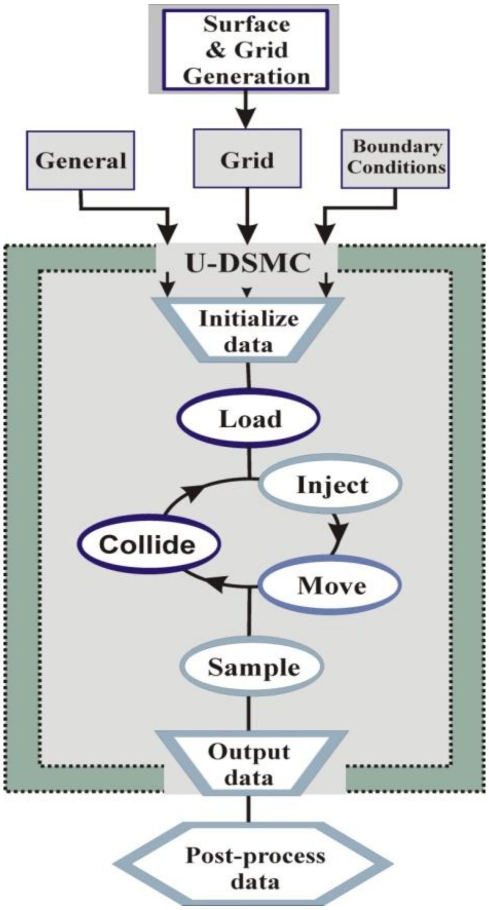

Figure 2-1 U3DSMC flow chart (adapted from Chamberlin, 2007.)

The flowchart in Figure 2-1 shows a general overview of the basic DSMC steps and algorithms that are utilized in the U3DSMC code. From Figure 2-1 , it is very clear that in order to run the U3DSMC, three files are required: the general input file, the grid file and the boundary conditions file. In the general input file, all the specifications on the gas of interest are specified such as the gas composition as well as the collision model, time step selection, and the output time filing. The grid file contains all the information of the grid, such as the node locations, connectivity lists, and face attributes. The boundary condition file consists of the boundary conditions applied on any selected boundary; those conditions could be free stream, subsonic inlet or subsonic exit boundary conditions.

2.1.1 Grid Generation

The DSMC method in this work is implemented on an unstructured, tetrahedral Delaunay mesh. The grid generator discretizes the domain Ω by G_D Delaunay tetrahedra that have edge lengths scaling with a fraction of the local mean-free path λ.

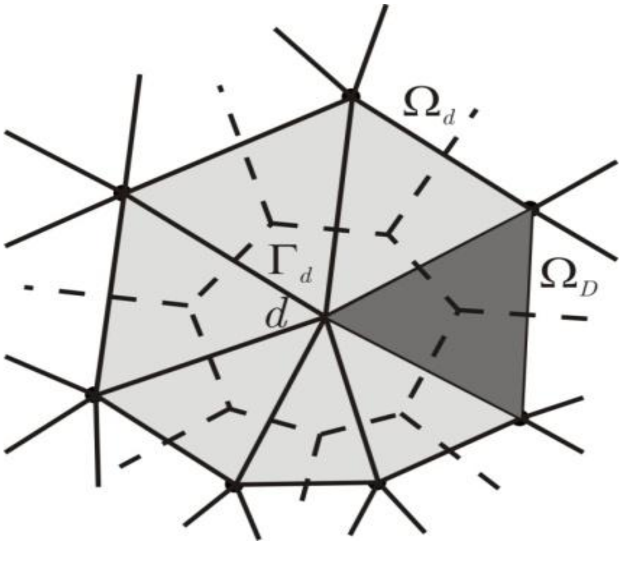

Figure 2-2. A Delaunay cell Ω_D , the Voronoi dual Γ_d and a Delaunay supercell Ω_d depicted in 2D.

Each node d is associated with the Voronoi dual, Γ_d and the Delaunay supercell Ω_d formed by all the Delaunay cells that share the node d (Figure 2-2).

The advantage of using the unstructured mesh is that we can capture the arbitrary geometries due to the geometrical flexibility supported by this technique. The mesh can be generated by a Delaunay triangulation code developed by Kovalev, (2000) and Hammel (2002) or by any commercial grid-generation software. The second option was adopted in this dissertation following Chamberlin (2007) who used COMSOL and developed a data-structure interface to accommodate the data structure of U3DSMC (Chamberlin and Gatsonis, 2008). The use of commercially available grid generators provides full control on the mesh parameters such as the edge length cell as well as providing ease of use and significant time savings.

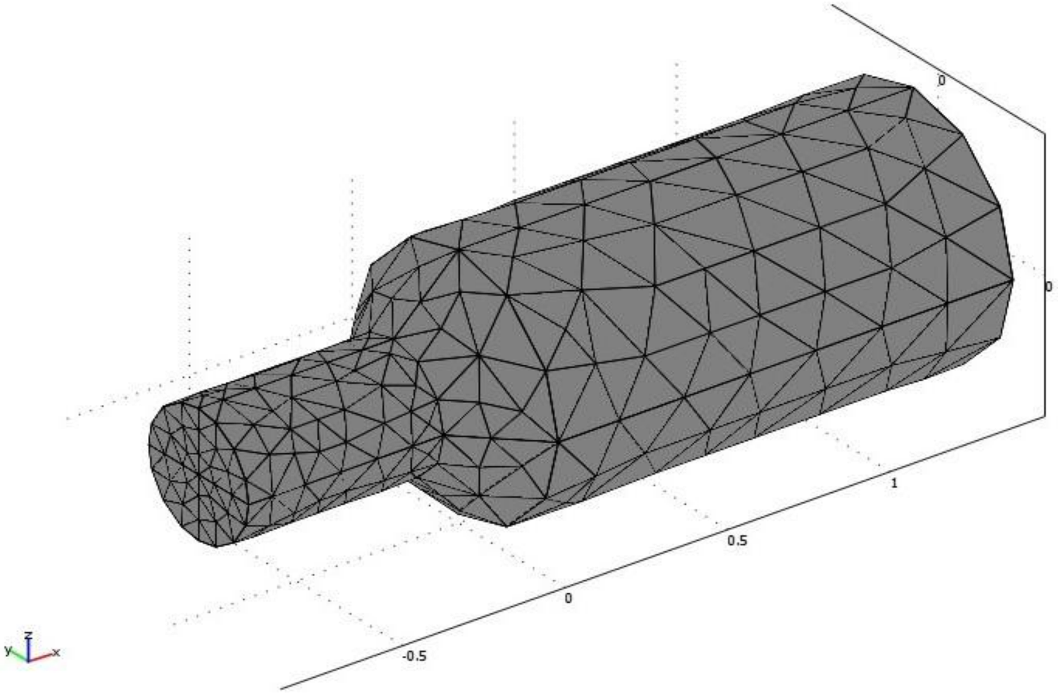

Figure 2-3 An example grid using COMSOL's grid generator.

Figure 2-3 shows a typical example of the surface triangulation obtained using COMSOL for grid generation (Ch. 5, COMSOL).

2.1.2 Particle Loading

In U3DSMC, particle loading is carried out by placing species s particles in each Delaunay cell of the domain following a prescribed distribution. For a drifting Maxwellian distribution with number density $n_s(\mathbf{r},t)$, translational temperature $T_s(\mathbf{r},t)$, and mean species velocity $\mathbf{V}_s(\mathbf{r},t)$

$$f_{0s}(\mathbf{r},\mathbf{v},t) = n_s(\mathbf{r},t)\left(\frac{m_s}{2\pi kT_s}\right)^{3/2} \exp\left[-\frac{m_s(\mathbf{v} - \mathbf{V}_s)^2}{2kT_s}\right] \tag{2.24}$$

the number of computational particles loaded at each Delaunay cell is

$$N_D = n_s \Omega_D \big/ F_N , \tag{2.25}$$

where F_N is the particle weight. The position of each particle is determined using local coordinates in each cell and the velocities are sampled from eq. (2.24) following the acceptance –rejection method (Gatsonis and Spirkin, 2008) to get the thermal or peculiar specie velocity and consequently the total specie molecular velocity.

2.1.3 Particle Injection

In U3DSMC particle injection is required to introduce computational particles inside the computational domain through a surface as indicated in Figure 2-1. The inward number flux of particle of species s through a surface with unit normal n, inclined at an angle θ to the species mean velocity $\mathbf{V}_s$ due to a drifting Maxwellian eq. (2.24) is

$$\dot{\mathrm{N}}_s = \frac{n_s C_s^m}{2\sqrt{\pi}} \left(\exp\left(-S_s^{\,2} \cos^2\left(\theta\right)\right) + \sqrt{\pi}\, S_s \cos\left(\theta\right) \left\{ 1 + \operatorname{erf}\left(S_s \cos\left(\theta\right)\right) \right\} \right), \tag{2.26}$$

where the most probable thermal speed is

$$C_s^m = \sqrt{2k_B T_s \,/\, m_s} \tag{2.27}$$

and the speed ratio of the mean speed to the most probable speed is

$$S_s = V_s \,/\, C_s^m \tag{2.28}$$

Using the speed of sound

$$a_s = \sqrt{\gamma k_B T_s \,/\, m_s} \tag{2.29}$$

the Mach number is

$$M_s = V_s \,/\, a_s \tag{2.30}$$

The number of species s computational particles injected to the domain in a given time is calculated for each face by

$$\Delta N_s = \dot{\mathrm{N}}_s \Delta\tau\, A_s \Big/ F_N \tag{2.31}$$

where $\Delta\tau$ is the time step and A_s is the area of the surface element. The position of particles inside a Delaunay cell is determined by a random process using local coordinates of the cell surface. The velocities of the injected particles are sampled from the distribution function following the CDF (Cumulative Distribution Function) method, or the Box-Muller method or the acceptance-rejection algorithm (Gatsonis and Spirkin, 2008). The boundary condition on the surfaces where the injection is happening is either free stream or subsonic inlet or subsonic exit boundary conditions.

2.1.3.1 Free Stream Boundary

For a free stream boundary the number density, temperature and the velocity (n, T, V) are given at the face of a surface element and defined completely by the drifting Maxwellian eq. (2.24).

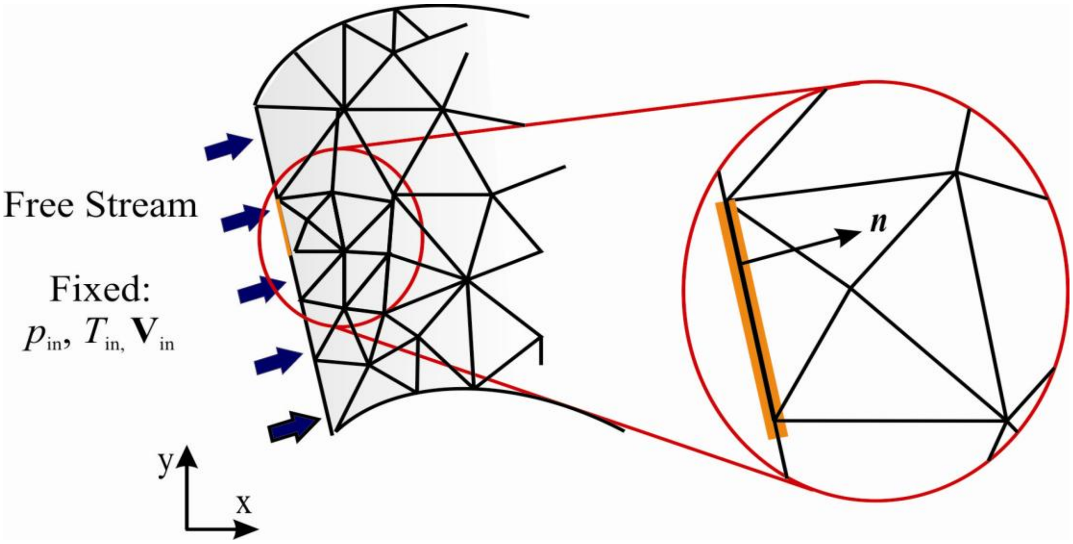

Figure 2-4. Free stream boundary condition.

The conditions at a free stream boundary are shown in Figure (2.4). Particles introduced into the domain following the injection algorithm described in sec. 2.1.2. In the case of a free stream boundary, all particles are injected into the domain through at inlet surface ($V.n < 0$) while no particles are injected through an outlet ($V.n > 0$). Molecular velocities which are the summation of the average and the thermal velocities are found after sampling the distribution function based on the fixed properties (n_{in}, T_{in} and V_{in}).

2.1.3.2 Subsonic Inlet Boundary

In U3DSMC a subsonic boundary is associated with a surface where the pressure and the density are fixed as shown in Figure 2-6 and the mean velocity is evaluated using information from within the domain. Once $n_s, T_s, \mathbf{V}_s$ are obtained on a surface, the particles are injected into the domain following the procedure outlined in Sec. 2.1. The subsonic inflow method used in U3DSMC was developed by Chamberlin (2007) following the approach that has its roots in the method of characteristics (Whitfield and Janus, 1984); Nance *et al.*, 1997; Liou and Fang, 2000; Wang and Li, 2004) . We provide below the theory behind the method of characteristics for the 1D Euler equations and formally derive the methodology used in U3DSMC .

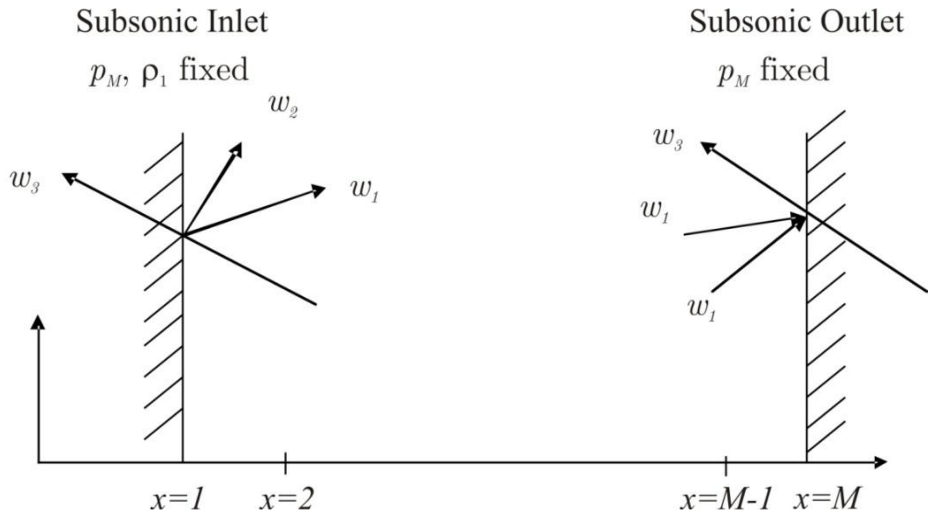

Figure 2-5. Illustration of the characteristic method for subsonic inlet and subsonic outlet conditions.

The inviscid, 1-D, steady state and constant cross section Euler equations can be written in terms of the primitive variables U (Sec. 16.4, Hirsch, 1995; Yee *et al*., 1982)

$$U = \begin{pmatrix} \rho \\ V_x \\ p \end{pmatrix} \tag{2.32}$$

as

$$
\begin{aligned}
&V_x \frac{\partial \rho}{\partial x} - \frac{V_x}{a^2}\frac{\partial p}{\partial x} = 0 \\
&(V_x + a)\left(\frac{\partial V_x}{\partial x} + \frac{1}{\rho a}\frac{\partial P}{\partial x}\right) = 0 \\
&(V_x - a)\left(\frac{\partial V_x}{\partial x} + \frac{1}{\rho a}\frac{\partial P}{\partial x}\right) = 0
\end{aligned}
\tag{2.33}
$$

where a is the speed of sound. For locally constant values of $V_{x\circ}, a_\circ, \rho_\circ$, we can define the characteristic vector W as:

$$
W = \begin{pmatrix} w_1 \\ w_2 \\ w_3 \end{pmatrix} = \begin{pmatrix} \rho - \dfrac{P}{a_\circ{}^2} \\ \dfrac{1}{\sqrt{2}}(V_x + \dfrac{P}{\rho_\circ a_\circ}) \\ \dfrac{1}{\sqrt{2}}(-V_x + \dfrac{P}{\rho_\circ a_\circ}) \end{pmatrix} = T_0^{-1} U \tag{2.34}
$$

where

$$
T_\circ = \begin{pmatrix} 1 & \rho_\circ / (\sqrt{2} a_\circ) & \rho_\circ / (\sqrt{2} a_\circ) \\ 0 & 1 / \sqrt{2} & -1 / \sqrt{2} \\ 0 & \rho_\circ a_\circ / \sqrt{2} & \rho_\circ a_\circ / \sqrt{2} \end{pmatrix} \tag{2.35}
$$

The characteristic equations can then be written as

$$
\begin{pmatrix} V_{x\circ} & 0 & 0 \\ 0 & V_{x\circ} + a & 0 \\ 0 & 0 & V_{x\circ} - a \end{pmatrix} \frac{\partial W}{\partial x} = \Lambda_\circ \frac{\partial W}{\partial x} = 0 \tag{2.36}
$$

The method of characteristics for the subsonic inlet and subsonic outlet boundary condition is illustrated in Figure 2-5. In a subsonic inlet, w_1, w_2 represent the physical boundary conditions, while in a subsonic outlet, w_3 is the physical boundary condition. Following Hirsch (Sec.19.1.5, 1995) and Yee at al. (1982), for a subsonic inlet the two physical boundary conditions specified at the boundary are p_1 and ρ_1 as shown in Figure 2-5. Zero-order space and zero-order time extrapolation of the characteristic variable w_3 between the boundary point (subscript 1) and the interior point (subscript 2) provides the numerical boundary condition

$$w_3\Big)_1^n = w_3\Big)_2^n \tag{2.37}$$

Using eq. (2.34)

$$\left(\frac{1}{\sqrt{2}}(V_x - \frac{P}{\rho_\circ a_\circ})\right)_1^n = \left(\frac{1}{\sqrt{2}}(V_x - \frac{P}{\rho_\circ a_\circ})\right)_2^n \tag{2.38}$$

we obtain the third primitive variable,

$$V_{x1}^n = V_{x2}^n + \frac{p_1^n - p_2^n}{\rho_\circ a_\circ} \tag{2.39}$$

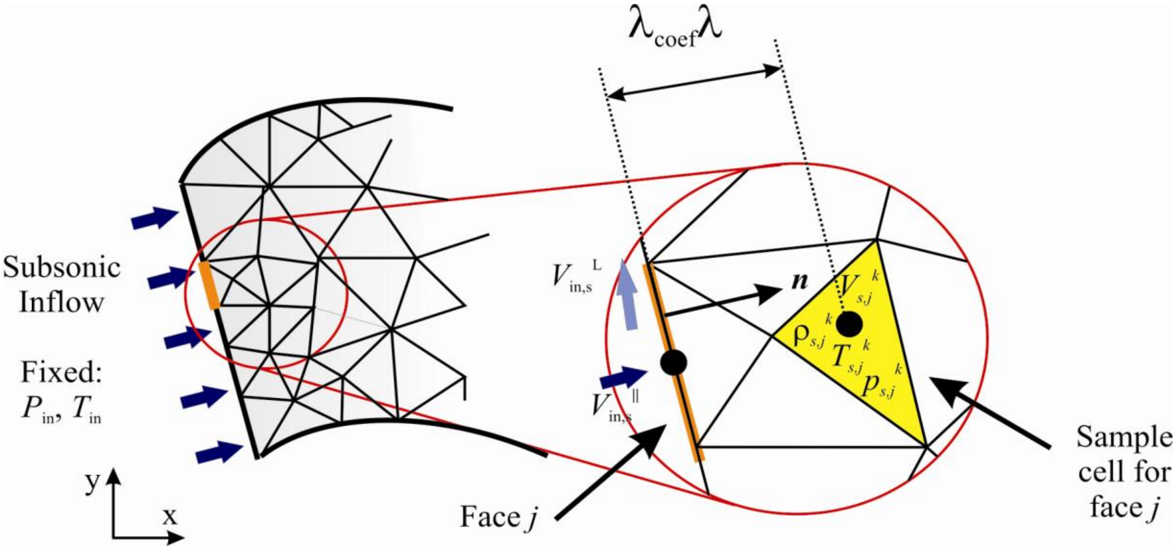

Figure 2-6. Subsonic inlet boundary condition treatment on unstructured grids

Figure 2-6 illustrates the algorithm used in U3DSMC to model the subsonic inlet boundary condition. As in the case of the Euler equations, we specify the species pressure and density at the inlet surface (p_{in}, n_{in}) and we derive the species-mean velocity (V_{in}) so that injection from the boundary can proceed by sampling the distribution function to get the molecular total velocity. The algorithmic steps in the U3DSMC are summarized below.

Step 1: Calculate the normal vector on the injection surface face j

$$\mathbf{n} = \frac{\mathbf{r}_{12} \times \mathbf{r}_{13}}{|| \mathbf{r}_{12} \times \mathbf{r}_{13} ||} \tag{2.40}$$

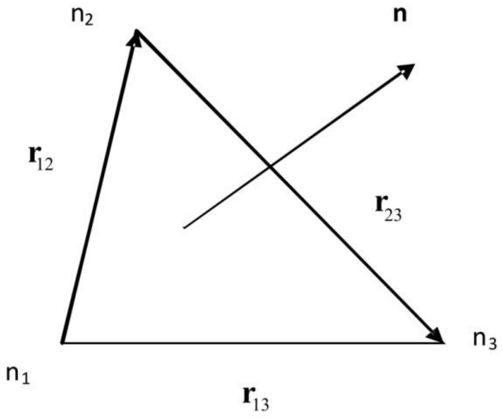

Figure 2-7. Geometry used in calculation of local face normal vectors

In eq.(2.40), $\mathbf{r}_{12}$ is the vector from node 1 to node 2 and $\mathbf{r}_{13}$ is the vector from node 1 to node 3 as shown in Figure 2-7**.**

Step 2: Obtain the sample cell location from where domain properties are to be evaluated

$$x_j^c = x_j^f + \lambda_{coef,s} \lambda_s \mathbf{n} \tag{2.41}$$

Step 3: For each injection surface face, for each species, calculate the sample cell properties

$$n_{s,j}^k = \frac{\sum_{i=1}^{N_{s,j}} F_N}{\Omega_D} \tag{2.42}$$

$$(\mathbf{V}_s)_j^k = \frac{1}{N_{s,j}} \sum_{i=1}^{N_{s,j}} \mathbf{v}_s \tag{2.43}$$

$$\overline{(\mathbf{C}_s^{*2})}_j^k = \frac{1}{N_{s,j}} \sum_{i=1}^{N_{s,j}} \left[(\mathbf{v}_s)_j^k - (\mathbf{V}_s)_j^k \right]^2 \tag{2.44}$$

$$(p_s)_j^k = \frac{1}{3} m_s (n_s)_j^k \left(\overline{C_s^{*2}} \right)_j^k \tag{2.45}$$

$$(T_s)_j^k = \frac{(p_s)_j^k}{(n_s)_j^k k_B} \tag{2.46}$$

$$(a_s)_j^k = \sqrt{\frac{\gamma k_B (T_s)_j^k}{m_s}} \tag{2.47}$$

Step 4: For each inlet surface face, calculate corrected species-drift velocity following eq. (2.39)

$$\left(V_{x,s}\right)_j^k = \left(V_s\right)_j^k \bullet \mathbf{n} \tag{2.48}$$

$$\left(V_{in,s}\right)_j^{k*} = \left(V_s\right)_j^k + \frac{p_{in,s} - (p_s)_j^k}{m_s (n_s)_j^k (a_s)_j^k} \tag{2.49}$$

Step 5: Apply time-averaging to reduce oscillations

$$\left(V_{in,s}\right)_j^k = \frac{1}{4} \left(V_{in,s}\right)_j^{k*} + \frac{3}{4} \left(V_{in,s}\right)_j^{AVE} \tag{2.50}$$

With p, n and V known at the inlet surface face, the injection procedure (Sec 2.1.3) is applied.

2.1.3.3 Subsonic Outlet Boundary

Following Hirsch (Sec.19.1.5, 1995), for a subsonic outlet with physical boundary condition the fixed pressure p_M as indicated in Figure 2-5. Zero-order space and zero-order time extrapolation of the characteristic variables provides

$$\begin{aligned} w_1\Big)_M^n &= w_1\Big)_{M-1}^n \\ w_2\Big)_M^n &= w_2\Big)_{M-1}^n \end{aligned} \tag{2.51}$$

and using eq. (2.34), the numerical boundary conditions becomes

$$\begin{pmatrix} \rho - \dfrac{P}{a^2} \\ \dfrac{1}{\sqrt{2}}(V_x + \dfrac{P}{\rho_\circ a_\circ}) \end{pmatrix}_M^n = \begin{pmatrix} \rho - \dfrac{P}{a^2} \\ \dfrac{1}{\sqrt{2}}(V_x + \dfrac{P}{\rho_\circ a_\circ}) \end{pmatrix}_{M-1}^n \tag{2.52}$$

The two numerical primitive variables are

$$\begin{aligned} \rho_M^n &= \rho_{M-1}^n + \frac{p_M^n - p_{M-1}^n}{a_\circ^2} \\ V_M^n &= V_{M-1}^n + \frac{p_{M-1}^n - p_M^n}{\rho_\circ a_\circ} \end{aligned} \tag{2.53}$$

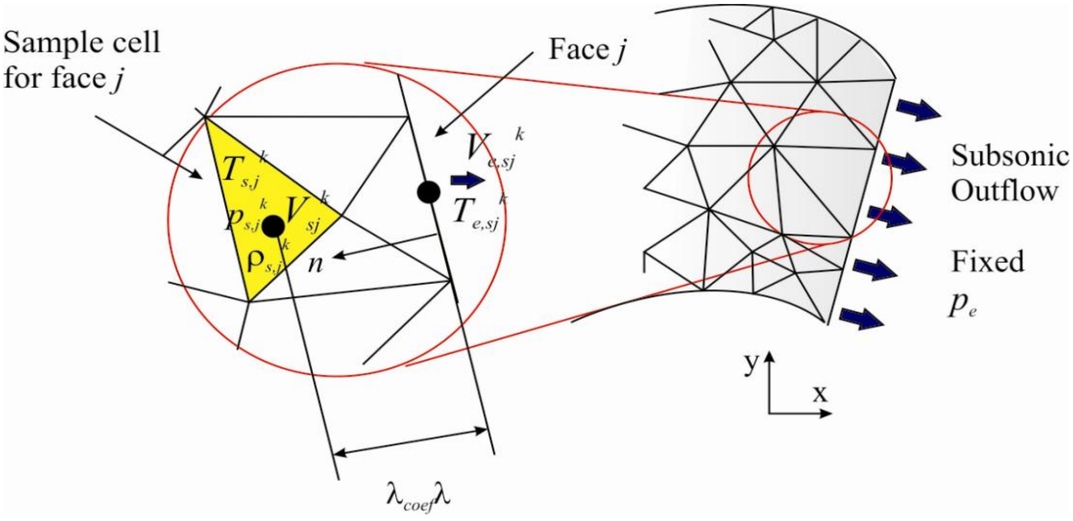

Figure 2-8. Subsonic exit boundary condition treatment on unstructured grids

Figure 2-8 illustrates the implementation of the subsonic exit boundary condition using U3DSMC method. As with the case of the Euler equations, we specify the species pressure at the outlet surface (p_e) and we derive the species-mean velocity and density (V_e, n_e) so that injection from the outlet boundary can proceed. The algorithmic steps in the U3DSMC are summarized below.

Step-1: Calculate the normal vector on the face

$$\mathbf{n} = \frac{\mathbf{r}_{12} \times \mathbf{r}_{13}}{|| \mathbf{r}_{12} \times \mathbf{r}_{13} ||} \tag{2.54}$$

Step-2: The sample cell location is

$$x_j^c = x_j^f + \lambda_{coef,s} \lambda_s \mathbf{n} \tag{2.55}$$

Step-3: For each injection surface face, for each species calculate the sample cell properties:

$$(n_s)_j^k = \frac{\sum_{i=1}^{N_{s,j}} F_N}{\Omega_D} \tag{2.56}$$

$$(\mathbf{V}_s)_j^k = \frac{1}{N_{s,j}} \sum_{i=1}^{N_{s,j}} \mathbf{v}_s \tag{2.57}$$

$$\overline{(\mathbf{C}_s^{*2})}_j^k = \frac{1}{N_{s,j}} \sum_{i=1}^{N_{s,j}} \left[(\mathbf{v}_s)_j^k - (\mathbf{V}_s)_j^k \right]^2 \tag{2.58}$$

$$(p_s)_j^k = \frac{1}{3} m_s \left(n_s\right)_j^k \left(\overline{C_s^{*2}}\right)_j^k \tag{2.59}$$

$$(T_s)_j^k = \frac{\left(p_s\right)_j^k}{\left(n_s\right)_j^k k_B} \tag{2.60}$$

$$(a_s)_j^k = \sqrt{\frac{\gamma k_B \left(T_s\right)_j^k}{m_s}} \tag{2.61}$$

Step-4: For each injection surface face, for each species calculate corrected species-drift velocity based on eq. (2.53) to get:

$$(n_{e,s})_j^k = (n_s)_j^k + \frac{p_{e,s} - (p_s)_j^k}{m_s((a_s)_j^k)^2} \tag{2.62}$$

$$(T_{e,s})_j^k = \frac{p_{e,s}}{(n_{e,s})_j^k \, k_B} \tag{2.63}$$

$$\left(V_{e,s}\right)_j^k = \left(V_{e,s}\right)_j^k \bullet \mathbf{n} \tag{2.64}$$

$$\left(V_{e,s}\right)_j^{k*} = \left(V_s\right)_j^k + \frac{(p_s)_j^k - p_{e,s}}{m_s (n_s)_j^k (a_s)_j^k} \tag{2.65}$$

Step 5: Apply time-averaging to reduce oscillations

$$\left(V_{e,s}\right)_j^k = \frac{1}{4}\left(V_{e,s}\right)_j^{k*} + \frac{3}{4}\left(V_{e,s}\right)_j^{AVE} \tag{2.66}$$

With p, n and V known at the outlet surface face surface the injection procedure including the sampling of the velocities (Sec. 2.1.3) is applied.

The pressure in the exit region can be set to a vacuum. In such a case, any particle reaching the exit plane is removed from the domain and no particles are allowed to enter the computational domain through the exit plane.

2.1.4 Particle Motion

The computational particles are tracked as they interact with other particles and with domain boundaries. For specie s with position $\mathbf{r}_s(t)$ and velocity $\mathbf{v}_s(t) = (v_{sx}, v_{sy}, v_{sz})$ the new particle position is obtained from integration of the equation of motion, given by

$$\mathbf{r}_s(t+dt) = \mathbf{r}_s(t) + \mathbf{v}_s\left(t\right)\Delta\tau \tag{2.67}$$

In U3DSMC molecular motion over the time step ($\Delta\tau$) and intermolecular collisions occurring at a mean collision time τ_{coll} are uncoupled by choosing $\Delta\tau < \tau_{coll}$. Tracing the motion of the particle on the unstructured grid is carried out using the successive-neighbor search algorithm (Gatsonis and Spirkin, 2009).

2.1.5 Elastic Collisions

Modeling of elastic collisions in U3DSMC is accomplished with an implementation of Birds no-time-counter (NTC) method (Chapter 2, Bird 2004) to unstructured grids (Chamberlin, 2007). We summarize the basic algorithmic steps performed for each Delaunay cell of the domain.

Step 1. Calculate the number of particles in the Delaunay cell

$$N_c = \sum_{i=1}^{stack\_last} 1 \tag{2.68}$$

Step 2. Calculate $\left(\sigma_T v_r\right)_{MAX}$ where σ_T is the total collision cross section and v_r is the relative velocity of a collision pair.

Step 3. Calculate the number of collision pairs per Delaunay cell per time step is by

$$N_{pairs} = \frac{1}{2\Omega_D} N_c \overline{N} F_N \Delta\tau \left\{\left(\sigma_T v_r\right)_{MAX}\right\} \tag{2.69}$$

Ω_D is the volume of the Delaunay cell, N_c is the current number of computational particles in the Delaunay cell, $\overline{N}$ is the time-averaged number of computational particles in the Delaunay cell, $\Delta\tau$ is the time step (time elapsed per iteration)

Step 4. Generate N_{pairs} of collision partners chosen at random from the list of particles in the cell. For each collision pair, the value of $\sigma_T v_r$ is determined either by the hard sphere or variable hard sphere models as indicated in eq. (2.70). The variable hard sphere model captures the dependence of the collision cross section on the translational energy while the hard sphere does not. It is worth to mention that the hard sphere model is easy to calculate due to its isotropic scattering.

$$\sigma_T = \int_0^{4\pi} \sigma \, d\Omega = \pi \, d_{12}^2 = \left(\begin{array}{c} \left(\sigma_T\right)_{HS} = \pi \left(\dfrac{d_1 + d_2}{2} \right)^2 \\ \left(\sigma_T\right)_{VHS} = \dfrac{\pi}{4} \left[d_{1,ref} \left(v_{1,ref} / v_r \right)^{\omega_1} + d_{2,ref} \left(v_{2,ref} / v_r \right)^{\omega_2} \right] \end{array} \right) \tag{2.70}$$

$$v_r = \| \mathbf{v}_1 - \mathbf{v}_2 \| \tag{2.71}$$

If the value of $\sigma_T v_r$ for the pair is greater than $\left(\sigma_T v_r\right)_{MAX}$ for the current cell then the cell value of $\left(\sigma_T v_r\right)_{MAX}$ is updated.

The probability of any chosen pair colliding is given as:

$$P_{coll} = \frac{\sigma_T v_r}{\left\{ \left(\sigma_T v_r\right)_{MAX} \right\}} \tag{2.72}$$

Using P_{coll}, each collision pair is chosen to undergo a collision according to the acceptance-rejection algorithm.

Step 5. Calculate the post-collision velocities of the collision pair selected in Step 4.

2.1.6 Inelastic Collisions

Inelastic collisions follow the NTC method and the Larsen-Borgnakke model for the exchange of rotational energy between the collision pair (Borgnakke and Larsen, 1975).

2.1.7 Surface Interactions

Gas surface interactions in U3DSMC include specular, diffuse with full thermal accommodation, and non-diffuse. These models are implemented in U3DSMC is several algorithmic steps. The first step is to determine if the particle's motion is such that a solid surface interaction occurs following the particle tracing algorithm Sec. 2.1.4. If the particle does reflect off a solid surface then the face of reflection is used to determine what type of reflection model is applied. Tabulation of the surface model applied at each face is handled using a surface label referred to as a face attribute. During the grid generation process the user specifies the face attribute to be applied to each flow boundary. This information is then linked to the boundary conditions applied.

In specular reflection, the impinging molecule's surface-normal velocity component is reversed during the collision while the surface-tangential velocity components remain unchanged.

In diffuse reflection the particle's velocity components after the surface collision are determined from sampling an equilibrium distribution with a temperature corresponding to that of the solid surface

In non-diffuse reflection the user specifies the diffuse fraction ε which is the percentage of interactions that are treated as undergoing fully diffuse reflection. For each surface collision, to determine the model used a random fraction R is generated and a selection algorithm is applied. If $R > \varepsilon$ then the interaction is modeled as specular. If $R \leq \varepsilon$ then the interaction is modeled as fully diffuse.

2.1.8 Sampling Macroscopic Parameters

Macroscopic single-fluid and multi-fluid variables are evaluated on nodes by averaging the particle properties within the Delaunay Ω_D or the Voronoi cell Γ_d shown in Figure 2-2. For $N_{sD}(t)$ particles of species s residing in the sampling cell with volume Ω_D associated with node d the number density is defined as

$$n_s(D,t) \equiv \sum_{p=1}^{N_{sD}} F_{Np} \Big/ \Omega_D \,, \tag{2.73}$$

the mean species velocity $\mathbf{V}_s(D,t) = \left\{V_{sx}, V_{sy}, V_{sz}\right\}$ is

$$\mathbf{V}_s(D,t) \equiv \sum_{p=1}^{N_{sD}} \mathbf{v}_{sp} \Big/ N_{sD} \,, \tag{2.74}$$

and the mass-average velocity $\mathbf{V}(D,t) = \left\{V_x, V_y, V_z\right\}$ is

$$\mathbf{V}(D,t) = \sum_s n_s m_s \mathbf{V}_s(D,t) \Big/ \sum_s n_s m_s \tag{2.75}$$

For the p-th particle the thermal velocity $\mathbf{C}_{sp}$ is defined with respect to the mass-average velocity $\mathbf{V}$ as

$$\mathbf{C}_{sp} = \mathbf{v}_{sp} - \mathbf{V} \tag{2.76}$$

The translational temperature is

$$\frac{3}{2} k T_s(D,t) = \frac{1}{2} m_s \left(\sum_{p=1}^{N_{sD}} C_{sp}^2 \right) / \, N_{sD} \tag{2.77}$$

and the scalar pressure is

$$p_s(D,t) = n_s(D,t)kT_s(D,t) \quad (2.78)$$

We also calculate the overall single-fluid properties as

$$T(D,t) = \sum_s n_s T_s^*(D,t) \,/\, \sum_s n_s(D,t) \quad (2.79)$$

$$p(D,t) = \sum_s p_s^* \quad (2.80)$$

The instantaneous value of a macroscopic variable associated with a node d is obtained with a volume averaged procedure in the Delaunay supercell Ω_d,

$$\Upsilon(d,t) = \frac{\sum_{D=1}^{cells} \Upsilon(D,t)\Omega_D}{\Omega_d} \quad (2.81)$$

Following standard procedures, nodal values in U3DSMC are averaged over a large number of computational time steps to obtain time-averaged macroscopic gas properties. For example, the nodal value for the mean velocity obtained between the m-th and M-th time steps, using $M-m$ samples, is

$$\mathbf{V}_s(d) = \frac{\sum_{n=m}^{M} \mathbf{V}_s(d,t^n)}{(M-m)} \quad (2.82)$$

2.1.9 Flux Evaluation

The U3DSMC code has the ability to capture the flux through any arbitrary interior or free stream boundary or even subsonic inlet or subsonic outlet boundary faces defined during grid generation as an interior or free boundary surface or subsonic inlet or subsonic outlet surfaces. The number and mass fluxes are evaluated as

$$\Gamma_{N_s} = \frac{\sum_{i=1}^{\eta} F_N}{\Delta t \sum_{j=1}^{faces} A_{s,j}} \tag{2.83}$$

$$\Gamma_{m_s} = m_s \Gamma_{N_s} = \frac{\sum_{i=1}^{\eta_q} m_s F_N}{\Delta t \sum_{j=1}^{faces} A_{s,j}} \tag{2.84}$$

where, Γ_{N_s} and Γ_{m_s} are the number, mass fluxes of species s respectively, $A_{s,j}$ is the surface area and Δt is the time interval.

2.1.10 Surface Transport Properties

Several flux properties, such as pressure, shear stress and heat flux (W/m^2) to a solid surface, are determined from the perpendicular or parallel momentum and total energy exchange of the impinging particles. For example,

$$p_{surf} = \sum_j m_j F_N \left[\left(\mathbf{v}_\perp^* \right)_j - \left(\mathbf{v}_\perp \right)_j \right] \Big/ A_s \Delta t \tag{2.85}$$

$$\tau_{surf} = \sum_j m_j F_N \left[\left(\mathbf{v}_{||}^* \right)_j - \left(\mathbf{v}_{||} \right)_j \right] \Big/ A_s \Delta t \tag{2.86}$$

$$q_{surf} = \sum_j F_N \left[\left(E^* \right)_j - \left(E \right)_j \right] \Big/ A_s \Delta t \tag{2.87}$$

In the above equations, $\mathbf{v}^*$ is the reflected velocity component of particle m_i impinging on surface area A_s, E^* is the reflected translational and internal energy of impinging particles, and Δt is the duration of impingement sampling.

2.2 Validation of U3DSMC

U3DSMC had been validated extensively in Chamberlin (2007) by comparison to results from literature including flows over flat plates, plumes, pressure driven internal flows and flow inside nozzles. Chamberlin, (2007) studied also the effects of the time step, the cell edge length as well as the number of simulated particles inside the cell on the accuracy of the U3DSMC code. In his study, a very good agreement between the results from the U3DSMC code and the literature was achieved. In this work, the U3DSMC code is validated by comparisons with previous 2D DSMC results of Liou and Fang (2001) and Le *et al*. (2007).

These simulations of the validation case involved supersonic nitrogen (N_2) flow incoming into a two dimensional microchannel with height of 1.2 μm, length 6 μm and represent the smallest scales available in the literature for comparison.

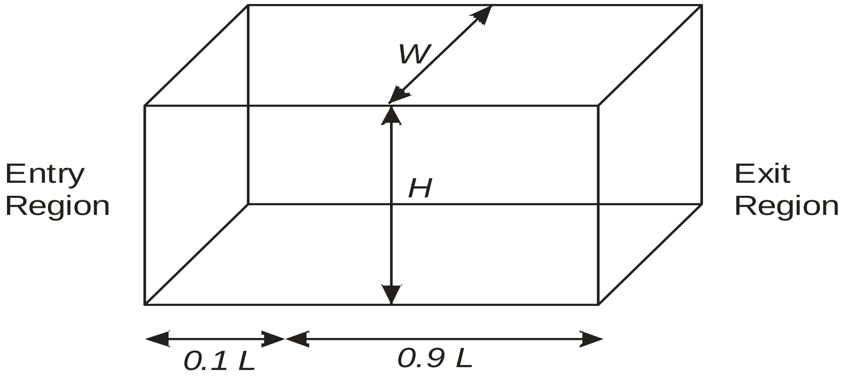

Figure 2-9. Geometry in U3DSMC simulation of microchannel flow for comparison with Liou and Fang (2001) and Le *et al*. (2007)

The domain used in the U3DSMC simulations is depicted in Figure 2-9. The incoming nitrogen N_2 flow has $n_\infty = 1.75 \times 10^{25}$ m^{-3}, $T_\infty = 300$K, $V_\infty = 1465.7$ m/s corresponding to $P_\infty = 72450$ Pa, $M_\infty = 4.15$, and $\lambda_\infty = 74.4$ nm, $Kn_\infty = 0.062$. Following Liou and Fang

(2001) and Le *et al*. (2007), the first $0.1L$ of the length of the computational domain is assumed to be specularly reflecting in order to generate uniform free-stream condition inside the microchannel. The supersonic incoming conditions are applied at the inlet of the computational domain. A vacuum outlet boundary condition is specified at the exit of the microchannel. Particles that leave the exit are removed from the domain and no particles are allowed to return into the domain. The upper and lower walls of the microchannel are isothermal at a constant temperature of 323 K and are assumed to be fully diffuse with perfect thermal accommodation. The side walls are simulated as specular so that they act as symmetry planes. In order to compare with the 2 D results, the depth D of the microchannel in our 3D simulations was varied and it was found that results are not sensitive for $D \geq \lambda_\infty$ and $D = 74.4$ nm was used in the simulations. The domain is discretized with 23032 Delaunay cells with 405 particles/cell upon loading and $\Delta\tau = 1 \times 10^{-13}$ sec. Macroscopic flow properties are sampled once steady state is reached. Twenty samples are used in obtaining the average after reaching the steady state time. The parameters used in the simulation are summarized in Table 2-1.

Table 2-1. Parameters used for comparison between U3DSMC code results, Liou and Fang (2001) and Le *et al*. (2007)

H	1.2 μm
L	6 μm
W	74.4 nm
p_∞	72450 Pa
T_∞	300 K
Kn_∞	0.062
V_∞	1465.7 m/s

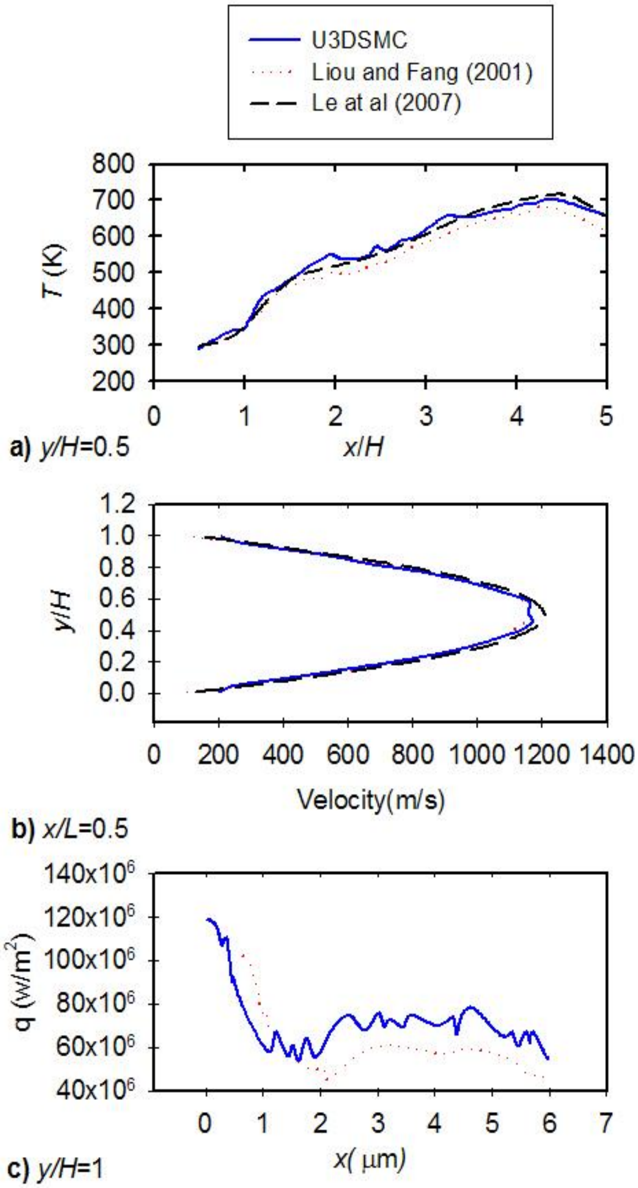

Figure 2-10. Comparison of U3DSMC results with the 2D DSMC results of Liou and Fang (2001) and Le *et al*. (2007)

Figure 2-10a shows the centerline $y / H = 0.5$ translational temperature profile given in Eq. (2.9) obtained from the U3DSMC simulation. The difference between Liou and Fang (2001), Le *et al*. (2007) and our 3D results is less than 7%.

Figure 2-10b shows an excellent agreement between the axial velocity profiles obtained for $x / L = 0.5$ for the results extracted for U3DSMC code and the simulations carried out by Liou and Fang (2001) and Le *et al*. (2007).

Figure 2-10c shows a good agreement with the heat flux at the wall of the microchannel. The heat flux from U3DSMC is evaluated using eq. (2.18). Differences between the 3D and 2D simulations are attributed to the sidewalls present in our 3D simulations.

3 STATISTICAL ERRORS IN U3DSMC SIMULATIONS OF MICRO/NANOSCALE DOMAINS

In this chapter, we provide the basic theory for the statistical fluctuations and errors associated with the U3DSMC method and its application to micronscale and nanoscale flows. We analyze the error in average macroscopic properties such as the density, velocity and temperature associated with the U3DSMC method. We consider uniform and pressure driven (Poiseuille) flows and investigate the effects of the number of simulated particles inside the Delaunay cell and Mach number on fractional errors. We provide also comparisons between the results form U3DSMC and theoretical estimates. The uniform flow consists of a free stream with $n = 2.69 \times 10^{25} \mathrm{m}^{-3}$, $T = 273\ \mathrm{K}$ and a characteristic length of $L = 0.05\ \mu\mathrm{m}$ with resulting Mach number could be either 0.1 or 10. For the case of the pressure driven flows, the nanochannel will be of 500 nm height, 100 nm width and 4 μm length. Subsonic inlet boundary condition are implemented at the inlet of the nanochannel so that the inlet pressure will be 1 atm and $T = 273\ \mathrm{K}$, while subsonic exit boundary condition is implemented at the exit of the nanochannel so that the exit pressure is 0.1 atm. The methodology of implementing those different boundary conditions is discussed in Sec. 2.2.3.

3.1 Mathematical Formulation

In a dilute gas there are inherent statistical fluctuations in macroscopic parameters such as number density, mean velocity, temperature, that are provided by theoretical estimates (see Landau, (1997)). In the case of a particle simulation such as the U3DSMC, these statistical fluctuations result to statistical errors due to the small number of particles used to represent the real number of particles in the domain, the ensemble sampling associated with estimation of macroscopic variables. Such fluctuations and errors when compared to theoretical estimates, are functions of the particle weight (F_N), the volume of the Delaunay cells (Ω_D), the time-step ($\Delta\tau$) used, and the number of samples (M) used to obtain macroscopic properties. We consider the fluctuations associated with three important macroscopic fields, the number density (n), mean velocity (V) and translational temperature (T).

We follow Hadjiconstantinou et al (2003) and generalize their derivation for 3D unstructured grids used in U3DSMC considering a gas of species s particles. We consider a computational domain discretized with $D = 1, G_D$ Delaunay cells, each with a volume Ω_D with the nodes denoted by $d = 1, G_d$ as indicated in Figure 2.2. For steady U3DSMC computations we obtain after reaching steady-state $m = 1, \mathrm{M}$ independent Delaunay cell samples. With a particle weight of F_N, the number of computational particles in a Delaunay cell is N_{sD}^m and the number of real particles in a Delaunay cell is N_{sD}^m

$$\mathrm{N}_{sD}^m = F_N N_{sD}^m \tag{3.1}$$

We denote mean macroscopic variables as $X_{sD}^m \equiv n_{sD}^m, \mathbf{V}_{sD}^m, T_{sD}^m$. For species s particles the number density is

$$n_{sD}^m \equiv \sum_1^{N_{sD}^m} F_N \bigg/ \Omega_D \tag{3.2}$$

The species mean velocity $\mathbf{V}_{sD}^m = \left\{V_{sx}, V_{sy}, V_{sz}\right\}_D^m$ is

$$\mathbf{V}_{sD}^m \equiv \sum_1^{N_{sD}^m} \mathbf{v}_s \bigg/ N_{sD}^m \tag{3.3}$$

and the mass-average velocity $\mathbf{V}_D^m = \left\{V_x, V_y, V_z\right\}_D^m$ is

$$\mathbf{V}_D^m = \sum_s n_s m_s \mathbf{V}_{sD}^m \Big/ \sum_s n_s m_s \tag{3.4}$$

For each particle the thermal velocity is defined with respect to the mass-average velocity as

$$\mathbf{C}_s = \mathbf{v}_s - \mathbf{V} \tag{3.5}$$

and the translational temperature is

$$\frac{3}{2} k T_{sD}^m = \frac{1}{2} m_s \left(\sum_1^{N_{sD}^m} C_s^2 \right) / \, N_{sD}^m \tag{3.6}$$

The sample-averaged mean number of computational particles in a Delaunay cell is

$$N_{sD} = \frac{\sum_{\mathrm{M}} N_{sD}^m}{\mathrm{M}} = \frac{\mathrm{N}_{sD}}{F_N} \tag{3.7}$$

The sample-averaged mean macroscopic property in each cell denoted by $X_{sD} \equiv n_{sD}, \mathbf{V}_{sD}, T_{sD}$ is given by

$$X_{sD} = \frac{\sum_{m=1}^{\mathrm{M}} X_{sD}^m}{\mathrm{M}} \tag{3.8}$$

The sample standard deviation for any variable $X_{sD}^m \equiv n_{sD}^m, \mathbf{V}_{sD}^m, T_{sD}^m$ is defined as

$$\sigma(X_{sD}^m) = \left[\frac{1}{\mathrm{M}-1} \sum_{m=1}^{\mathrm{M}} \left(X_{sD}^m - X_{sD} \right)^2 \right]^{1/2} \tag{3.9}$$

The standard deviation (uncertainty) of any mean variable $X_{sD} \equiv n_{sD}, \mathbf{V}_{sD}, T_{sD}$ is

$$\sigma(X_{sD}) = \frac{\sigma(X_{sD}^m)}{\sqrt{\mathrm{M}}} \tag{3.10}$$

and the fractional error of the mean variable, is defined as the standard deviation of the mean over the mean

$$E_{X_{sD}} = \frac{\sigma(X_{sD})}{X_{sD}} \tag{3.11}$$

These macroscopic properties exhibit statistical fluctuations that have been subject of kinetic theory of gases. For a single-species gas the variance in the number of computational particles in a Delaunay cell is

$$\left\langle \left(N_D^m - N_D\right)^2 \right\rangle \equiv \left\langle \left(\delta N\right)^2 \right\rangle_D = \kappa_T N_D{}^2 \frac{kT_D}{\Omega_D} \tag{3.12}$$

the standard deviation of the mean N_D is

$$\sigma(N_D) = \frac{\sqrt{\left\langle \left(\delta N\right)^2 \right\rangle_D}}{\sqrt{\mathrm{M}}} \tag{3.13}$$

and the fractional error in the number density in a Delaunay cell is

$$E_n = \frac{\sigma_n}{n_D} = \frac{\sigma_N}{N_D} = \frac{1}{\sqrt{\mathrm{M} N_D}} \frac{1}{Ac} \tag{3.14}$$

In the above equation the acoustic number is $Ac = a \big/ a_i$, where a is the speed of sound, and $a_i = \sqrt{\gamma k T_o / m}$ is the speed of sound at a reference temperature. For dilute gases Ac=1.

Similarly, the fractional error in the mean velocity component V_{xD} is

$$E_V \equiv \frac{\sigma(V_{xD})}{V_{xD}} = \frac{1}{\sqrt{\mathrm{M} N_D}} \frac{1}{Ac M \sqrt{\gamma}} \tag{3.15}$$

where $\gamma = c_p / c_v$ is the ratio of specific heats and the Mach number is $M = V_{xD} \big/ a$.

The fractional error in temperature is

$$E_T = \frac{\sigma\left(T_D\right)}{T_D} = \frac{\sqrt{\left\langle(\delta T)^2\right\rangle}}{T_D\sqrt{\mathrm{M}}} = \frac{1}{\sqrt{\mathrm{M}N_D}}\sqrt{\frac{k_B}{C_v}} \tag{3.16}$$

where, C_v is the heat capacity at constant volume.

3.2 U3DSMC Computations At The Nanoscale

The number of computational particles in a computational cell is an important parameter in determining the error in a DSMC calculation. In microscale and nanoscale domains DSMC computations are constrained by the small number of real particles that can reside in the computational cell.

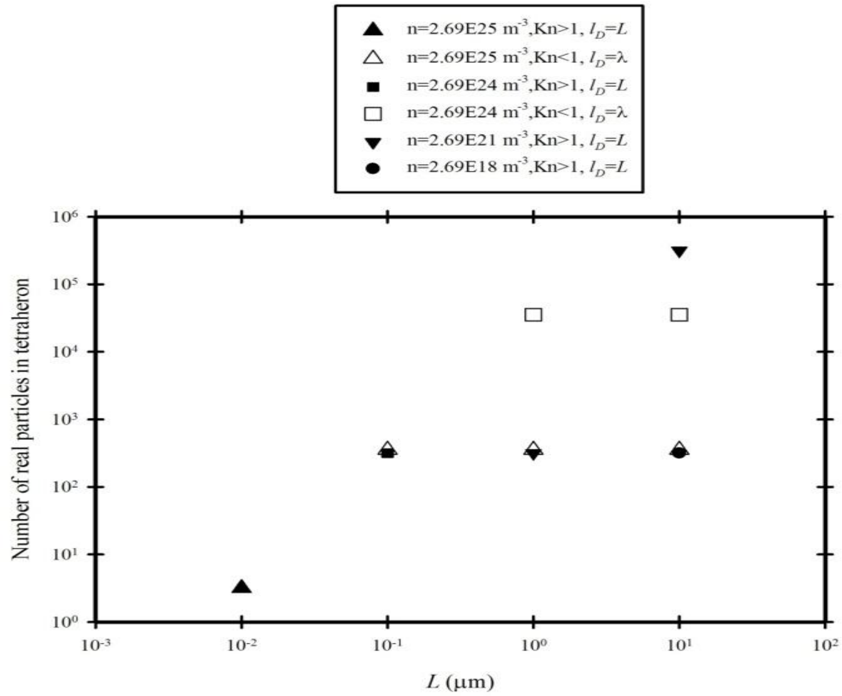

Figure 3-1. Number of real particles inside a tetrahedral cell used in U3DSMC simulation of a domain with a characteristic scale *L* .

We consider a U3DSMC simulation that is required to resolve a region defined by a characteristic scale $L = 10^{-2} - 10\,\mu m$. The number densities considered are $n = 2.69\times 10^{18}, 2.69\times 10^{21}, 2.69\times 10^{24}, 2.69\times 10^{25}\ \mathrm{m}^{-3}$ that are representative of ultra-high, medium, low, standard pressures. For $T = 273\,\mathrm{K}$ and Nitrogen (N_2) gas the corresponding mean-free paths are $\lambda =$ 481×10^{6} nm, 481×10^{3} nm, 481 nm, 48.1 nm. Discretization of the scale L in U3DSMC is obtained with tetrahedra that have edge-length l_D according to

$$\begin{aligned} &\max(l_D) \simeq \lambda \quad \text{for } \lambda < L(\mathrm{Kn} < 1) \\ &\max(l_D) \simeq L \quad \text{for } \lambda > L(\mathrm{Kn} > 1) \end{aligned} \tag{3.17}$$

Following standard DSMC procedures, the Delaunay edge-lengths scale with λ for both Kn conditions indicated above. For cases where the Kn <1 the cell edge-length is bounded by λ, while for Kn >1 the cell are bounded by L.

Figure 3-1 shows the number of real particles in a Delaunay with volume $\Omega_D = \sqrt{2} l_D{}^3 \big/ 12$ and provides an indication on the simulations that can be carried out by U3DSMC. For example, under atmospheric pressures and $L = 0.1, 1, 10\,\mu\mathrm{m}$ the maximum number of real particles in a Delaunay is 354. A U3DSMC simulation is feasible but with a particle weight that is of the order of 10. For $L = 0.01\,\mu\mathrm{m}$ there are only 3 real particles in the Delaunay cell and a DSMC simulation is practically not attainable. For the high-vacuum pressure the only length that can be resolved with U3DSMC is $L = 10\,\mu\mathrm{m}$ all others end up with less than 10 particles in a cell. Figure 3-1 shows clearly the restriction imposed onto DSMC in sub-micron scale domains.

3.2.1 Uniform Nanoscale Flows

These simulations correspond to a uniform flow of N$_2$ with $n_\infty = 2.69 \times 10^{25}\ \mathrm{m}^{-3}$ and $T_\infty = 273$ K with $\lambda_\infty = 48.1\ \mathrm{nm}$ and a characteristic length scale $L = 0.05\mu\mathrm{m}$. This set of conditions corresponds to one of the most restrictive for DSMC computation cases, as indicated in Figure 3-1.

The simulation is realized in a rectangular domain of $(H \times W \times D)$ region shown in Figure 3.2 with $H = W = 0.05\ \mu\mathrm{m}$ and $D = 10\ \mu\mathrm{m}$. A supersonic free stream with $V_\infty = 3369.17\ \mathrm{m/s}$, $M_\infty = 10$ and a subsonic free steam with $V_\infty = 33.69\ \mathrm{m/s}$ $M_\infty = 0.1$ is considered. Free stream conditions are applied on all of boundary surfaces. The simulations were run with $\Delta\tau = 1 \times 10^{-12}$ s which conforms to the DSMC requirement $\Delta\tau V_\infty < l_D$. The system was equilibrated after 10^4 time steps by monitoring the mass flow rate at the exit. The domain is discretized with $G_D = 2446$ Delaunay cells with an $\left\langle \Omega_D \right\rangle = 9.9 \times 10^{-24}\mathrm{m}^3$, average edge-length $\left\langle l_D \right\rangle = 0.0438\,\mu\mathrm{m}$ and average number of real particles $\mathrm{N}_D \simeq 266$. It is clear that for the conditions considered $\max(l_D) \simeq L$, The weight used in the simulations is $F_N = 26$ with $N_D = 10$ computational particle per cell, and $F_N = 9$ with $N_D = 30$.

The results from U3DSMC simulation provided M = 460 samples that are used to evaluate $X \equiv n_D, \mathbf{V}_D, T_D$ following equations ((3.2), (3.4) and (3.6)). The standard-deviation σ_X is evaluated from eq.(3.10), and the fractional error from Eq. (3.11) defines as $E_X(\mathrm{U3DSMC})$. We also evaluate the fraction error using the formulas in eq. (3.14), (3.15) and (3.16) with values from the U3DSMC results. These fractional errors are defined as

$E_X(\mathrm{U3DSMC\ Theory})$. For nitrogen, $\gamma = 1.4$, $c_V = 0.7421\,\mathrm{kJkg^{-1}K^{-1}}$ (Incropera *et al.*, 2006) and $C_V = \frac{3}{2}k_B$ since we are taking the translational temperature fractional error only.

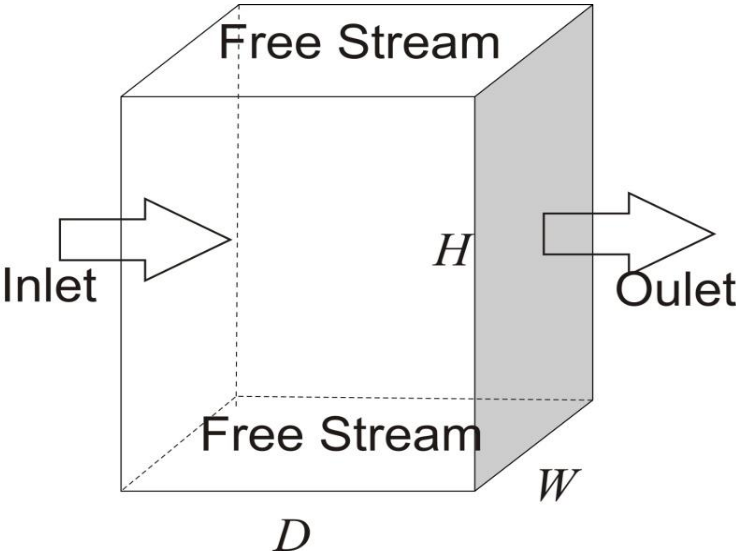

Figure 3-2. Geometry used in the U3DSMC simulation of a nanodomain in a uniform flow.

Figure 3-3 depicts the fractional error as a function of N_D. The results show that U3DSMC simulations using with 10 or 30 computational particles per Delaunay cell have a fractional error that compares very well with the theoretical U3DSMC values, as well as the theoretical error. Figure 3-3 shows that the increase in N_D reduces the numerical error.

Figure 3-4 illustrates the effect of M on the fractional error E_V using the same number of samples as before. The fractional error for the subsonic case $M = 0.1$ is two order of magnitudes larger than the supersonic $M = 10$ a direct result of eq. (3.15). Our results are consistent with similar findings in structured DSMC computations found in Hadjiconstantinou *et al*. (2003).

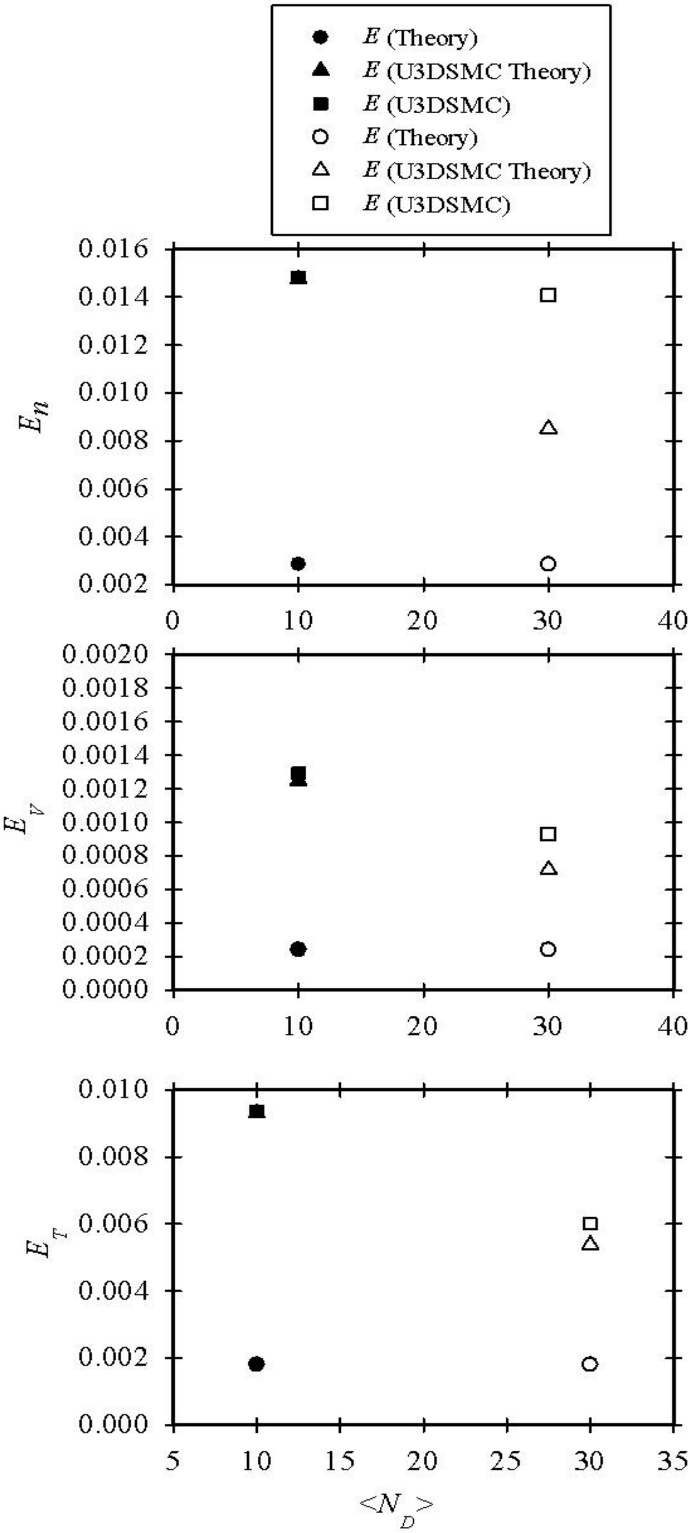

Figure 3-3. Statistical error in density, velocity and temperature for uniform flow as a function of number of computational particles in the Delaunay cell.

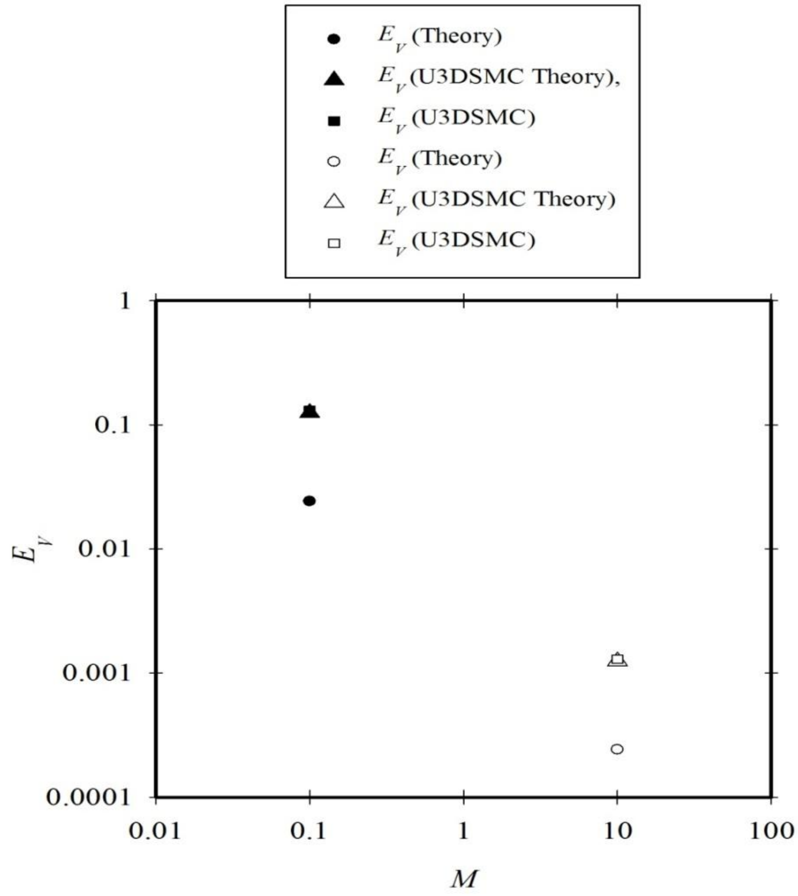

Figure 3-4. Statistical error in mean velocity for the uniform flow as a function of the Mach number.

3.2.2 Pressure Driven Poiseuille Nanoflow

A pressure driven flow of N_2 is simulated using the U3DSMC. The geometry that is considered is a nanochannel of 500 nm height and 100 nm width 4 μm length as indicated in Figure 3-5. The subsonic boundary conditions at the inlet follows of Sec.2.2.3.2. We assume that $n_\infty = 2.69 \times 10^{25}\ \mathrm{m}^{-3}$, $T_\infty = 273\ \mathrm{K}$ corresponding to atmospheric conditions with a $p_\infty = 101325$ Pa (1 atm) and $\lambda_\infty = 48.1$ nm. With P_{in} , and T_{in} specified, V_{in} is obtained and used for particle injection at the inlet boundary during the iteration. The outlet of the nanochannel is placed at the exit boundary of the computational domain as shown in Figure 3-5. The pressure boundary condition is applied at the exit outlet following Sec. 2.2.3.3. With $p_e =$ 10132.5 Pa specified, n_e and V_e are obtained so that injection of particles into the domain proceeds during each time step. The side walls of the nanochannel are of specular reflection while the upper and lower walls are of diffuse type with $T_w = 273\mathrm{K}$, so that the sampling of the velocities at the walls can be preceded.

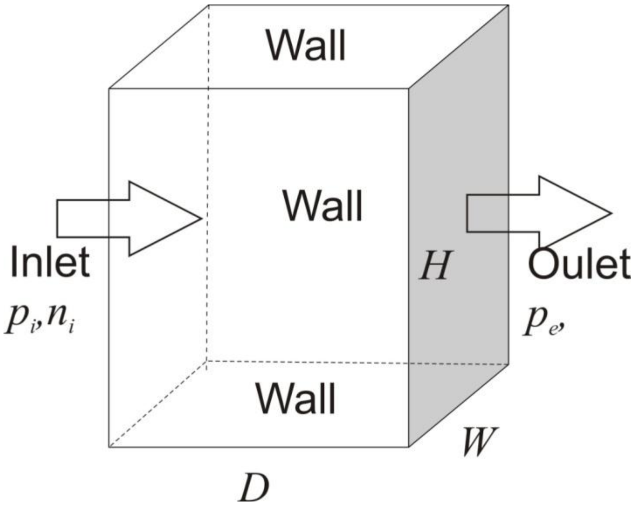

Figure 3-5. Geometry used in the simulation for the pressure driven flow

The characteristic length that needs to be resolved in this U3DSMC simulation is $L \sim 0.1\mu\mathrm{m}$. The simulation domain is discretized with $G_D = 8482$ Delaunay cells with $\left\langle l_D \right\rangle = 0.0463\mu\mathrm{m}$. The average number of real particles inside the cell $\mathrm{N}_D = 315$ particles. The particle weight $F_N = 10$ and $N_D \simeq 31$ upon loading with the free stream distribution. The time step used in the simulations is $\Delta\tau = 1\times 10^{-12}$ s and samples were taken every 100 time steps after 2×10^5 time steps. An M=200 of samples is used in the analysis.

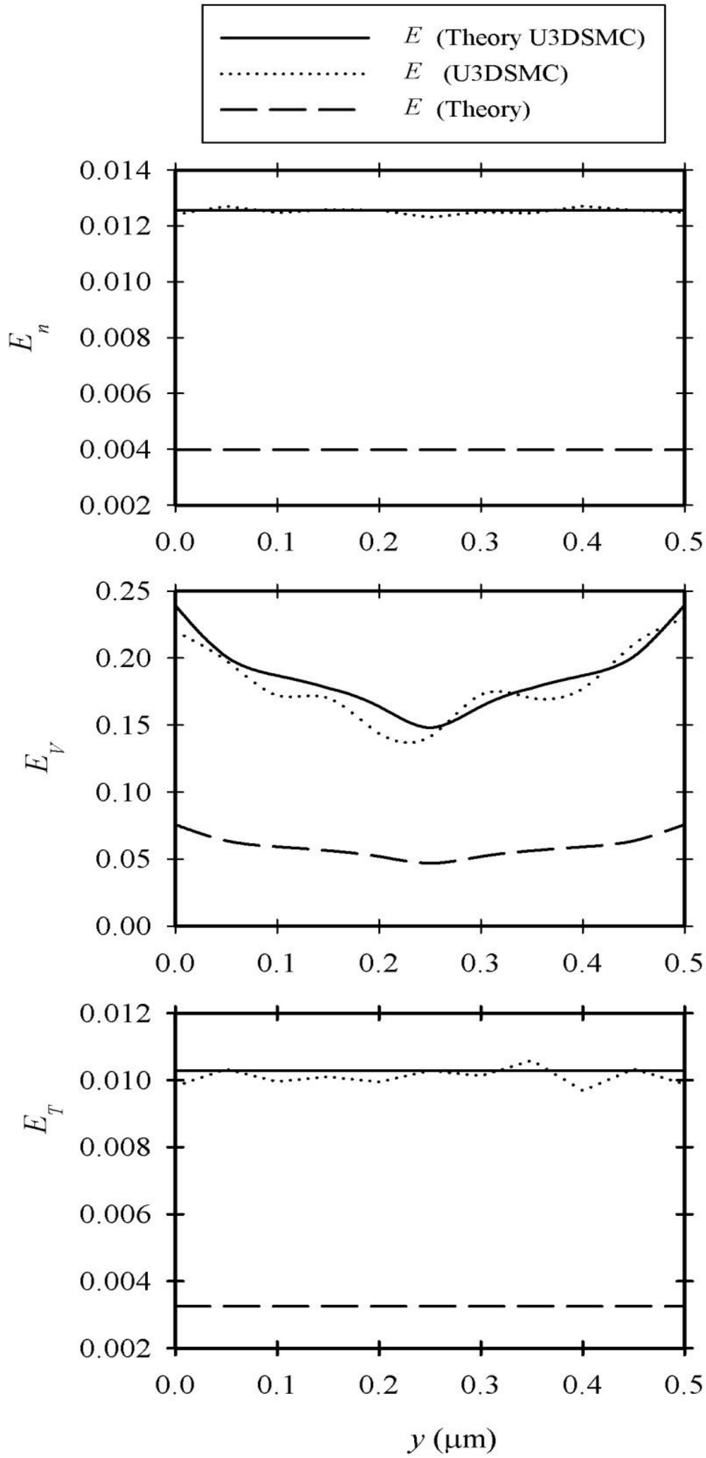

Figure 3-6. Statistical error in the pressure driven flow simulation.

Figure 3-6 shows the fractional error in the number density, mean axial velocity, and temperature as a function of the transverse direction (y). The U3DSMC errors are almost identical with the errors obtained from the theoretical expressions using the local values obtained from the U3DSMC and the real number of particles. The error in density and temperature shows no dependence on the transverse position. The error in mean velocity depends on the position. The minimum error occurs at the center of the channel where the maximum velocity is achieved. These results obtained from the U3DSMC are qualitatively similar to those of Hadjiconstantinou *et al.* (2003) for 2D DSMC simulations on uniform Cartesian grids.

4 U3DSMC SIMULATION OF SUB-ATMOSPHERIC SUPERSONIC FLOWS INTO NANOCHANNELS

In this chapter, the geometric effects, the rarefaction effects, the effects of the speed ratio as well the back pressure effects on the sub-atmospheric supersonic flows into rectangular nanochannels are investigated extensively using U3DSMC. The Knudsen number considered range from 0.481 to 4.81 covering the transitional to the near-free molecular regimes. The height of the nanochannels are 100, 500 and 1000 nm and the aspect ratios are 1, 10 and 100. The speed ratio is 2, 5 and 10. The effects of back pressure are considered with pressure in the range from 0-200 kPa. The application of the subsonic outlet boundary condition is utilized in several simulations in which the exit pressure is implemented and fixed throughout the simulations while the exit number density and velocity are floating (Sec. 2.2.3.3). The heat flux to the wall obtained from U3DSMC is compared to the values of the heat transfer rates obtained from the free molecular theory. The mass flux at the exit of the nanochannel is also compared to the theory of Hughes and de Leeuw (1965). Grid sensitivity analysis is carried out to study the effects of the cell size edge length on the U3DSMC simulations. The analysis utilizes the phase-space plots resulting from the U3DSMC methodology as well as the centerline macroscopic sample-averaged properties. The material of this chapter appears in Gatsonis *et al.* (2009).

4.1 Free Stream, Boundary Conditions And Computational Parameters

The supersonic flow into a rectangular nanochannel is investigated with the U3DSMC code for the geometry shown in Figure 1-2. The simulation domain features a buffer region with length L_B, shown in Figure 4-1, followed by the nanochannel with length, height and width L, H, W respectively. The cases are summarized in Table 4-1.

The flow is characterized by the Knudsen number, where

$$Kn = \frac{\lambda}{H} = \frac{1}{\sqrt{2}\pi {d_{ref}}^2 n \left(T_{ref}/T\right)^{\omega-1/2}} \frac{1}{H} \tag{4.1}$$

with $d_{ref} = 4.17 \times 10^{-10}$ m, $T_{ref} = 273$ K and $\omega = 0.74$ (Bird, 2004) which is the viscosity index for the VHS molecule. The local speed-ratio is defined in eq. (2.28) and the Mach number is given in terms of the specific heat ratio γ

$$M = V \Big/ \sqrt{\frac{\gamma k T}{m}} \tag{4.2}$$

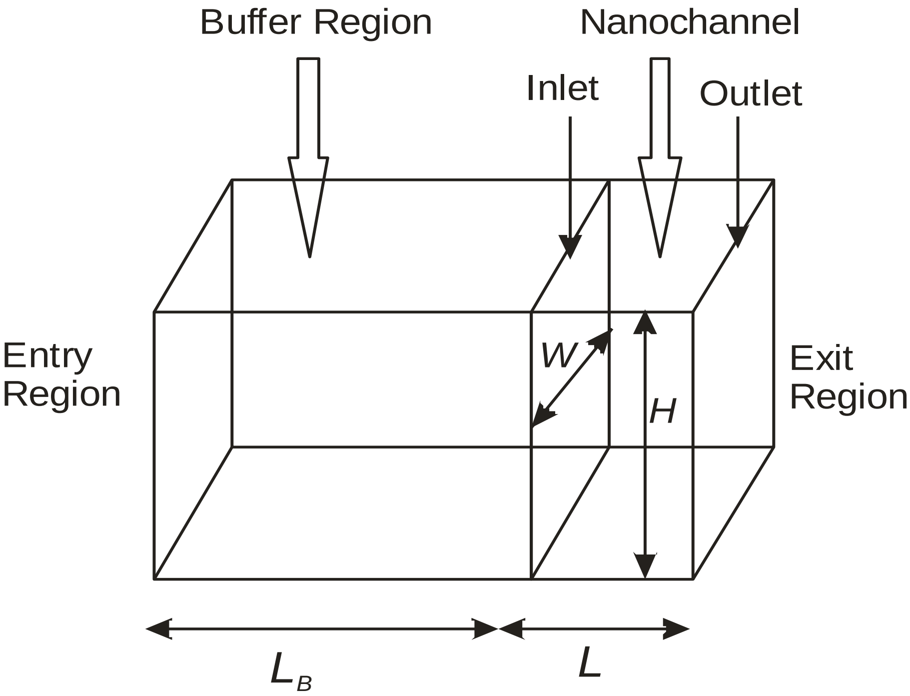

Figure 4-1. Geometry of the domain used in the U3DSMC simulations (dimensions are not to scale).

Table 4-1. Physical and computational parameters for U3DSMC simulations of nitrogen nanochannel flows.

Case	H (nm)	L/H	S_∞	M_∞	P_b (kPa)	Kn_∞	L_B (nm)	G_D	$\langle l_D \rangle$ (nm) [$\sigma(l_D)$]	F_N	$\langle N_D \rangle$ [$\sigma(N_D)$]
1	100	1	5	5.97	0	4.81	1000	132	85.8 [8.74]	20	11.21 [4.44]
2	100	10	5	5.97	0	4.81	1000	252	85.2 [7.2]	20	10.67 [3.78]
3	100	100	5	5.97	0	4.81	1000	504	122 [17.8]	20	29.36 [10.96)]
4	500	1	5	5.97	0	0.962	1000	1544	118 [12.1]	20	32.67 [11.93]
4a	500	1	5	5.97	120	0.962	100	1544	118 [12.1]	20	32.67 [11.93]
4b	500	1	5	5.97	200	0.962	100	1544	118 [12.1]	20	32.67 [11.93]
5	500	10	5	5.97	0	0.962	1000	5836	129 [11.4]	20	34.57 [11.03]
5a	500	10	5	5.97	40	0.962	1000	5836	129 [11.4]	20	34.57 [11.03]
5b	500	10	5	5.97	100	0.962	1000	5836	129 [11.4]	20	34.57 [11.03]
6	500	100	5	5.97	0	0.962	1000	48576	135 [9.26]	20	35.30
7	1000	1	5	5.97	0	0.481	1000	8276	125 [10.4]	20	32.5 [11.00]
8	1000	10	5	5.97	0	0.481	1000	45194	128 [10.1]	20	72.1 [10.5]
9	1000	100	5	5.97	0	0.481	3000	425576	400 [34.8]	100	199.51 [74.38]
10	500	10	2	2.39	0	0.962	1000	5836	129 [11.4]	20	34.57 [11.03]
11	500	10	10	11.95	0	0.962	1000	5836	129 [11.4]	20	34.57 [11.03]

Rectangular nanochannels with $H = W = 100 - 1000$ nm, AR=1, 10, 100 are considered in the simulations with input parameters shown in Table 4.1

The incoming nitrogen N_2 flow has $n_\infty = 2.69 \times 10^{24} \mathrm{m}^{-3}$, $T_\infty = 273\mathrm{K}$, corresponding to $P_\infty = 0.1$atm (10.132 kPa) and $\lambda_\infty = 481$ nm. Cases 1-9 have $V_\infty = 2013$ m/s, $S_\infty = 5$ and $M_\infty = 5.97$. Case 10 has $V_\infty = 805.2$ m/s, $S_\infty = 2$, $M_\infty = 2.39$. Case 11 has $V_\infty = 4026.8$ m/s, $S_\infty = 10$ and $M_\infty = 11.95$. In the simulations we consider the rotational but neglect the vibrational degrees of freedom of nitrogen.

In order to allow for the undisturbed free stream conditions to be realized far from the nanochannel inlet we include a buffer region of length L_B ahead of the nanochannel inlet. Molecules are injected through the boundaries of the buffer region based on eq. (2.31) with specified $n_\infty, T_\infty, V_\infty$. The sides of the buffer region are modeled as a free stream. Particles that move upstream and reach the surfaces of the buffer region are removed from the computational domain.

The outlet of the nanochannel is placed at the exit boundary of the computational domain as shown in Figure 4-1. A vacuum boundary condition is set for Cases 1-11, where the back pressure is specified as $P_b = 0$ at the exit region. Any particle reaching the exit plane is removed from the domain and no particles are allowed to enter the computational domain through the exit plane. For Cases 4a, 4b and 5a, 5b a finite back pressure P_b is specified at the exit. The upper and lower walls, as well as the side walls of the nanochannel, are modeled as fully diffuse and the temperature of the wall equals that of the free stream distribution. The simulation domain is loaded initially with a uniform drifting gas following eq. (2.24) based on the free stream conditions in Figure 4-1.

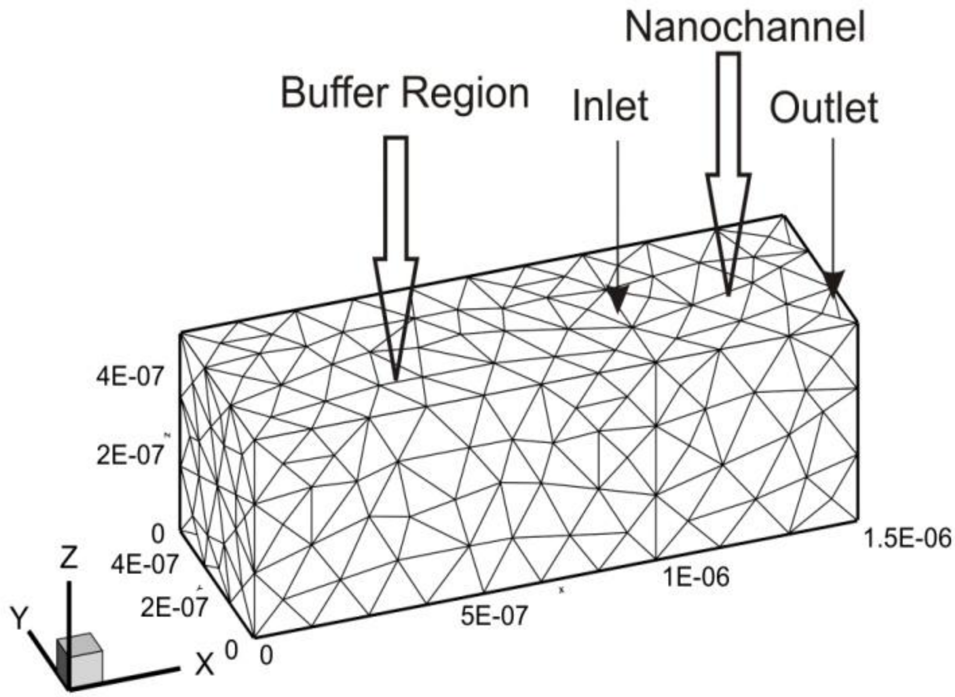

Figure 4-2. Typical grid used in U3DSMC simulations (Case 4) showing the surface elements of the Delaunay tethrahedra.

Figure 4-2 displays the boundary faces of the Delaunay cells of a typical mesh used in the simulations. The interior is discretized with Delaunay tethrahedra cells with edge-lengths that are smaller than λ_∞. The mean of the Delaunay edge lengths $\left\langle l_D \right\rangle$ in Table 4-2 show that they are smaller than the corresponding $\lambda_\infty = 481$ nm. The total number of Delaunay cells in the domain G_D, the average number of simulated particles in each cell $\left\langle N_D \right\rangle$ and its standard deviation $\sigma(N_D)$ are provided in Table 4-2. These parameters show that the Delaunay cells are populated at initialization with at least 10 computational particles.

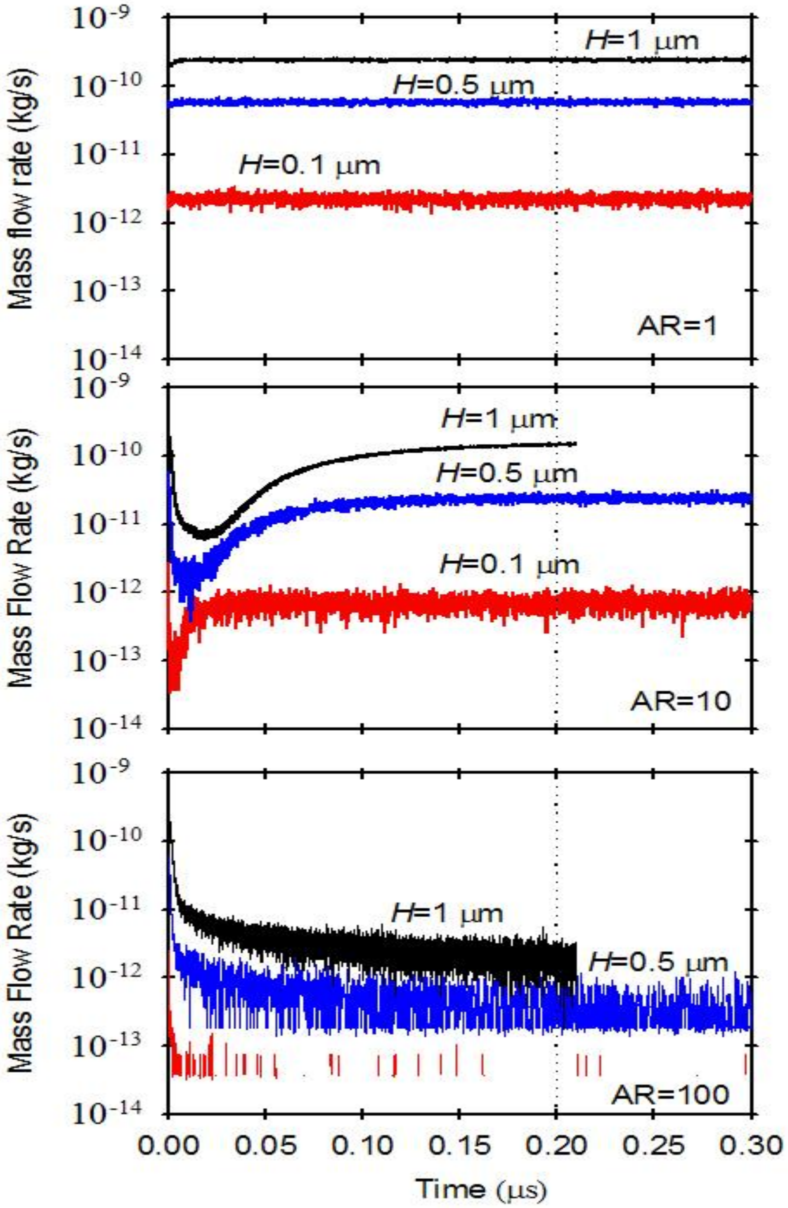

Figure 4-3. Steady state time determination from mass flow rate at the outlet of the nanochannel with $P_\infty = 0.1$ atm.

The simulations were run with a time step $\Delta\tau = 1\times10^{-12}$ sec, and the steady state time was determined from the mass flow rate obtained at the outlet of the nanochannel, as shown in Figure 4-3. After reaching the steady state time of 0.2 μsec, 100 independent samples were taken every 100 timesteps, and averaged to produce the steady-state flow properties.

4.2 Grid Sensitivity Analysis

The cell size is an important parameter in a DSMC simulation and for microflows it has been examined extensively for 2D uniform grids (Garcia *et al*, 1998; Hadjiconstantinou, 2000). For the unstructured 3D simulations in this work the grid is generated using nearly equally sized tetrahedra. While the distribution of edge-lengths is nearly uniform, the mean $\left\langle l_D \right\rangle$ is the proper representative cell scale. The grid sensitivity analysis studies the effect of increasing the cell size using as baseline parameters presented in Table 4-2 and comparing macroscopic flow parameters such as density, flow velocity and translational temperature.

Table 4-2. U3DSMC Simulation parameters used in the grid sensitivity study.

Case	$\left\langle l_D \right\rangle$(nm) [λ]	$\sigma(l_D)$ (nm)	$\left\langle N_D \right\rangle$	$\sigma(N_D)$
2	85.2 [1/5.6]	8.74	11.21	4.44
GS-2	136 [1/3.4]	11.7	35.87	13.73
4	129 [1/3.4]	11.4	34.57	11.03
GS-4	205 [1/2.3]	17	57.5	11.2

Results for the two most restrictive Cases 2 and 4, i.e. nanochannels with the small inlets and aspect ratios, are discussed below. Input parameters of Case 2 and Case 4 are used in simulations GS-2 and GS-4, nearly doubling the edge-length l_D while keeping the particle weight constant at $F_N = 20$. The resulting $\left\langle l_D \right\rangle$ and $\left\langle N_D \right\rangle$ are shown in Table 4-2.

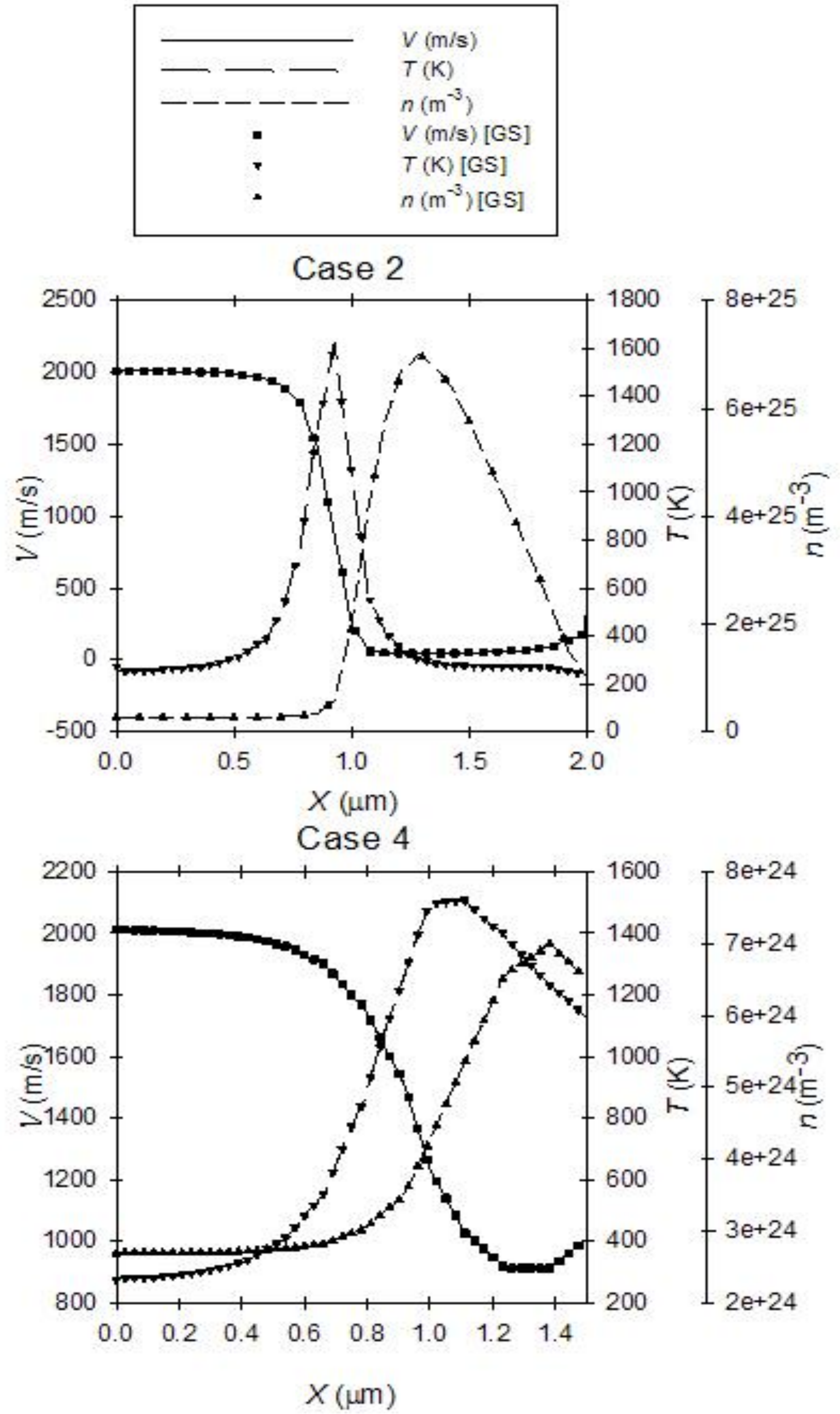

Figure 4-4. Centerline values of n, V_x, T from U3DSMC simulations. Top: Case 2 (lines) and Case GS-2 (symbols) Bottom: Case 4 (lines), Case GS-4 (symbols).

Centerline values for the number density, translational temperature, and mean velocity are shown in Figure 4-4. Case 2 and Case GS-2 represent a near free-molecular flow with $Kn_{\infty} = 4.81$, $H = 0.1\,\mu\mathrm{m}$ and AR=10. Figure 4-4 shows that doubling the size of the edge-length, while keeping it smaller than λ_{∞}, has no effect on centerline flow properties. Case 4 and Case GS-4 correspond to a transitional flow with $Kn_{\infty} = 0.962$, $H = 0.5\,\mu\mathrm{m}$ and AR=1. A comparison between Case 4 and GS-4 flow properties in Figure 4-4 shows that the doubling of the edge-length has no effect on the centerline flow properties. These results obtained for the most restrictive cases, provide evidence that the choice of computational parameters used in the nanoscale simulations, provide sufficient numerical resolution.

4.3 Results And Discussion

4.3.1 Effects of Nanochannel Inlet Size and Aspect Ratio

These effects are examined with Case 1 to Case 9 simulations shown in Table 4-1. In these cases, the inlet height of the nanochannel was changing to be either 0.1 or 0.5 or 1 μm and the aspect ratio, which is the ratio between the length to the height of the nanochannel, will be either 1, 10 or 100. The inlet height establishes the free stream Knudsen number and characterizes the rarefaction effect which was varying to cover the slip, transitional and the early free molecular regimes. The aspect ratio, AR, establishes the flow development due to particle-wall interactions with the diffuse walls of the nanochannel.

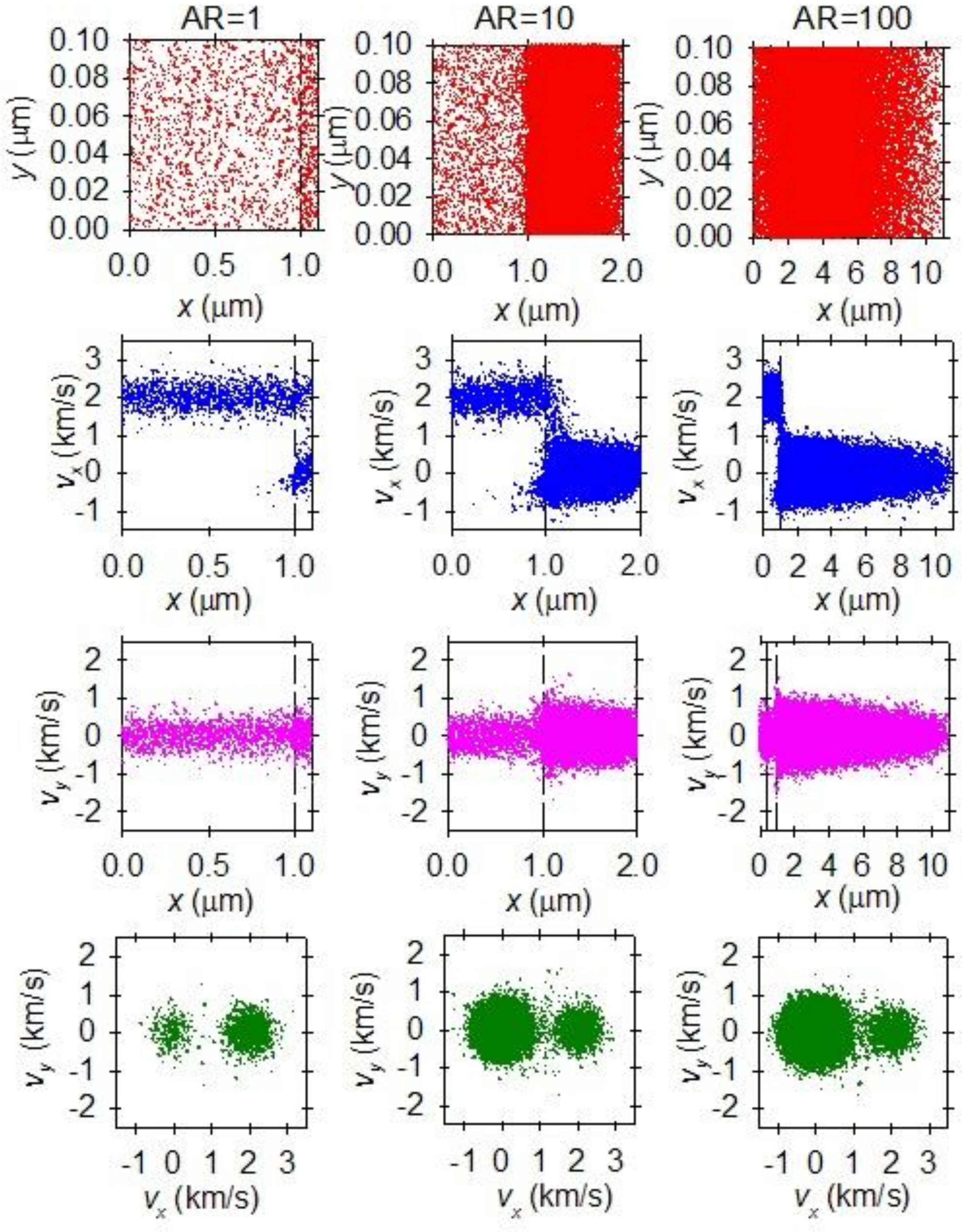

Figure 4-5. Effects of AR for *H*=0.1 μm nanochannels. Phase plots (x, y), (x, v_x), (x, v_y) and (v_x, v_y) for Case 1, 2 and 3.

The phase space for Cases 1, 2 and 3 is presented in Figure 4-5. These cases simulate the smallest nanochannels with $H = 0.1\,\mu\mathrm{m}$ and correspond to the near free-molecular flow with a $Kn_{\infty} = 4.81$. The (x, y) phase plot shows the number density to increase inside the AR=1 nanochannel. The AR=10, and AR=100 nanonchannels show an increase in the number density followed by a decrease at the end of the nanochannel. The (x, v_x) phase plot shows the high-speed free-stream population to permeate the entire length of the AR=1 nanochannel. The (x, v_x) plot shows that inside the AR=1 nanochannel a low-speed population develops as a result of collisions of particles with the walls. In addition, a small population of upstreaming particles exit from the inlet after colliding with the walls or other particles in the density enhancement region. The (x, v_x) plot for the AR=10 and AR=100 cases shows that the high-speed component does not permeate the entire length of the nanochannel. Instead, the nanochannel is populated with near zero-drift particles, due to diffuse reflections off the walls. The (x, v_x) phase space for AR=10 and AR=100 shows that the spread of the v_x component is reduced towards the exit. Both phase plots exhibit the upstreaming particles.

The (x, v_y) phase plots in Figure 4-5 show that the *y*-component of the velocity increases inside the nanochannel as a result of the collisions in the density enhancement region. As the AR increases from 1 to100, the velocity spread decreases with increasing length, due to diffuse reflections off the walls. The (v_x, v_y) phase plots in Figure 4-5 corroborate the previous results. The AR=1 nanochannel shows the appearance of a symmetric, free-streaming population and a secondary, symmetric, zero-drift population that arise due to collisions with the wall. This zero-drift population becomes the dominant feature of the flow as the AR increases. It is also noticeable that the spread, that is the temperature of the low-drift population, is larger than the free-stream value as a result of collisions inside the nanochannel. The symmetry of the low-speed population is indicative of gas-wall equilibration phenomena inside the nanochannel

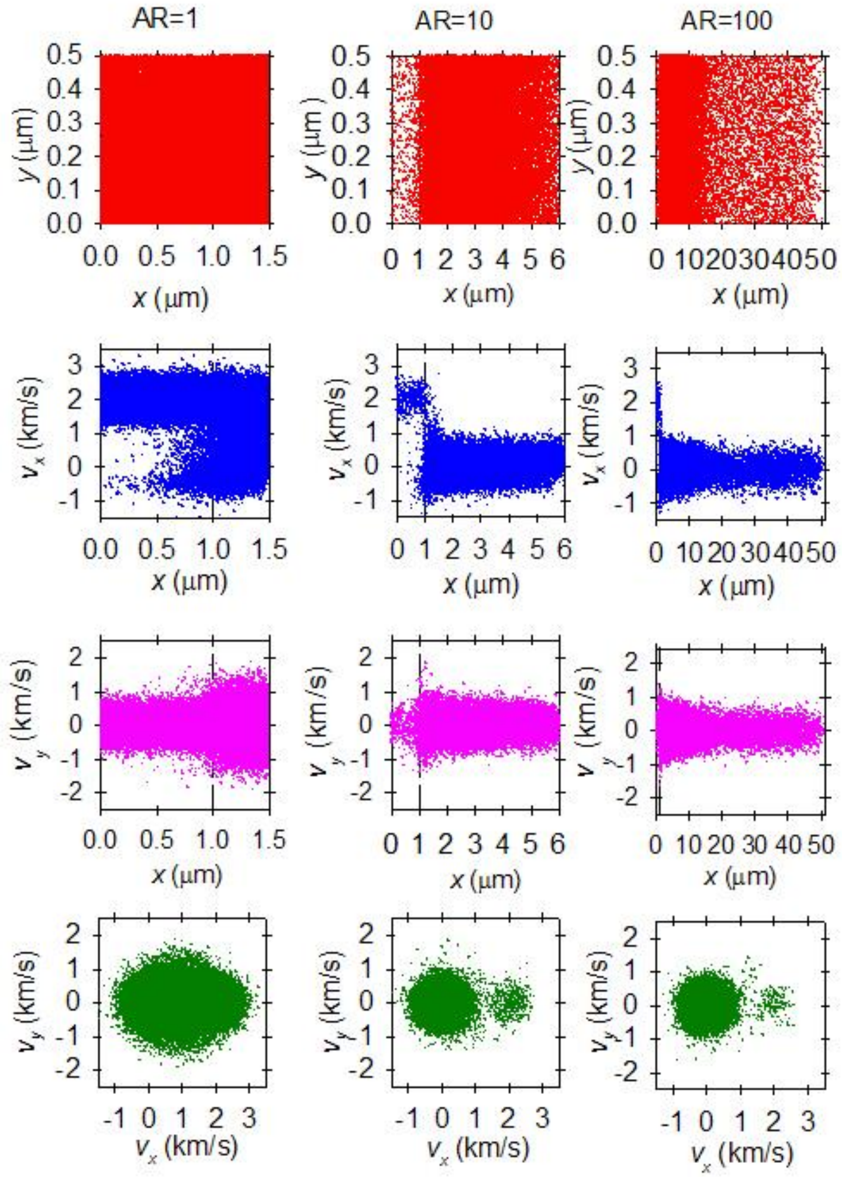

Figure 4-6. Effects of AR for *H*=0.5 μm nanochannels. Phase plots (x,y), (x,v_x), (x,v_y) and (v_x,v_y) for Case 4, 5 and 6.

Figure 4-6 depicts the phase-space for Cases 4, 5 and 6 where the nanochannel inlet is designated by the dashed line. The nanochannel has $H = 0.5\,\mu\mathrm{m}$ and corresponds to the transitional regime with a $Kn_{\infty} = 0.962$.

The (x, y) phase space in Figure 4-6 shows that the number density is nearly uniform inside the AR=1 nanochannel. For the AR=10 and AR=100 nanochannels, the density enhancement is followed by a density reduction region towards the outlet. The (x, v_x) phase space in Figure 4-6 shows the high-speed free-stream population to permeate the entire length of the AR=1 nanochannel but reduces to a low-speed population for the long nanochannels. The (x, v_y) phase plots in Figure 4-6 show that the spread in v_y increases in the inlet of the nanochannel for all ARs considered. This behavior, similar to the $H = 0.1\,\mu\mathrm{m}$ cases, is a result of collisions within the density enhancement region. For the AR=10 and AR=100 nanochannels the spread in v_y decreases gradually towards the outlet due to the collisions with the diffuse type of reflection walls.

The (v_x, v_y) phase space plots in Figure 4-6 display a similar behavior to those of Figure 4-5. For all ARs considered, the primary population is the zero-drift population that arises due to collisions with the walls. The secondary population belongs to the high-speed free-streaming particles. And it is very obvious that the low-speed population is becoming the dominant as the aspect ratio is increasing. The symmetry of the low-speed population is an indication of the gas-wall equilibration phenomena inside the nanochannel.

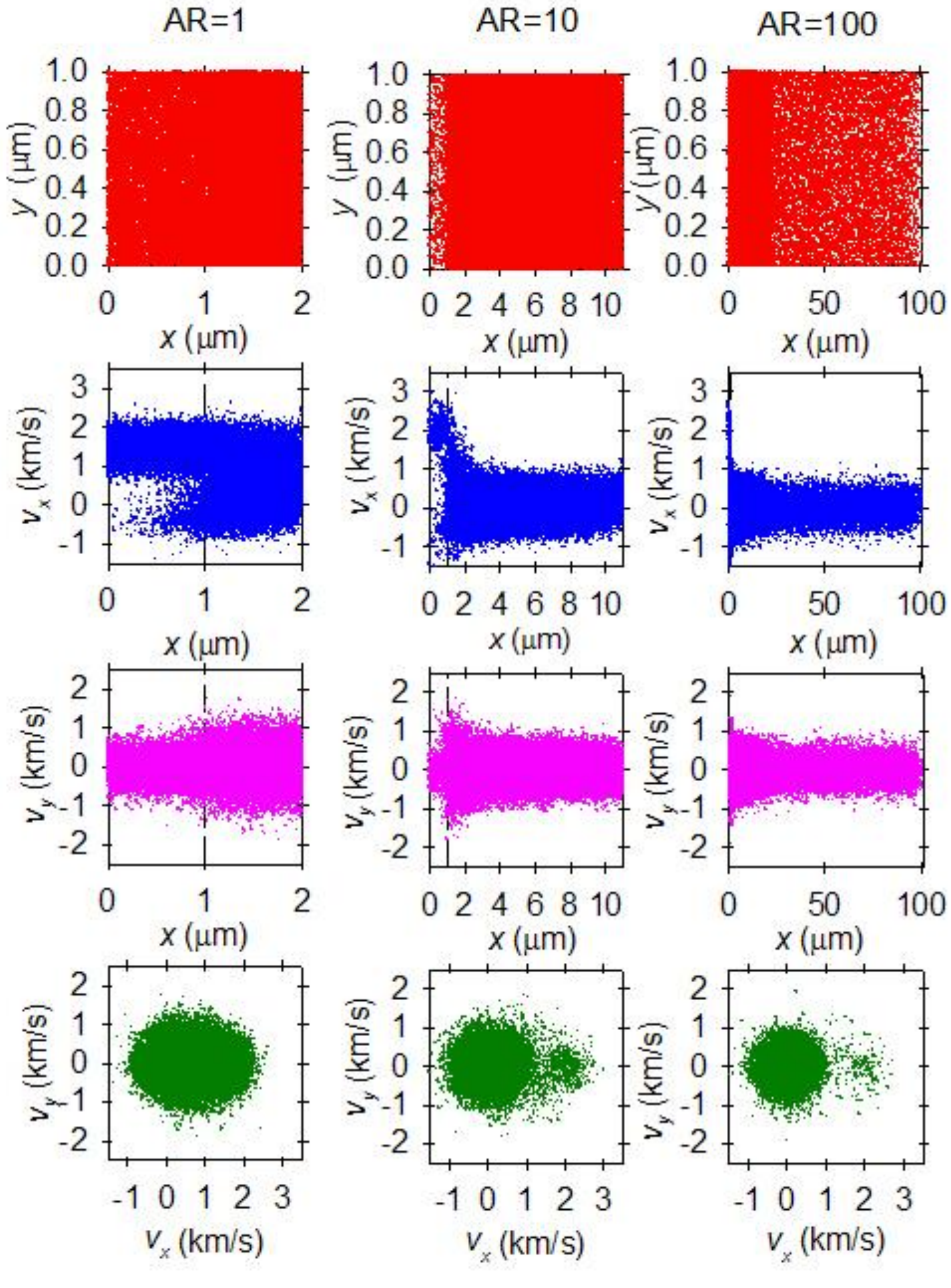

Figure 4-7. Effects of AR for *H*=1 μm nanochannels. Phase plots (x,y)**,** (x,v_x)**,** (x,v_y) **and** (v_x,v_y) **for Case 7, 8 and 9.**

Figure 4-7 plots the phase space for Cases 7, 8 and 9 that simulate $H = 1\mu\mathrm{m}$ nanochannels in the transitional regime with a $Kn_\infty = 0.481$. The (x, y) phase plot shows the number density to increase inside the *AR*=1 and AR=10 nanochannels. The AR=100 nanochannel shows a density increase in the inlet region followed by a gradual density reduction towards the outlet. The (x, v_x) phase plot exhibits characteristics similar to those depicted for Cases 4, 5, and 6. The high-speed population permeates the entire AR=1 nanochannel, but only a small portion of the AR=10 and AR=100 nanochannels. All ARs considered show the development of the bakcstreaming flux into the buffer region from particles emanating from the inlet of the nanochannel due to the collisions with the walls and the other particles in the density enhancement region.

The (x, v_y) phase plots in Figure 4-7 show an increase in the spread of v_y that begins in the inlet region because of the collisions with other particles in the density enhancement region. The spread remains almost uniform further downstream. For the AR=10 and AR=100 cases the distributions of v_x and v_y are symmetric inside the nanochannels indicating equilibration due to wall collisions.

The (v_x, v_y) phase plots in Figure 4-7 show the development of a symmetric, zero-drift population which is the result of collisions in the density enhancement region, as well as wall collisions. The high-speed population retains the characteristics of the incoming supersonic flow. The low-speed population is becoming the dominant feature as the aspect ratio of the nanochannel is increasing.

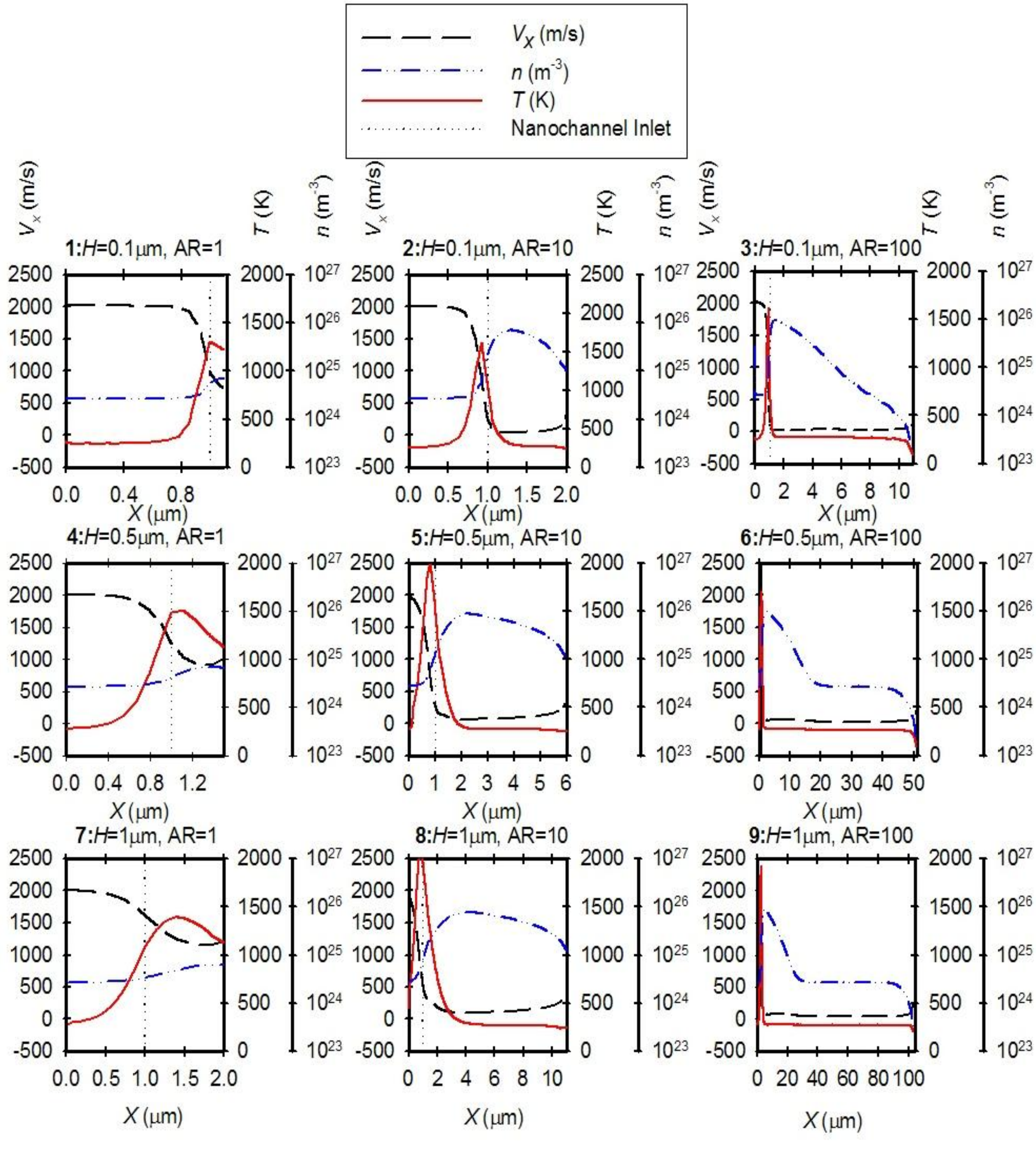

Figure 4-8. Centerline macroscopic flow properties in the computational domain for Cases 1-9. The inlet is indicated by the dotted line with the buffer region ahead of the nanochannel.

In Figure 4-8. we plot the macroscopic fluid properties along the centerline of the nanochannel and the buffer region. They include the number density from eq. (2.73), the average velocity V_x from eq. (2.74), and the translational temperature T from eq. (2.77). These macroscopic variables are sampled in Delaunay cells, shown in Figure 2-2, that occupy a considerable fraction of the nanochannel at a given downstream position. With a few sampling cells spanning the width of the nanochannel it is not feasible to obtain a meaningful spatial resolution and construct contour plots. In Figure 4-8, the free stream boundary conditions on the velocity, temperature and the number density are clearly imposed at the entry plane and persist throughout the buffer of the simulated region for the cases of AR= 1 nanochannel.

The number density shows the formation of the density enhancement that becomes stronger with increasing AR for all Knudsen numbers considered. The density decreases inside the nanochannel and the trend is more pronounced with the larger AR cases. The density enhancement is explained physically with the phase plots discussed earlier. The average velocity shows the free stream velocity followed by a reduction near the inlet of the nanochannel for all cases considered.

The temperature shows an enhancement in the inlet region and it is associated with the presence of the high-speed and low-speed particle populations shown in the phase plots of Figure 4-5, Figure 4-6 and Figure 4-7. The temperature after the inlet region shows a sharp decrease and remains almost constant for the AR=10 and AR=100 nanochannels indicating equilibrium with the wall temperature.

Table 4-3. Position and magnitude of centerline maximum temperature and number density from U3DSMC simulations.

Case	$X(T_{\max})$ (μm)	$T_{\max}$ (K)	$X\ (n_{\max})$ (μm)	$n_{\max}$ (m^{-3})
1	1.0	1304	1.1	7.060E+24
2	0.9	1620	1.3	7.000E+25
3	0.9	1617	1.4	9.540E+25
4	1.0	1498	1.4	6.990E+24
5	0.8	1978	2.2	8.690E+25
6	0.9	1691	2.0	9.800E+25
7	1.4	1389	1.9	6.200E+24
8	0.9	2070	4.1	7.680E+25
9	1.0	1802	3.0	8.980E+25

The position and magnitude of the maxima of density and translational temperature are shown in Table 4-3. For all cases considered the density maximum is located near the inlet but inside the nanochannel. The temperature maximum is located before or at the inlet of the nanochannel. This behavior where density and temperature enhancement do not coincide has been observed in rarefied high-speed flows into macroscale tubes by Gatsonis *et al*. (1997) as well microchannels (Oh *et al*., 1997, Liou *et al*., 2001, Le and Hassan, 2007). The nanochannel acts a solid body to the incoming flow and reflected particles from the wall generate this perturbation region which is similar to a diffuse shock formed in front of a solid body in a high-speed rarefied gas flow.

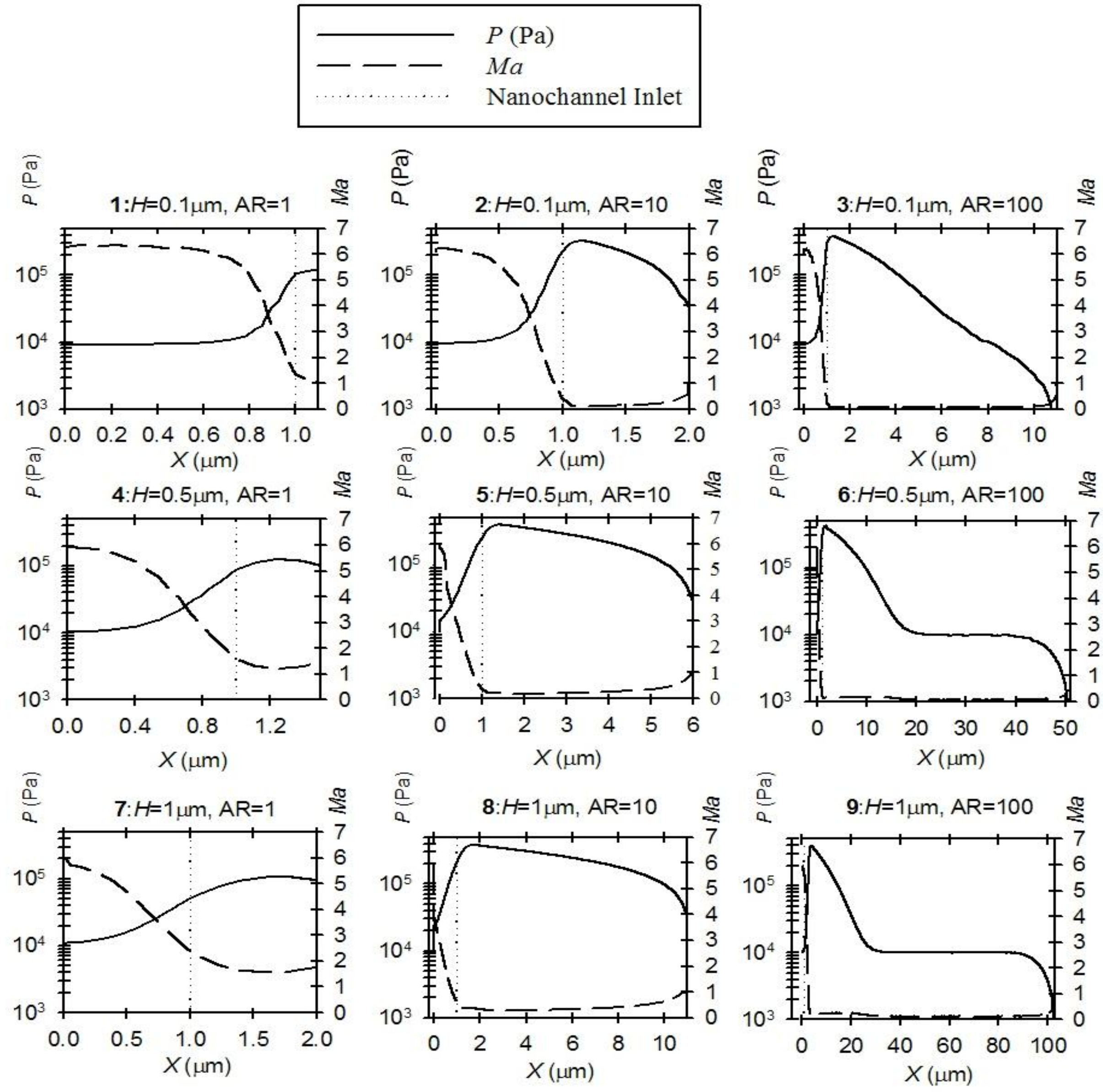

Figure 4-9. Centerline Mach number and pressure in the computational domain for Cases 1-9. The inlet is indicated by the dotted line with the buffer region ahead of the nanochannel.

In Figure 4-9, the centerline pressure from eq. (2.11) and the Mach number (which is the ratio of the local velocity to the local speed of sound) are plotted for Cases 1-9 which are specified in Table 4-1.

The AR=1 nanochannels show that the Mach number is supersonic at the inlet and remains supersonic for the three Knudsen numbers considered. The centerline pressure increases from its free stream value and decreases slightly towards the outlet. The inlet of the nanochannel is designated by the dotted line.

The nanochannels with AR=10 and AR=100 result in a subsonic inlet Mach number and a sharp increase in pressure near the inlet. The Mach number, subsequently, increases and reaches the sonic point of Mach number of 1 at the outlet for all cases considered. The flow therefore, is choked at the outlet of the nanochannel.

For the supersonic inlet (Case 1, 4 and 7) in the AR=1 nanochannels, the Mach number remains supersonic at the outlet. For cases where the inlet Mach number becomes subsonic the flow becomes sonic at the exit and the flow is choked.

The pressure in Figure 4-9 shows a sharp increase in the density enhancement region near the inlet followed by a decrease towards the end of the channel. In all of the cases investigated in Figure 4-9, none of them has an exit pressure to match the imposed pressure at the outlet of the nanochannel which is the vacuum pressure. This implies the necessity of applying a back pressure so that eventually the exit pressure will be matching the back pressure implemented. This investigation will be studied extensively with details in (Sec.4.3.3) by implementation of the subsonic outlet boundary condition using a fixed pressure at the outlet of the nanochannel throughout the duration of the simulations and a floating velocity and number density at the exit of the nanochannel.

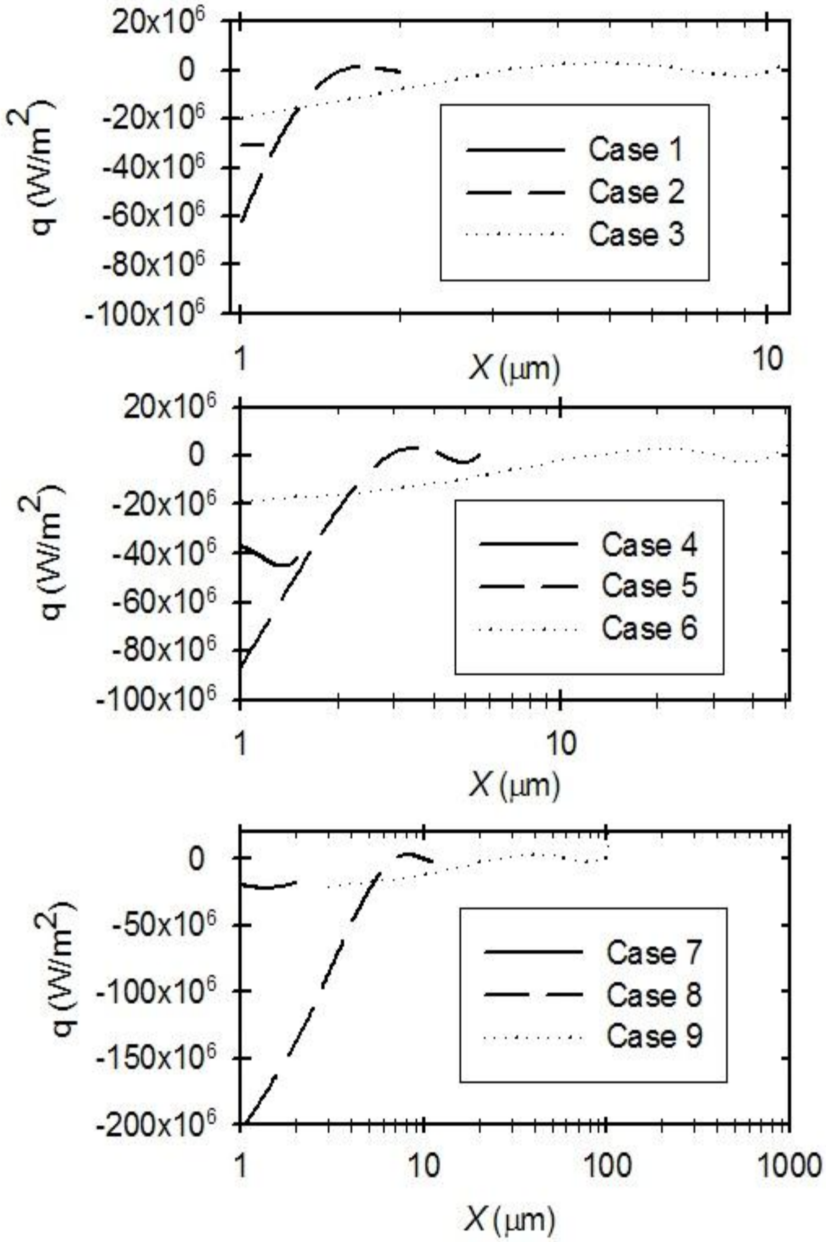

Figure 4-10. Heat flux to the wall of the nanochannel (Case 1-9).

The physical picture that emerges from these nanochannel simulations can be explained with arguments drawn from compressible, viscous flows with friction and heat loss. The heat flux obtained from eq. (4.3) to the constant temperature wall is plotted in Figure 4-10.

A comparison between the numerical values and theoretical values can be obtained for Cases 1, 2, 3 that correspond to near-free molecular flows at $Kn_{\infty} = 4.51$. The free molecular, total translational and internal energy flux (or heat transfer rate) from a free stream with ρ, T, S to a flat plate with surface temperature T_r aligned with the flow is,

$$q_{th} = nm\left(\frac{2kT}{m}\right)^{3/2}\frac{(1-\varepsilon)}{4\pi^{1/2}} \left(\left[S^2+\frac{\gamma}{\gamma-1}-\left\{\frac{1}{2}\frac{\gamma+1}{\gamma-1}\right\}\frac{T_r}{T}\right]\left[\exp\left(-S^2\right)+\pi^{1/2}S\left\{1+erf\left(S\right)\right\}\right]-\frac{1}{2}\exp\left(-S^2\right)\right) \tag{4.4}$$

where ε is the fraction of molecules that is reflected specularly [Sec.7, Bird, 2004]. Substituting in eq. (4.4) values for ρ, T, S from the U3DSCM results sampled at the inlet of the nanochannel we obtain theoretical values of heat flux. For Case 1, $q_{th} = -52.4 \times 10^6$ W/m^2 with the numerical $q = -31.3 \times 10^6$ W/m^2. For Case 2, $q_{th} = -93.7 \times 10^6$ W/m^2 and $q = -62.5 \times 10^6$ W/m^2. For Case 3, $q_{th} = -42.5 \times 10^6$ and $q = -19.8 \times 10^6$ W/m^2. The numerical values are, therefore, within the order of magnitude of the theoretical estimates.

The short nanochannels AR=1 for Cases 1, 4 and 7 result in an almost uniformly distributed heat loss to the wall. This heat flux coincides with the temperature enhancement region that permeates these short nanochannels as Figure 4-8 shows. These flows remain supersonic at the inlet as Figure 4-8 and Figure 4-9 show, then slow down due to the friction effect at the first portion of the nanochannel in which the temperature is increased while the velocity is decreased in a fashion that is very similar to Fanno flow. In the next part of the nanochannel the flow velocity increases while the temperature decreases due to the cooling of the flow. This behavior is similar to a Rayleigh flow when frictional effects are not important.

For the AR=10 and AR=100 nanochannels (Cases 2, 3, 5, 6, 8, 9) the heat flux to the wall shown in Figure 4-10 is non-uniform. It is largest (negative) in the temperature enhancement region near the inlet. These subsonic flows decelerate within the region of the heat loss, consistent with the Rayleigh flow analogy. For the remainder of the nanochannel the heat flux to the wall is greatly diminished in magnitude as the fluid temperature remains almost in equilibrium with the wall. The flows after the heat loss region, as Figure 4-8 and Figure 4-9 show, accelerate and become sonic at the exit. In this later region of the nanochannel the flow behavior is closer to a Fanno flow analogy. The continuum fluid interpretation is corroborated by the phase plots presented in Figure 4-5, Figure 4-6 and Figure 4-7.

The outgoing mass flow rate obtained at the outlet from U3DSMC is compared with estimates obtained using the semi-analytical theory developed for the free-molecular regime by Hughes and de Leeuw. For a cylindrical tube with aspect ratio $D = d / L$, a drifting Maxwellian with a speed ratio at zero angle of attack with the tube axis will have a flux of particles exiting at the outlet into a background of specified pressure given by

$$N(S_{\infty}, D, 0) = \frac{n_{\infty} C_{m\infty}}{2\sqrt{\pi}} \pi r^2 \int_{0}^{\pi/2} K(\phi, D) F(\phi, S_{\infty}, 0) d\phi \tag{4.5}$$

In the above, $C_{m\infty}$ is the most probable speed. The quantity $K(\phi, D)$ is the ratio between the number flux of molecules exiting at the outlet of the tube, and the number flux of particles that enter the tube due to a beamlet with an angle ϕ with the tube axis. Hughes and de Leeuw evaluate $K(\phi, D)$ using the Clausing's probability function for particle transmission after wall reflections. The flux term in eq. (4.5) that strikes a surface perpendicular to the tube axis at an angle between ϕ and $d\phi$, is,

$$F(\phi, S, 0) = \sin\phi\cos\phi[(1 + S^2\cos^2\phi)\exp(-S^2) + \pi^{1/2}S\cos\phi\exp(-S^2\sin^2\phi)(\tfrac{3}{2} + S^2\cos^2\phi)(1 + erf(S\cos\phi))] \quad (4.6)$$

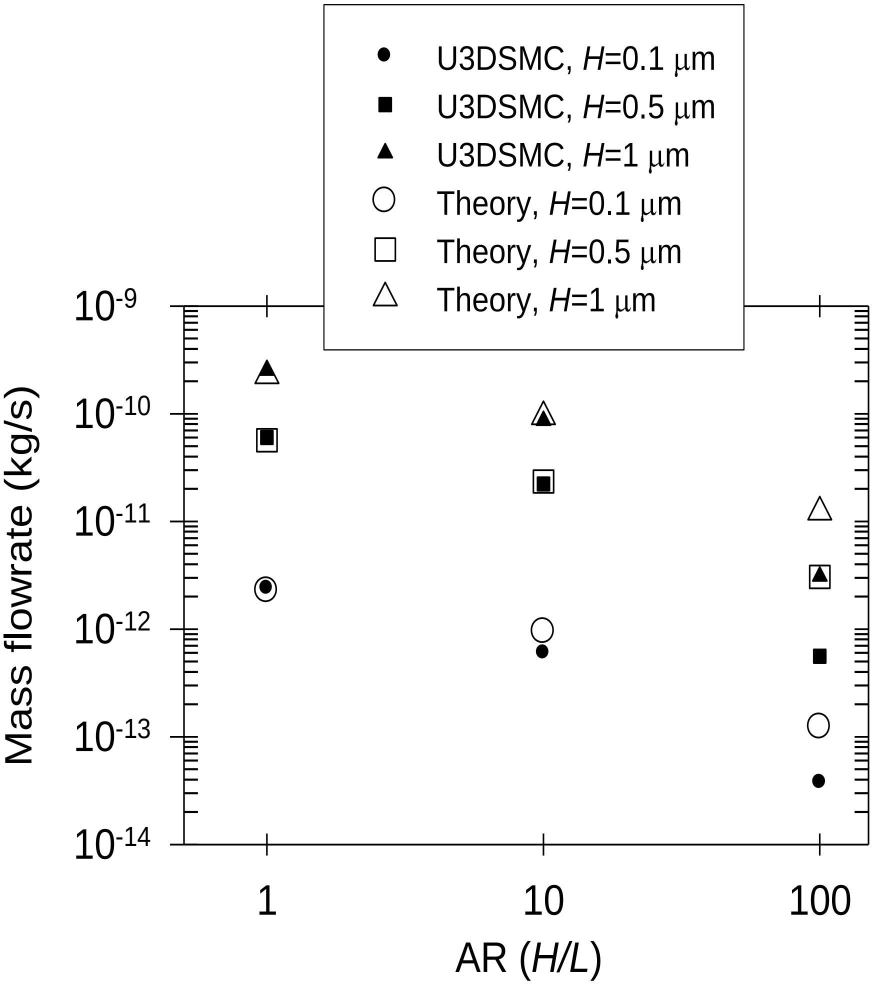

Figure 4-11. Outgoing mass flow rate at the outlet of the nanochannel. Comparison between U3DSMC and numerical results obtained from the Hughes and de Leeuw theory.

The expression in eq. (4.5) has been integrated numerically and evaluated using input parameters from the simulations in Case1-9. Comparisons are shown in Figure 4-11. For AR=1 and AR=10, the U3DSMC predictions are very close to the theoretical. For the long AR=100 nanochannels, the theoretical predictions are larger than the U3DSMC. The theory does not account for the external flow effects or the internal structure of the flow field as evident in the

U3DSCM results discussed earlier. In the case of short tubes, wall collisions are not sufficient to modify the free-stream and the theoretical results provide the outgoing flux.

4.3.2 Effects of Free Stream Speed Ratio

The free stream speed ratio can have profound effects on the flow characteristics inside a nanochannel. Simulations for $H = 0.5\mu$ and AR=10 nanochannels were performed with free stream speed ratios of $S_\infty = 2$ (Case 10), $S_\infty = 5$ (Case 5) and $S_\infty = 10$ (Case 11).

The case of $S_\infty = 2$ corresponds to $V_\infty = 805.2 \text{ m/s}$ and $M_\infty = 2.39$, the criterion for the DSMC to have that $V_\infty \Delta\tau < \lambda_\infty$ is satisfied. The case of $S_\infty = 10$ corresponds to $M_\infty = 11.95$ and $V_\infty = 4026.8 \text{ m/s}$, the criterion for the DSMC to have that $V_\infty \Delta\tau < \lambda_\infty$ is also satisfied.

In order to investigate the effects of the speed ratio on the flow, the phase-space plots including $(x - y,\ x - V_x,\ x - V_y \text{ and } V_x - V_y)$ will be analyzed as well as the heat flux to the upper wall of the nanochannels.

The (x, y) phase space in Figure 4-12 shows that the number density develops an enhancement upstream of the inlet that is more pronounced at $S_\infty = 2$. The (x, v_x) phase space shows that this backstreaming of particles in the buffer region is greatly reduced at higher speed ratios. The nanochannel is populated primarily with the low-drift population for all speed ratios considered. The (x, v_y) phase space shows that the v_y increases near the inlet, a trend that becomes more pronounced at higher speed rations. The distribution in v_y is symmetric afterwards and the spread is larger than the free stream. The formation of the low-speed population with a zero drift is depicted in the (v_x, v_y) phase space plots for three speed ratios considered.

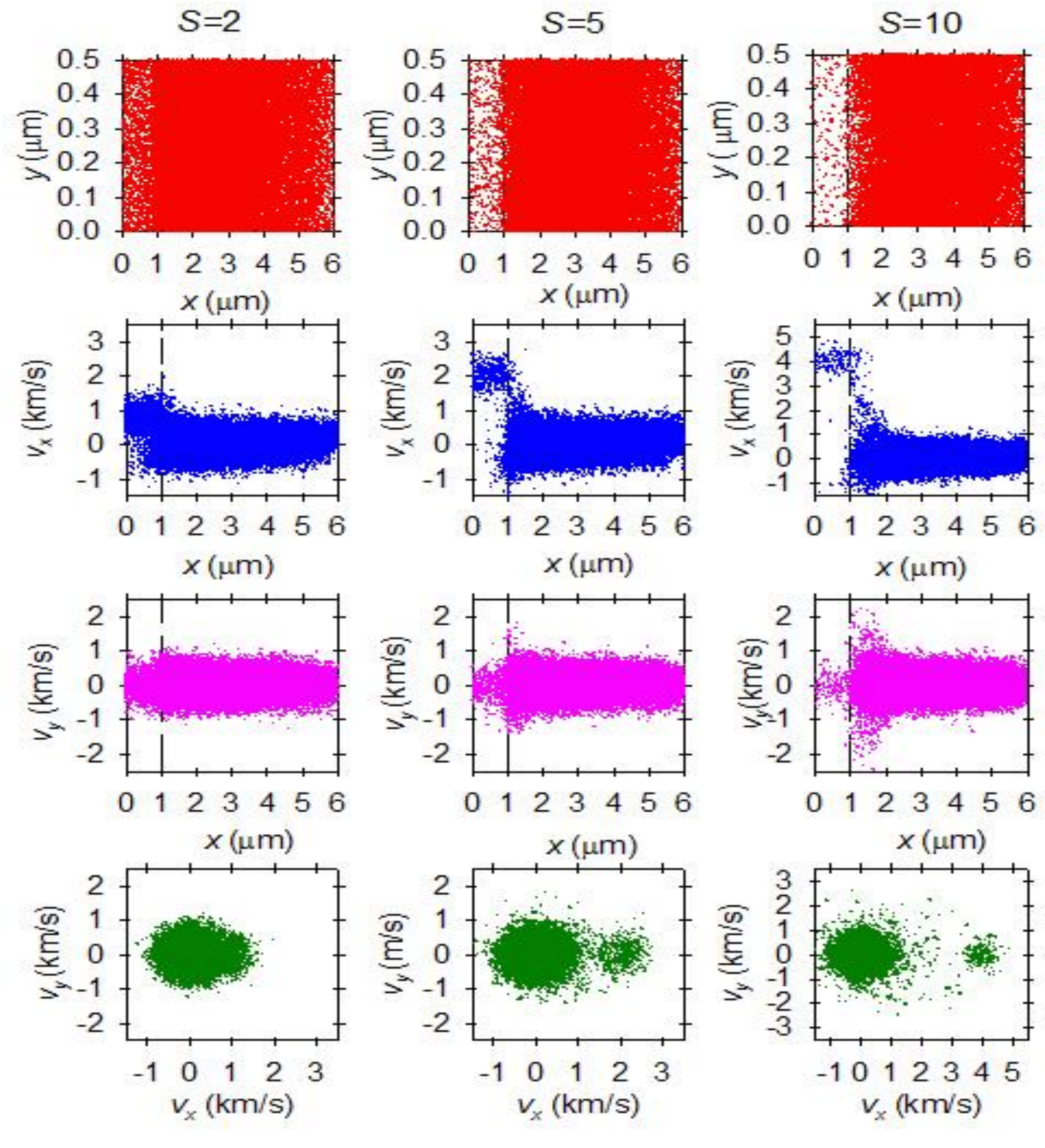

Figure 4-12. Effects of S_∞ for H=0.5 μm, AR=10. Phase plots (x,y), (x,v_x),(x,v_y) phase plots (Cases 5, 10 and 11).

The heat flux to the wall is plotted in Figure 4-13. The heat loss to the wall is confined within the inlet region of the nanochannel and is associated with the temperature enhancement that is depicted by the phase space plots in Figure 4-12. The heat loss increases with increasing S_∞, which is a direct consequence of the larger temperatures at the inlet region.

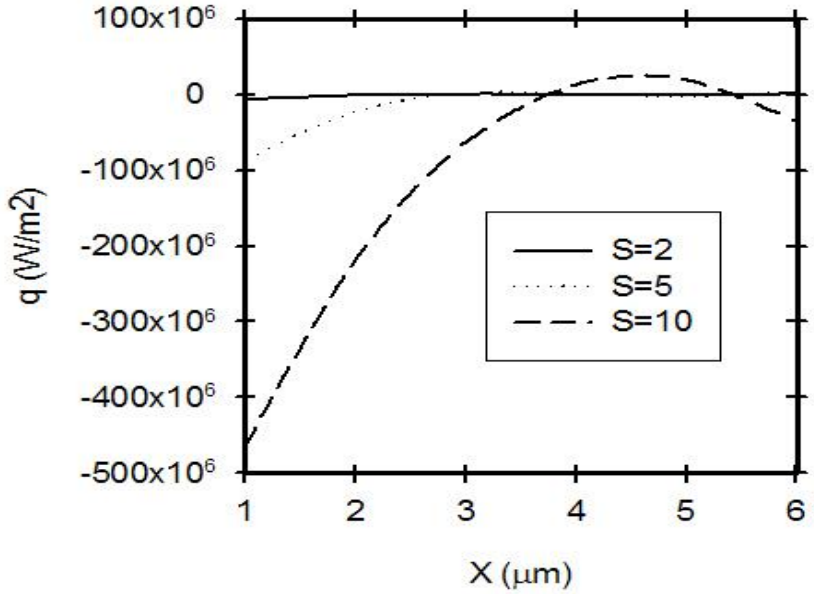

Figure 4-13. Effect of speed ratio on heat transfer for H=0.5 μm, AR=10. (Cases 5,10,11).

4.3.3 Effects of Back Pressure

The effects of back pressure are examined in simulations Case 4, 4a, 4b, 5, 5a, 5b. These simulations are performed with $H = 0.5\mu$ and AR=1 and AR=10 nanochannels with free stream speed ratio of $S_\infty = 5$ and $P_\infty = 10.13\,\text{kPa}$.

The back pressure was imposed at the exit of the nanochannel and was implemented following the subsonic outlet boundary condition based on the method of characteristics (Sec. 2.2.3.3) in which the pressure at the exit (P_e) is fixed throughout the simulations and the number density and velocity at the exit (V_e, T_e) are floating. The back pressure is in the range of 0-200 kPa, and its effects are investigated using the phase-space plots ($x-y$, $x-V_x$, $x-V_y$ and V_x-V_y), the centerline macroscopic properties (V, Ma and P), and the heat transfer fluxes to the upper wall of the nanochannel.

Figure 4-14 shows the centerline macroscopic flow properties. The $P_b = 0$ case (vacuum) shows that the pressure increases in the buffer region, reaches a maximum inside the nanochannel and reduces at the outlet to $P_e = 101{,}154$ Pa. The Mach number decreases in the buffer region but the flow remains supersonic throughout the domain and reaches $M_e = 1.48$ at the outlet. This flow yields expansion waves outside the exit. The phase plot (x, v_x) in Figure 4-15 shows that backstreaming particles fill the buffer region and result in the reduction in the average macroscopic velocity, V_x. Inside the nancochannel the low-speed population is superimposed with the free-stream supersonic population to result in a small average velocity. The (x, v_y) phase plot in Figure 4-15 shows that the v_y component is unperturbed in the buffer region but has a larger spread inside the nanochannel due to collisions. The heat flux to the wall remains nearly uniform (and negative) throughout the nanochannel. With $P_b = 120$ kPa the flow achieves $P_e = 118$ kPa at the outlet and becomes subsonic with $M_e = 0.42$. Similarly, with $P_b = 200$ kPa the flow achieves $P_e = 197$ kPa with $M_e = 0.38$. The exit pressure nearly matches the imposed back pressure in both cases. The fractional difference $\left(P_b - P_e\right) / P_b$ is less than 0.02% and results from the fact that these nodal values correspond to cell-based average sampling. These cases demonstrate the ability of the outlet boundary condition to conform to subsonic and supersonic flows.

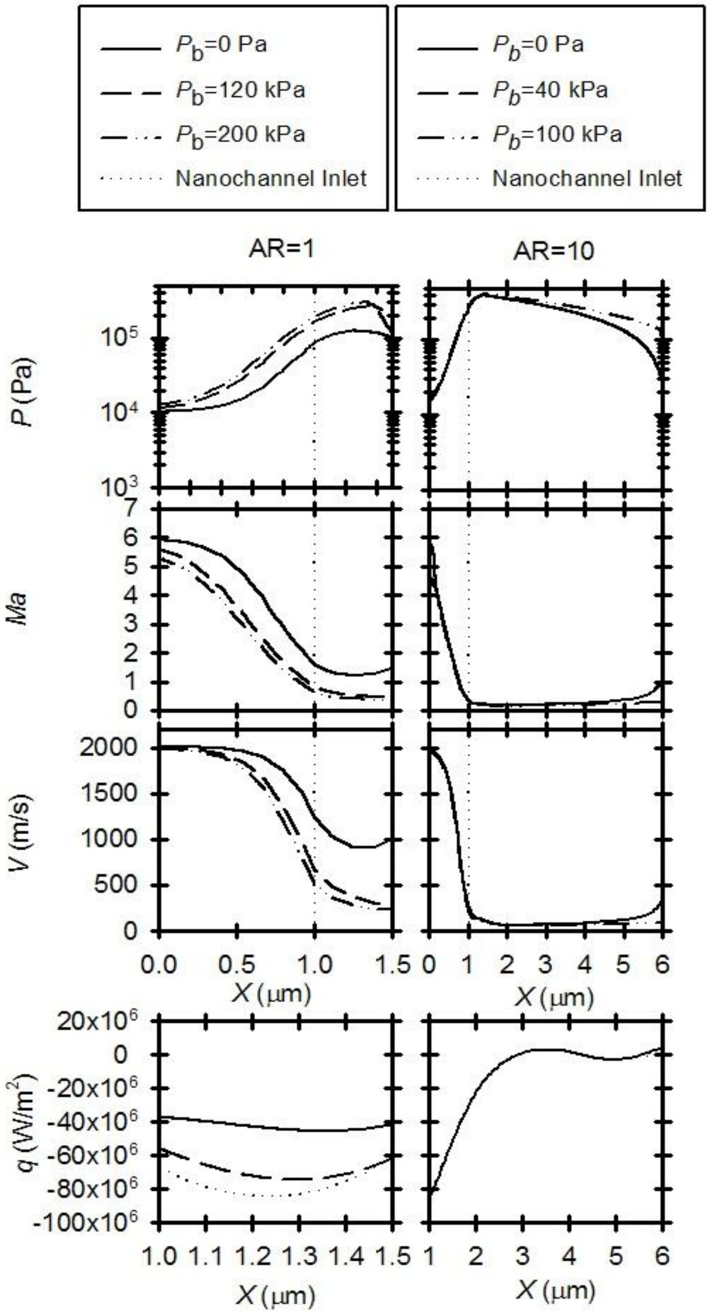

Figure 4-14 Centerline properties showing the effects of back pressure for *H*=0.5 μm AR=1(Left) and AR=10 (Right) (Cases 4,4a,4b,5,5a,5b). The inlet is indicated by the dotted line.

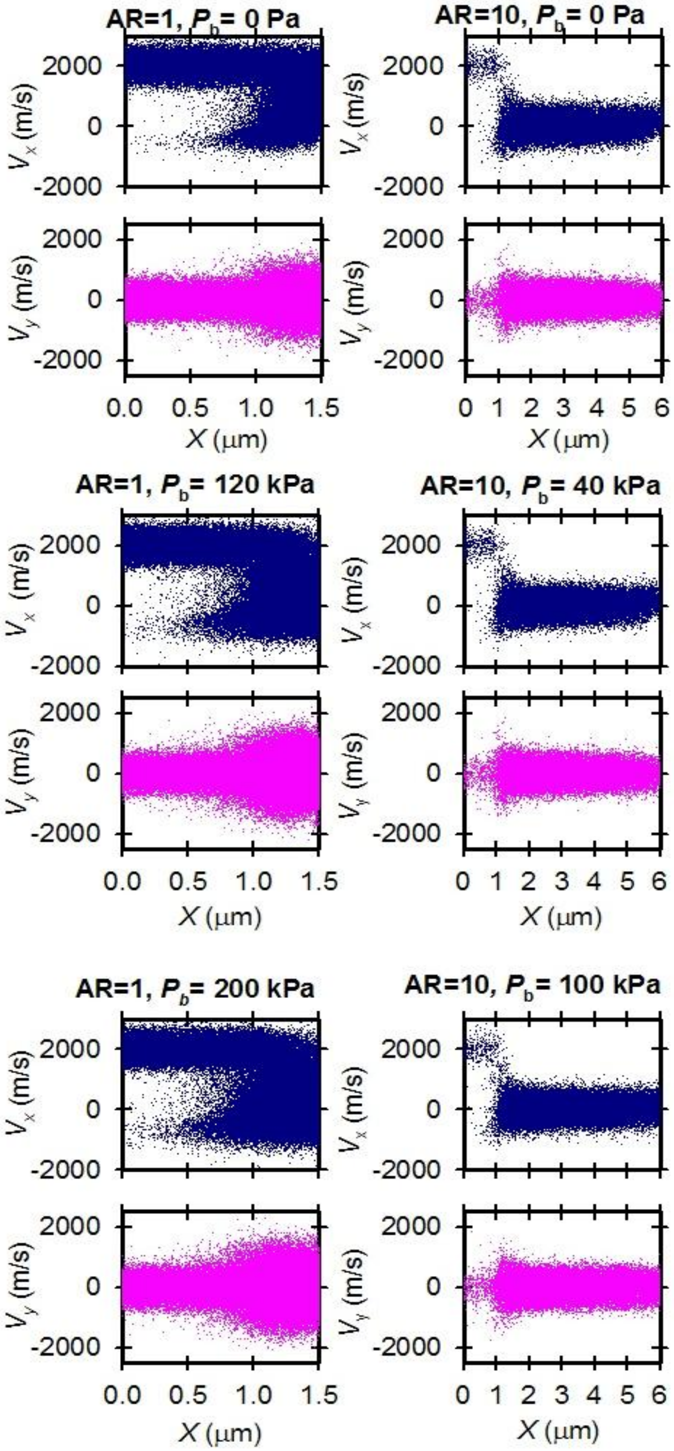

Figure 4-15. Phase plots of (x, v_x) and (x, v_y) showing the effects of back pressure for H =0.5 μm nanochannels (Cases 4, 4a, 4b and 5, 5a, 5b).

Figure 4-14 shows that the centerline macroscopic flow properties are almost identical for the vacuum and 40 kPa boundary conditions. The pressure is shown to increase in the buffer region to reach a maximum inside the nanochannel and to decrease towards the exit. With $P_b = 0$ kPa the flow achieves $P_e = 29$ kPa to become slightly supersonic with $M_e = 1.002$. Expansion waves persist outside the nanochannel. With $P_b = 40$ kPa the flow achieves $P_e = 39.7$ kPa and becomes sonic with $M_e = 1$. With $P_b = 100$ kPa the flow achieves $P_e = 102$ kPa and becomes subsonic with $M_e = 0.28$. The (x, v_x) phase plots in Figure 4-15 show that backstreaming particles fill the buffer region and result in the reduction in the average speed. Inside the long nanochannels the distribution is dominated by slow particles. Similarly, the (x, v_y) phase plots in Figure 4-15 show that the distribution remains symmetric in the buffer region, as well as inside the nanochannel. The spread in v_y increases with larger backpressure. Our results exhibit qualitative similarities with those obtained in microchannels (Liou *et al*., 2001; Le and Hassan, 2007). The heat flux to the wall is almost identical for the three back pressures considered. It is maximum (negative) in the inlet region and decreases downstream the inlet. The average velocity decreases from the inlet till the region of positive heat flux to the wall. For the remainder of the nanochannel the velocity increases to reach sonic at the outlet.

5 U3DSMC SIMULATION OF ATMOSPHERIC SUPERSONIC FLOWS INTO NANOCHANNELS

In this chapter, supersonic atmospheric flows into nanochannels are investigated using the U3DSMC method. The Knudsen numbers considered are 0.0962 and 0.481 covering the slip and transitional regimes. The heights of the nanochannels are 100 and 500 nm, the aspect ratios are 1 and 10, and speed ratios of 2, 5 and 10. Simulations consider vacuum back pressure. The study utilizes the phase-space plots resulting from the U3DSMC simulations as well as the centerline macroscopic properties including (n, T and V). Also, the heat fluxes to the upper wall of the nanochannels are obtained from the U3DSMC.

5.1 Input Conditions, Boundary Conditions and Computational Parameters

Rectangular nanochannels with $H = W = 100 - 500$ nm with AR=1, 10 are considered in the U3DSMC simulations.

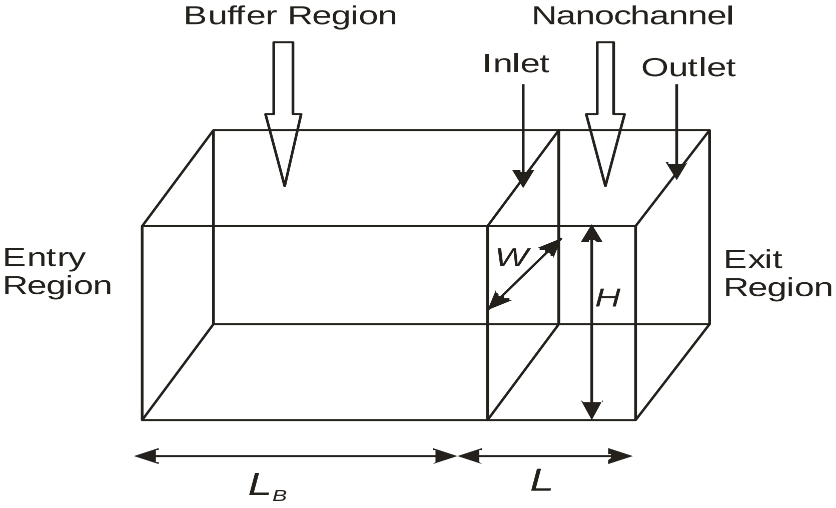

Figure 5-1. The domain used in the U3DSMC simulations (dimensions are not to scale).

Figure 5-1 shows the simulation domain as well as all the parameters used to define the nanochannel and the buffer region geometries. The incoming free stream of nitrogen N_2 has $n_\infty = 2.69 \times 10^{25}\,\mathrm{m}^{-3}$, $T_\infty = 273\mathrm{K}$, corresponding to $P_\infty = 1\,\mathrm{atm}$ and $\lambda_\infty = 48.1$ nm. The free stream velocity V_∞ is varied in the simulations so that the speed ratio spans the range of the supersonic ($S_\infty = 2$) to hypersonic ($S_\infty = 10$) flow regimes. The variation of the inlet height results in Kn_∞ that range from 0.0962 to 0.481 covering the slip to transitional regimes.

In order to allow for the undisturbed free stream conditions to be realized far from the nanochannel inlet we include a buffer region of length L_B ahead of the nanochannel inlet. Molecules are injected through the boundaries of the buffer region based on specified $n_\infty, T_\infty, V_\infty$ following the method of particle injection described in (Sec. 2.2.3).

Particles that move upstream and reach the free stream surfaces of the buffer region are removed from the computational domain. The upper and lower walls as well as the side walls of the nanochannel are modeled as fully diffuse and the temperature of the wall equal that of the free stream distribution. The outlet of the nanochannel is placed at the exit boundary of the computational domain. The back pressure in all Cases 1-6 considered is specified as $P_b = 0$ at the exit region. Any particle reaching the exit plane is removed from the domain and no particles are allowed to enter the computational domain through the exit plane. The simulation domain is loaded initially with a uniformly drifting gas based on the free stream conditions specified $n_\infty, T_\infty, V_\infty$ following the method of particle loading described in (Sec. 2.2.2).

Elastic collisions are modeled with the VHS model where we capture the dependence of the collision cross section on the translational energy (eq. (2.70)) where the temperature exponent of the coefficient of viscosity for nitrogen gas $w = 0.74$ and $d_{ref} = 4.17 \times 10^{-10}$ m. Rotational degrees of freedom are modeled using the Larsen-Borgnakke model (Sec. 2.1.6) The vibrational degrees of freedom of the nitrogen are ignored.

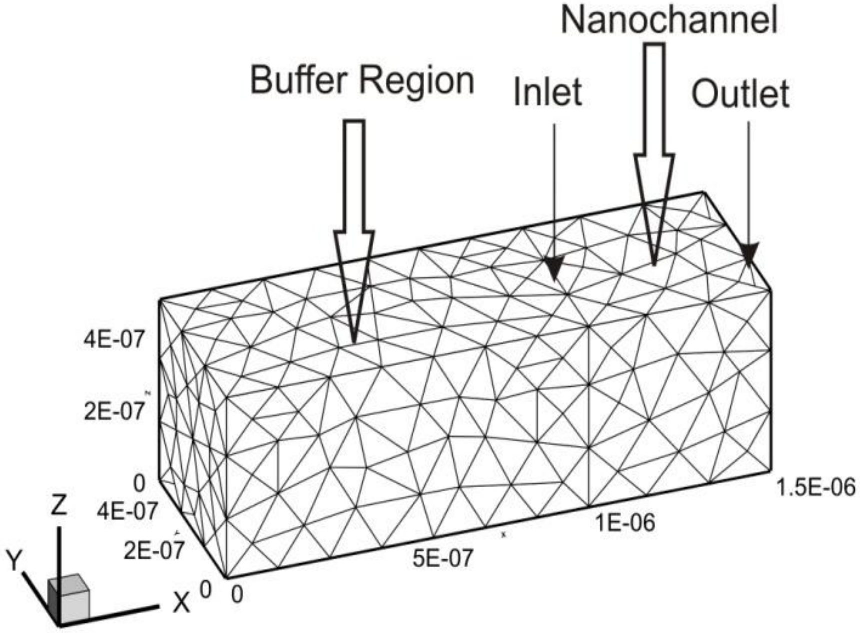

Figure 5-2.Typical grid used in U3DSMC simulations.

A typical grid used in the simulations depicted in Figure 5-2, displays the boundary faces of the Delaunay cells. The interior is discretized with Delaunay tethrahedra cells each with edge length that is smaller than λ_{∞}. The resulting averages of the Delaunay edge lengths $\langle l_D \rangle$ in Figure 5-2 show that they are smaller than the corresponding $\lambda_{\infty} = 48.1$ nm. The total number of Delaunay cells in the domain G_D, the average number of simulated particles in each cell $\langle N_D \rangle$ and its standard deviation $\sigma(N_D)$ are provided in Table 5-1. These parameters show that the Delaunay cells are populated at initialization with a least 10 computational particles.

Table 5-1. Physical and computational parameters for U3DSMC simulations of nitrogen flow.

Case	H (nm)	L/H	S_∞	M_∞	P_b (kPa)	Kn_∞	L_B (nm)	G_D	$\langle l_D \rangle$ (nm) $[\sigma(l_D)]$	F_N	$\langle N_D \rangle$ $[\sigma(N_D)]$
1	100	1	5	5.97	0	0.481	1000	1578	8.62 [0.793]	12	13.47 [3.21]
2	100	10	5	5.97	0	0.481	1000	2793	8.45 [0.775]	12	14.34 [3.11]
3	500	1	5	5.97	0	0.0962	1000	57407	11.29 [1.21]	12	14.21 [3.07]
4	500	10	5	5.97	0	0.0962	1000	57879	18.08 [2.15]	30	22.8 [5.77]
5	100	10	2	2.39	0	0.0962	1000	2793	8.45 [0.775]	12	14.34 [3.11]
6	100	10	10	11.95	0	0.0962	1000	2793	8.45 [0.775]	12	14.34 [3.11]

The simulations were run with a time step $\Delta\tau = 1 \times 10^{-12}$ sec, and the steady state time was determined from the mass flow rate obtained at the exit of the nanochannel, after reaching the steady state time, 100 independent samples were taken every 100 time steps. These 100 samples were averaged to produce the final averaged steady-state flow properties.

5.2 Results And Discussion

5.2.1 Effects of Nanochannel Inlet Size and Aspect Ratio

The inlet height determines the free stream Knudsen number and thus characterizes the rarefaction effects in the nanochannel. The nanochannel length and height determine the aspect ratio AR which will establish the flow development due to the particle-wall interactions.

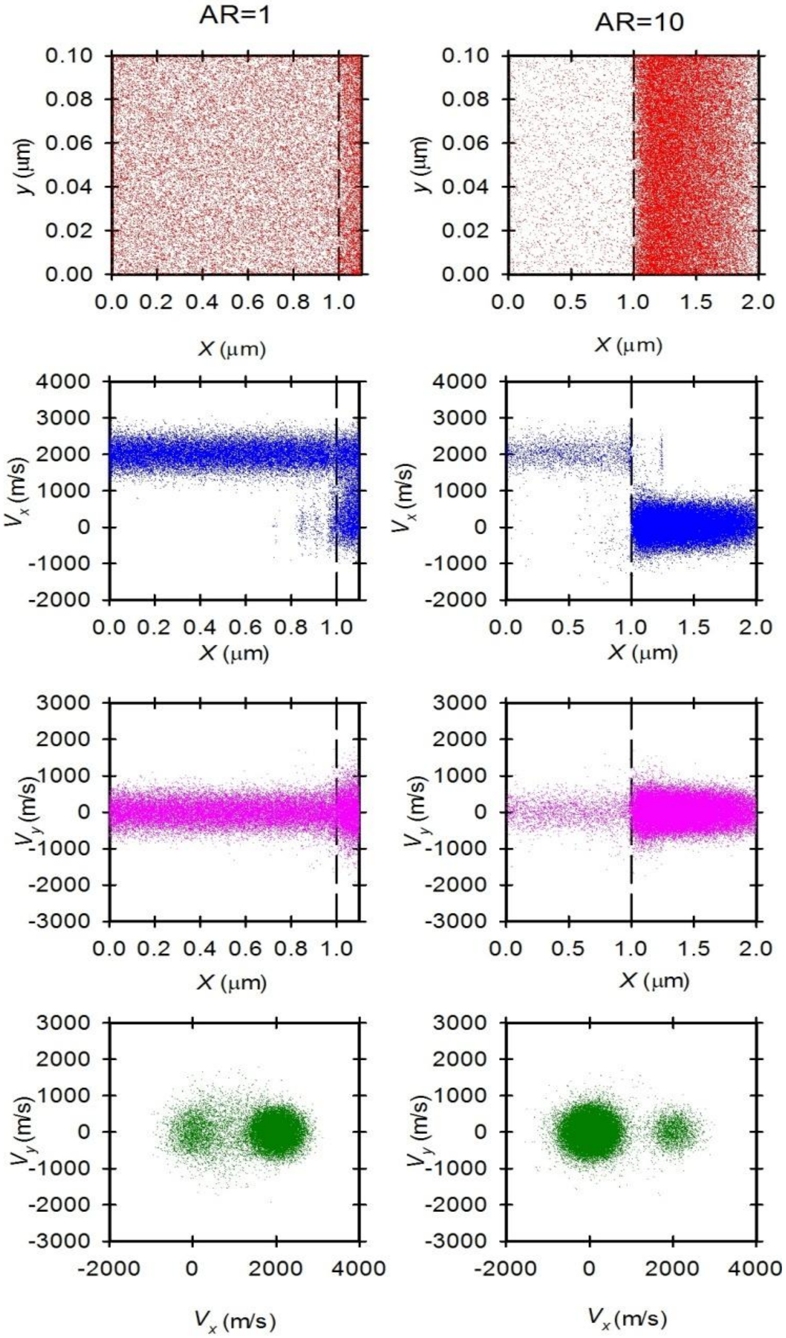

Figure 5-3. Effects of AR for *H*=0.1 μm nanochannels. Phase plots (x,y)**,** (x,v_x)**,**(x,v_y) **and** (v_x,v_y) **for Case 1, 2.**

The phase space plots for case 1 and 2 are presented in Figure 5-3. These cases simulate the narrowest nanochannels with $H = 0.1\,\mu\mathrm{m}$ and correspond to the transitional flow with a

$Kn_{\infty} = 0.481$. The (x, y) phase plot shows that there is an enhancement in the number density inside the *AR*=1 nanochannel. The long AR=10 nanonchannel shows an increase in the number density followed by a decrease at the end of the nanochannel. The (x, v_x) phase plot shows the high-speed free-stream population to permeate the entire length of the AR=1 nanochannel. The (x, v_x) plot shows a low-speed population of particles that develops inside the AR=1 nanochannel as a result of collisions of particles with the walls. In addition, a small population of up streaming particles exit the inlet after colliding with the walls or other particles in the density enhancement region. The (x, v_x) plot for the AR=10 case show that the high-speed component does not permeate the entire length of the nanochannel. Instead, the nanochannel is populated with a near zero-drift particles due to diffuse reflections of the walls. The (x, v_x) phase space shows that the spread of the v_x component is reduced towards the exit. The (x, v_y) phase plots show that the y-component of the velocity increases inside the nanochannel as a result of the collisions in the density enhancement region. As the AR increases the velocity spread decreases with increasing length, due to diffuse reflections of the walls. The (v_x, v_y) phase plots corroborates the analysis of the space-velocity phase plots. The AR=1 nanochannel show the appearance of a symmetric free-streaming population and a secondary, symmetric, zero-drift population that arise due to collisions with the wall. This zero-drift population becomes the dominant feature of the flow as the AR increases. It is also noticeable that the spread in v_y (which is an indication of the temperature) for the low-drift population is larger than the free-stream value as a result of collisions inside the nanochannel. The symmetry of the low-speed population is indicative of gas-wall equilibration phenomena inside the nanochannel.

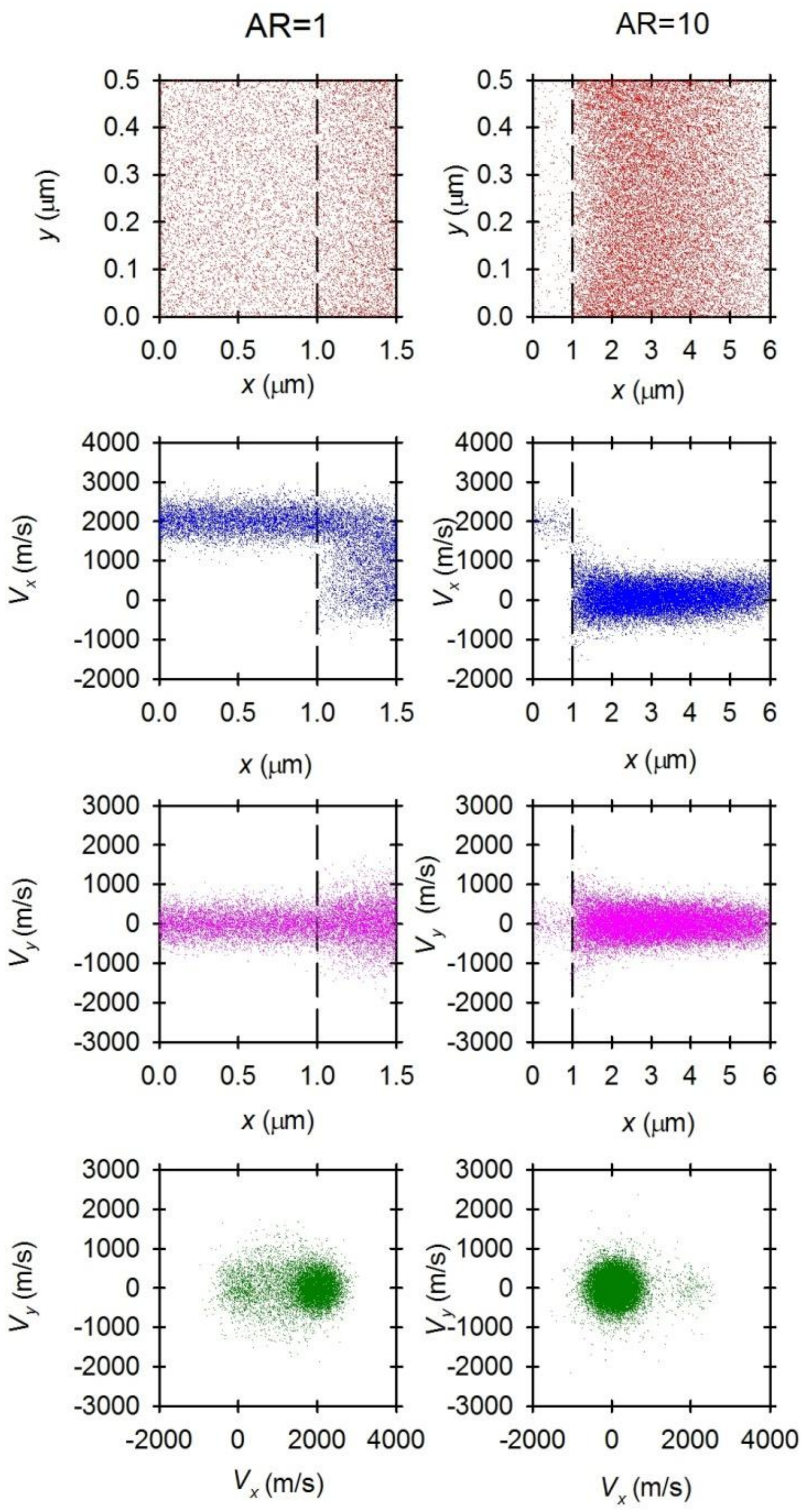

Figure 5-4. Effects of AR for *H*=0.5 μm nanochannels. Phase plots (x,y), (x,v_x),(x,v_y) and (v_x,v_y) for Case 3 and Case 4.

The phase-space plots in Figure 5-4 result from the simulations of cases 3 and 4 which represent the nanochannels with $H = 0.5\,\mu\mathrm{m}$ and correspond to the slip regime with a $Kn_\infty =$ 0.0962.

The (x, y) phase plot in Figure 5-4 shows that the number density increases inside the AR=1 nanochannel. For the AR=10 case, the density enhancement is followed by a density reduction region at the end of the nanochannel. The (x, v_x) phase plot shows the high-speed free-stream population to permeates the entire length of the nanochannel for the AR=1 case but reduces to a slow drifting population for the long AR=10 nanochannel which appears clearly inside the nanochannel and this phenomena is due to the collisions of the particles and the diffuse walls of the nanochannel. Both phase plots exhibit the upstreaming of particles in the buffer regime due to the collisions of the particles with the walls as well as other particles in the density enhancement region.

The (x, v_y) phase plots in Figure 5-4 show that the spread in v_y increases inside the nanochannel due to the collisions in the density enhancement region. For the AR=10 nanochannel, the spread in v_y gradually decreases with increasing the length of the channel. This behavior, as in the $H = 0.1\,\mu\mathrm{m}$ cases is a result of collisions with the diffuse walls of the nanochannel. The (v_x, v_y) phase plots in Figure 5-4 show that for both AR=1 and AR=10 there is a generation of a symmetric zero-drift population due to collision with the wall as well as the free-streaming population. It is also obvious that when increasing the aspect ratio then the near-zero symmetric population is becoming the dominant. The symmetry of the low speed population in the (v_x, v_y) phase plot is an indication of the gas-wall equilibration phenomena inside the nanochannel.

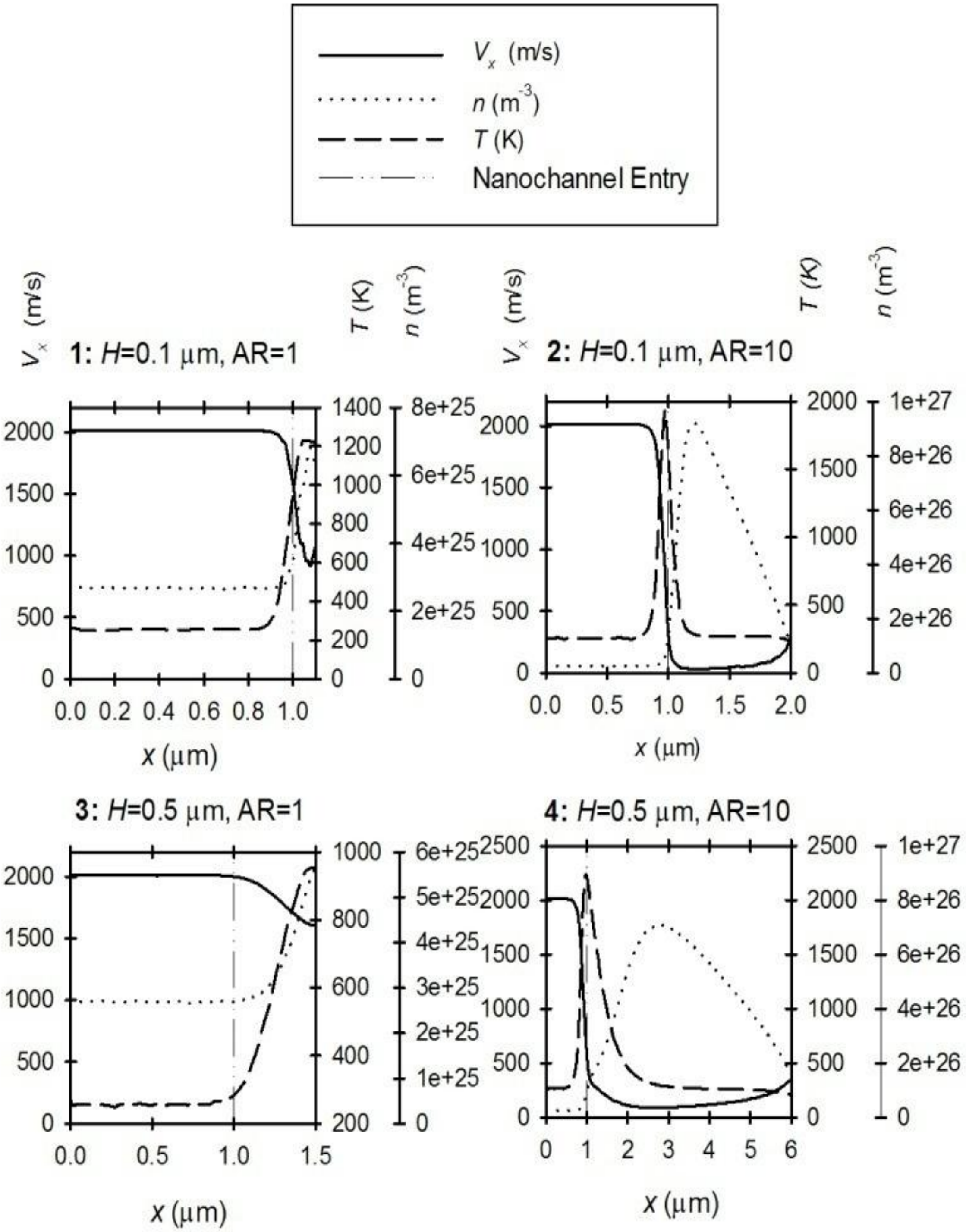

Figure 5-5. Centerline flow properties in the computational domain that includes the buffer region ahead of the nanochannel (cases 1-4).

In Figure 5-5, the sample-averaged macroscopic fluid properties obtained along the centerline of the channel are plotted. These samples are based on nodal values of the number density, n (eq.(2.73)), the average velocity V_x (eq.(2.74)) and the translational temperature T (eq.(2.77)). Figure 5-5 shows that the free stream boundary conditions are permeating inside the buffer region. The velocity decreases inside the AR=1 nanochannel and remains supersonic until the outlet. The number density increases inside the nanochannel and reaches a maximum at the outlet. The translational temperature for AR=1 shows an increase inside the nanochannel and then a slight decrease towards the exit of the channel. The longer nanochannels with AR=10 show a different behavior for these macroscopic variables. The velocity shows a drastic decrease and becomes subsonic in the inlet region of the nanochannel. As the flow moves downstream the velocity increases and becomes sonic at the outlet. The translational temperature shows a significant enhancement region near the inlet. The number density shows an increase inside the nanochannel. The location of the density maximum is downstream of the temperature maximum. The values for the centerline macroscopic properties at the exit of the nanochannel are extracted from Figure 5-5 or case 1 which corresponds to the height of 100 nm , Kn of 0.481 and AR of 1 then the centerline macroscopic properties are $n_{exit} = 6.3651 \times 10^{25}\mathrm{m}^{-3}$, $T_{exit} = 1220\mathrm{K}$, $V_{exit} = 1068\mathrm{m/s}$, for case 2, which corresponds for the height of 100 nm, AR of 10 and Kn of 0.481 then the centerline macroscopic properties are of the values of $n_{exit} = 1.2173 \times 10^{26}\mathrm{m}^{-3}, T_{exit} = 229.3\mathrm{K}$, $V_{exit} = 307.44\mathrm{m/s}$ for case 3 corresponding to a height of 500 nm, AR of 1 and Kn of 0.0962, the exit centerline macroscopic properties are $n_{exit} = 5.6897 \times 10^{25}\mathrm{m}^{-3}, T_{exit} = 953.4\mathrm{K}$, $V_{exit} = 1605.8\mathrm{m/s}$ and for case 4,where the height is

500 nm, AR of 10 and Kn of 0.0962, the exit macroscopic centerline properties are $n_{exit} = 1.67831\times10^{26}\,\mathrm{m}^{-3}, T_{exit} = 207.73\mathrm{K},\ V_{exit} = 348\mathrm{m/s}.$

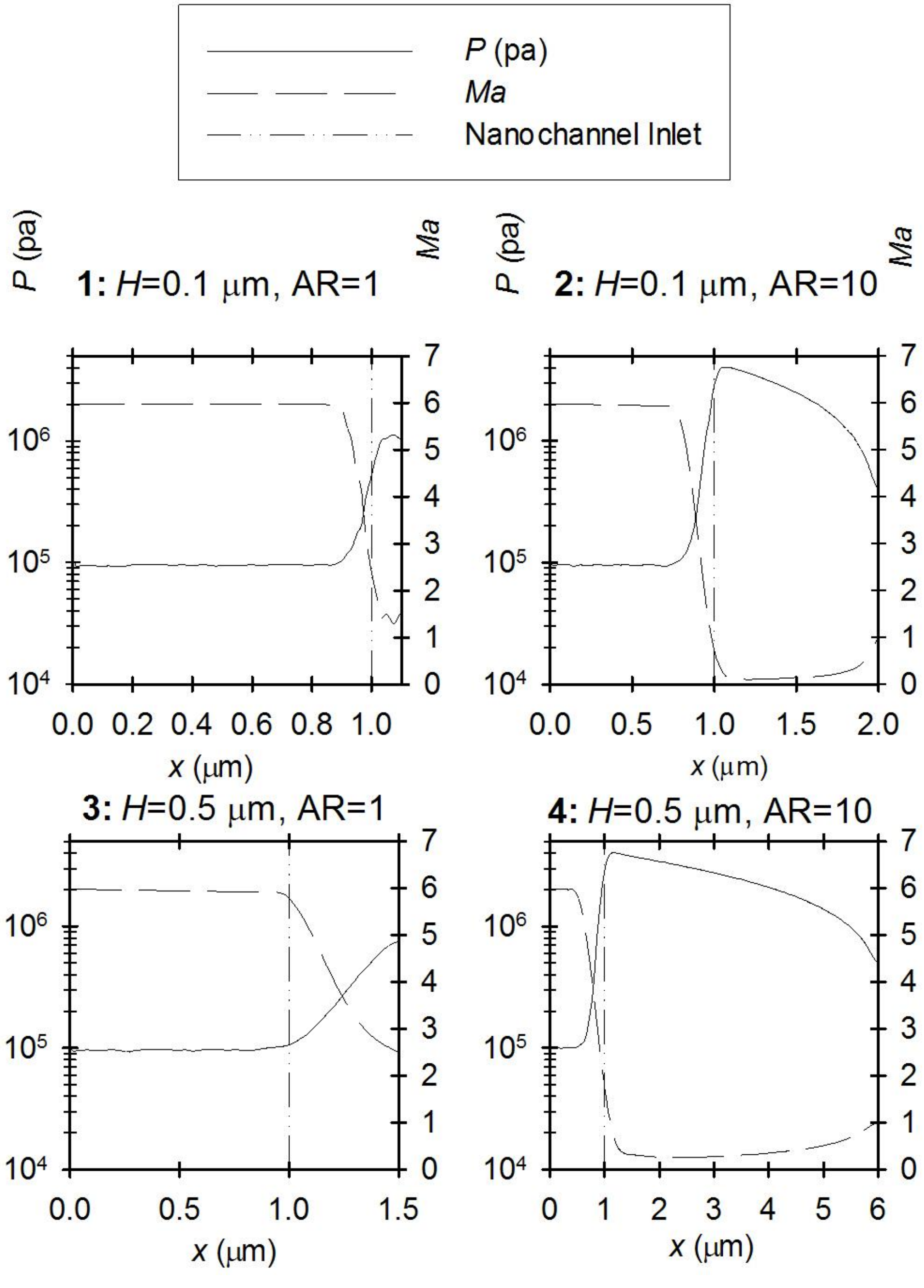

Figure 5-6. Centerline pressure and Mach number in the computational domain that includes the buffer region ahead of the nanochannel (Cases 1-4).

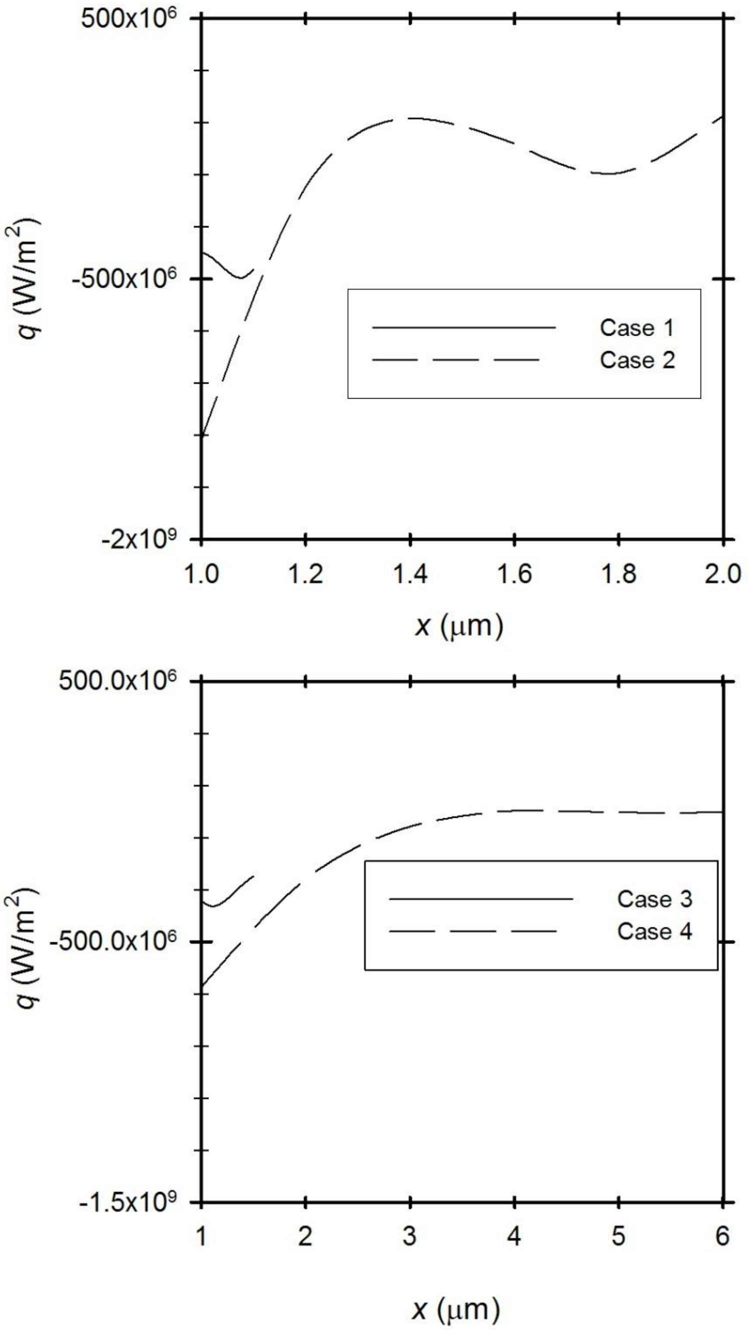

Figure 5-7. Heat flux to the wall of the nanochannel for cases 1,2,3 and 4.

In Figure 5-6, the sample-averaged centerline pressure and Mach number are plotted for Cases 1-4. The AR=1 nanochannels for the two different Knudsen numbers shows that the flow is entering the channel supersonically and remains supersonic throughout. The flow in the AR=10 nanochannels become subsonic at the inlet and reach the sonic point at the exit of the channel. The pressure increases significantly in the AR=1 nanochannels for both Knudsen numbers considered. The AR=10 nanochannels show an increase in pressure followed by a decrease inside the nanochannel. The pressure at the outlet is much larger than the free stream for all cases considered. It is very important to mention that the exit pressure never matched with the vacuum (zero pressure) in those cases, and that justifies the necessity for implementing a fixed back pressure at the exit of the channel. Also, the exit pressure as well as the exit Mach number at the centerline of the nanochannels can be extracted from Figure 5-6, for case 1, the values for P_{exit} and M_{exit} are 1016898 Pa and 1.5417 respectively, for case 2, those values are 390450 Pa and 1, case 3 will give 750551 Pa and Mach number of 2.4987 at the exit, P_{exit} and M_{exit} for case 4 are 482638 Pa and 1 respectively.

The heat flux to the constant temperature nanochannel wall is illustrated in Figure 5-7. The short nanochannels AR=1 for Cases 1 and 3 result in almost a uniform heat loss to the wall. This heat flux coincides with the temperature enhancement region that permeates these short nanodomains. Figure 5-6 shows that the flow is supersonic at the inlet and slows down at the first portion of the nanochannel due to friction and then accelerates all the way to the exit. This behavior is similar to Fanno flow at the first portion of the nanochannel and to Rayleigh flow when frictional effects are not important near the exit of the nanochannel. For the AR=10 nanochannels (Cases 2, 4), the heat flux to the wall shown in Figure 5-7 is non-uniform. It is largest (negative) in the temperature enhancement region near the inlet. The flows is subsonic for case 2 at the inlet of the nanochannel as shown in Figure 5-6 and decelerate within the region of the heat loss, consistent with the Rayleigh flow analogy. For the remainder of the nanochannel the heat flux to the wall is greatly diminished in magnitude as the fluid temperature remains almost in equilibrium with the wall as shown in Figure 5-6. The flows after the heat loss region as shown in Figure 5-5 and Figure 5-6 accelerate and become sonic at the exit. In this later region of the nanochannel the flow behavior is closer to Fanno flow, which implies that frictional effects dominate over cooling. Overall, the fluid mechanical picture that emerges from these simulations can be explained with arguments drawn from continuum, compressible viscous flows with friction and heat loss. For case 4, the flow enters the nanochannel supersonic and then decelerates to reach sonic while its temperature increases, similar to Fanno flow. The flow subsequently shows an decrease in speed and increase in temperature, in a fashion that resembles a Rayleigh flow. After that the flow accelerates with decreasing temperature, till it becomes sonic at the exit, a behavior similar to Fanno flow. The continuum fluid interpretation is corroborated by the phase plots presented in Figure 5-3 and Figure 5-4. One also can extract the values of the heat flux at the inlet and the outlet of the nanochannel for the Cases 1-4. From Figure 5-7, for Case 1, $q_{inlet} = -396967000$ W/m^2, $q_{outlet} = -396967000$ W/m^2. For Case 2, $q_{inlet} = -1123200000$ W/m^2. $q_{outlet} = -126122000$ W/m^2. The values for the heat flux at the inlet and the outlet for Case3 are $q_{inlet} = -342573000$ W/m^2, $q_{outlet} = -248741000$ W/m^2 and for Case 4, $q_{inlet} = -676075000$ W/m^2, $q_{outlet} = -3294560\ \mathrm{W/m}^2$.

5.2.2 Effects of Free Stream Speed Ratio

In order to study the effects of the free stream speed ratio on the atmospheric supersonic flows into nanochannels, simulations were performed with $S_\infty = 2$ (Case 5) and $S_\infty = 10$ (Case 6) for $H = W = 0.1$ and long AR=10 nanochannels. The analysis is based on phase-space plots ($x - y,\ x - V_x,\ x - V_y \text{ and } V_x - V_y$) as well as the heat flux to the upper wall of the nanochannel.

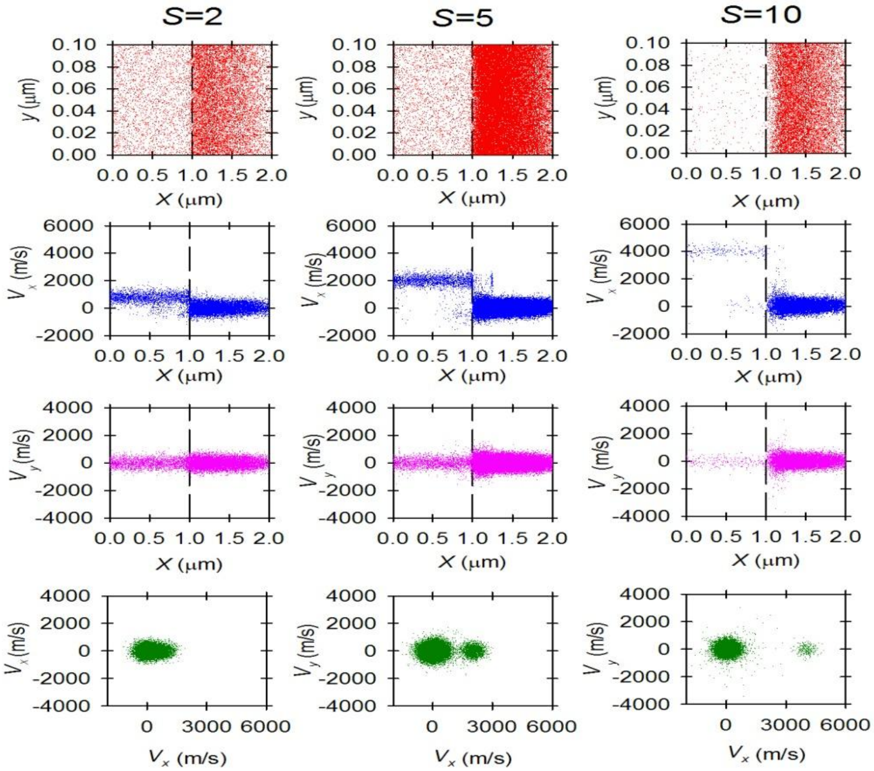

Figure 5-8. Effects of S_∞ for H=0.1 μm, AR=10. Phase plots (x, y), (x, v_x), (x, v_y) phase plots (Cases 5, 2 and 6)

Figure 5-8 shows the (x,y), (x,v_x),(x,v_y) phase plots for Case 2, 5 and 6. The density enhancement region in front of the nanochannel is diminished with increasing speed ratio. The (x,v_x) phase space show that by increasing the speed ratio the backstreaming of particles in the buffer region is greatly reduced. The (x,v_y) phase space shows that there is an increase in the spread of v_y at the inlet region which indicates an increase in the temperature near the inlet region. Also, as the speed ratio increases then this spread will be increasing and consequently the temperature near the inlet region. Generally the spread of v_y is larger in the nanochannel compared to the buffer region. Also, the spread will be decreased as the length of the nanochannel is increasing due to the diffuse reflection with the walls. In the (v_x,v_y) phase plot, one can notice that by increasing the speed ratio the low-speed population becomes the dominant feature of the flow.

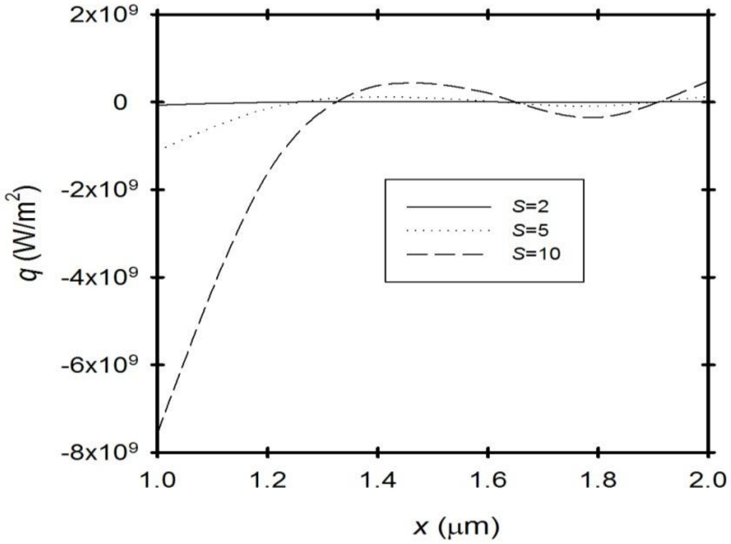

Figure 5-9. Effect of speed ratio on heat flux to the wall for *H*=0.1 μm, AR=10. (Cases 2, 5, 6) .

The heat flux to the wall is plotted in Figure 5-9. The heat loss to the wall is confined within the inlet region of the nanochannel and is associated with the temperature enhancement that is depicted by the phase space plots in Figure 5-8. The heat loss increases with increase in the free stream speed ratio. This is a direct consequence of the larger temperatures at the inlet region at elevated speed ratios.

6 SUMMARY, CONCLUSIONS AND RECOMMENDATIONS

This work addresses supersonic incoming flows into nanoscale channels applying the U3DSMC method. Nitrogen flows at atmospheric and sub-atmospheric conditions are considered, at speed ratios that range from supersonic to hypersonic, into small aspect ratio (short) and very long rectangular nanochannels. This work contributes to the computational mathematics background of U3DSMC and involves the development of formal mathematical background of the subsonic boundary conditions implemented in U3DSMC, and the analysis of fluctuations and statistical errors associated with U3DSMC applications at the nanoscale. Overall, this work provides physical insights on the rarefaction and compressibility effects of supersonic nanoflows. It also demonstrates the applicability of Bird's DSMC approach (Bird, 1994) as implemented in U3DSMC to nanoscale flows. In this chapter we summarize the approach and the conclusions obtained for each of the objectives identified in Sec. 1 of this dissertation. The chapter also provides recommendations for future work.

6.1 Summary And Conclusions

6.1.1 Verification and Validation

The U3DSMC code is validated by comparisons with previous 2D DSMC results of Liou and Fang (2001) and Le *et al*. (2007). These simulations involved supersonic nitrogen flow incoming into a microchannel with height of 1.2 μm, length 6 μm and represent the smallest scales available in the literature for comparison. The centerline temperature as well as the velocity and the heat transfer to the wall of the microchannel results obtained from the U3DSMC show an excellent agreement with these 2D simulations.

6.1.2 Subsonic Boundary Conditions in U3DSMC

The subsonic inflow and outflow method implemented in U3DSMC was developed by Chamberlin (2007) following an approach that has its roots on the method of characteristics (Whitfield and Janus, 1984; Nance et al., 1997; Liou and Fang, 2000; Wang and Li, 2004). In this dissertation, we follow Hirsch (Sec.19.1.5, 1995) and Yee at al. (1982) and derive the boundary methodology used in U3DSMC. For a subsonic inlet the two physical boundary conditions specified at the boundary are p_1 and ρ_1. In a subsonic inlet, w_1, w_2 represent the physical boundary conditions. Zero-order space and zero-order time extrapolation of the characteristic variable w_3 between the boundary point and the interior point provides the numerical boundary condition and allows the evaluation of the third primitive variable, V_1. For a subsonic outlet, w_3 is the physical boundary condition and the pressure is fixed at p_M. Zero-order space and zero-order time extrapolation of the characteristic variables and use of the numerical boundary conditions, provide the two primitive variables ρ_M and V_M. Once $n, T, \mathbf{V}$ are obtained on an inlet or outlet surface, the particles are injected into the domain following the procedure outlined in Sec. 2.1.3.

6.1.3 Statistical Fluctuations and Errors in the U3DSMC Methodology

Statistical fluctuations and errors in U3DSMC arise due to sampling of properties in order to obtain the sample-averaged macroscopic properties of a flow field. These fluctuations have added significance in micro- and nano-scale domains because the number of real particles can be very small inside a computational cell used in DSMC. The theory of fractional errors for number of particles, mean velocity, and translation temperature, presented in Hadjiconstantinou et al.

(2003) is modified and applied to the Delaunay discretization involved in U3DSMC. The effect of the number of samples, the number of computational particles in a Delaunay cell, and the Mach number on the fractional errors of density, velocity and temperature are investigated for uniform and pressure-driven flows at the nanoscale.

The uniform flow is implemented in U3DSMC by applying the free stream boundary condition of $n_\infty = 2.69 \times 10^{25}$ m^{-3}, $T_\infty = 273$, $M_\infty = 0.1,10$ in a domain that requires resolution of a characteristic length scale $L = 0.05\mu\mathrm{m}$. The corresponding $\lambda_\infty = 48.1\ \mathrm{nm}$ the average Delaunay edge-length used in the discretization is 43.8 nm. The results show that the U3DSMC numerical error is identical with the theoretical error using values obtained from the U3DSMC. The theoretical error using the real number of particles is also evaluate for comparison. The increase in number of computational particles per cell result in decrease in the fractional errors. It is also found that the increase in Mach number decreases the fractional error in mean velocity.

The pressure driven flow is implemented in U3DSMC with a nanochannel of 500 nm height, 100 nm width and $4\mu\mathrm{m}$ length. Subsonic boundary conditions are enforced, with inlet pressure $p_i = 101325$ Pa, $T_i = 273$ K and outlet pressure $p_e = 10132.5$ Pa. The numerical fractional errors are compared with the theoretical values and show very good agreement.

Overall, the analysis shows that U3DSMC simulations at nanoscales, featuring 10-20 particle per cell, result in statistical errors that are consistent with theoretical estimates.

6.1.4 U3DSMC Simulations for Sub-atmospheric Supersonic Flows Into Nanochannels

An investigation of supersonic flows of nitrogen at sub-atmospheric pressures of $P_\infty = 0.1$ atm, $T_\infty = 273$ K into rectangular nanochannels of height $H = 0.1, 0.5, 1\,\mu\mathrm{m}$ is performed using the U3DSMC code. The flows considered fall into the transitional to the near-free molecular regimes with $Kn_\infty = 0.481, 0.962, 4.81$. Through a parametric investigation we examine the geometric effects on a $S_\infty = 5$ flow by varying the aspect ratio for AR=1, 10 and 100 and applying vacuum back pressure at the outlet.

The investigation is based on the analysis of microscopic characteristics, the phase-space plots, rather than the macroscopic variables used typically in micro- and macroflows. The results show a region of disturbance upstream of the nanochannel inlet formed by the superposition of particles from the free stream and those emanating from the nanochannel. The number density shows the formation of an enhancement region near the inlet of the nanochannel. The velocity phase-space shows the formation of a low-speed population as a result of collisions with the diffusely reflecting walls. The high-speed incoming population penetrates the short nanochannels but is reduced significantly in the long nanochannels. The spread in the velocity components shows an increase in the near inlet region. The heat transfer rates (heat loss) to the wall reaches a maximum (negative) near the inlet where incoming and outgoing particles form a non-equilibrium region. The absolute value of the heat transfer rate is largest for the AR=10 nanochannel and $Kn_\infty = 0.481$. The heat loss for $Kn_\infty = 0.962$ is shown to increase with increasing S_∞. The back pressure is shown to have a significant impact on these nanoflows due to the backstreaming of slow particles from the outlet region into the nanochannel.

The macroscopic flow variables obtained through sampling in the super-Delaunay cells along the centerline, provide additional insights in the flow physics and corroborate the microscopic analysis of the phase-space. These macroscopic variables are representative of a large volume fraction of the nanochannel at each downstream position. Under vacuum back pressure the centerline velocity decreases in the buffer region from its free stream value. For $Kn_{\infty} = 0.481$, 0.962, 4.81 and AR=1 the Mach number is supersonic at the inlet and remains supersonic throughout the nanochannel. For $Kn_{\infty} = 0.481$, 0.962, 4.81 and AR=10, 100 the flow becomes subsonic at the inlet and shows a sharp increase in pressure. The Mach number, subsequently, increases and reaches the sonic point at the outlet. For $Kn_{\infty} = 0.481$, 0.962, 4.81 and AR=1 the translational temperature reaches a maximum near the inlet and decreases monotonically up to the outlet. For $Kn_{\infty} = 0.481$, 0.962, 4.81 and AR=10, 100 the translational temperature reaches a maximum near the inlet and then decreases to come in near equilibration with the wall temperature of 273 K. For $Kn_{\infty} = 0.962$, AR=1 and finite back pressure of 120 kPa or 200 kPa the outlet pressure nearly matches the imposed back pressure and the nanoflow becomes subsonic. For $Kn_{\infty} = 0.962$ and AR=10 the pressure at the outlet nearly matches the imposed back pressure with the nanoflow becoming sonic at 40 kPa and subsonic at 100 kPa.

Heat transfer rates to the wall compare very well with those obtained from analytical expressions covering the free-molecular flow regime and provide verification of the U3DSMC procedure. Furthermore, comparison of the computed outgoing particle fluxes at the outlet shows very good agreement with results from a semi-analytical model of Hughes and de Leeuw for the $Kn_{\infty} = 0.481$, 0.962, 4.81 and AR=1, 10 nanochannels. Differences between the theoretical estimates and the U3DSMC results for the AR=100 nanochannel, demonstrate that that the computations account for flow phenomena not included in the semi-analytical model.

The U3DSMC computations in this work feature a small number of real particles in the computational domain, small particle weights, and few computational cells across the width of the nanochannel. The U3DSMC results show that the supersonic nanoflows considered exhibit characteristics that are similar to previous micron- and macroscale flows covering similar Knudsen number regimes, and have physical characteristics that are found in continuous compressible, viscous channel flows with friction and heat loss. The microscopic analysis adopted in our work uses the phase-space distributions and provides the kinetic-based explanation of the obtained macroscopic flow variables. Overall, our work extends the applicability of the DSMC method to rarefied supersonic nanoflows.

6.1.5 U3DSMC Simulation for Atmospheric Supersonic Flows Into Nanochannels

An investigation of supersonic flows of nitrogen at atmospheric pressures of $P_\infty = 1$ atm, $T_\infty = 273\,\mathrm{K}$ into rectangular nanochannels of height $H = 0.1, 0.5\,\mu\mathrm{m}$ is performed using the U3DSMC code. The flows considered fall into the slip and transitional regimes with $Kn_\infty = 0.481, 0.0962$. Through a parametric investigation we examine the geometric effects on a $S_\infty = 5$ flow by varying the aspect ratio for AR=1 and 10 and applying vacuum back pressure at the outlet.

The investigation is based on the analysis of microscopic characteristics, the phase-space plots, rather than the macroscopic variables used typically in micro- and macroflows. The results show a region of disturbance upstream of the nanochannel inlet formed by the superposition of particles from the free stream and those emanating from the nanochannel. The number density shows the formation of an enhancement region near the inlet of the nanochannel. The velocity phase-space shows the formation of a low-speed population as a result of collisions with the diffusely reflecting walls. The high-speed incoming population penetrates the short nanochannels but is reduced significantly in the long nanochannels. The spread in the velocity components shows an increase in the near inlet region. The heat transfer rates (heat loss) to the wall reaches a maximum (negative) near the inlet where incoming and outgoing particles form a non-equilibrium region. The absolute value of the heat transfer rate is largest for the AR=10 nanochannel and $Kn_\infty = 0.481$. The heat loss for $Kn_\infty = 0.0962$ and AR of 10 is shown to increase with increasing S_∞.

The macroscopic flow variables obtained through volume sampling in the super-Delaunay cells along the centerline, provide additional insights in the flow physics and corroborate the microscopic analysis of the phase-space. These macroscopic variables are representative of a large volume fraction of the nanochannel at each downstream position. Under vacuum back pressure the centerline velocity decreases in the buffer region from its free stream value. For $Kn_\infty = 0.481$, 0.0962 and AR=1 the Mach number is supersonic at the inlet and remains supersonic throughout the nanochannel. For $Kn_\infty = 0.481$, 0.0962 and AR=10, the flow becomes either subsonic or supersonic at the inlet and shows a sharp increase in pressure. The Mach number, subsequently near the end of the nanochannel increases and reaches the sonic point at the outlet. For $Kn_\infty = 0.481$, 0.0962 and AR=1 the translational temperature reaches a maximum near the inlet and decreases monotonically up to the outlet. For $Kn_\infty = 0.481$, 0.0962 and AR=10, the translational temperature reaches a maximum near the inlet and then decreases to come in near equilibration with the wall temperature of 273 K.

6.2 Recommendations For Future Work

Future work should expand the envelope of nanoscale U3DSMC simulations explored in this dissertation and address outstanding issues in the field. Numerical simulations should involve investigation of supersonic in nanodomains that include:

1. Geometries such as nozzles, non-rectangular channels, and multi-channels found in MEMS and NEMS devices.
2. Gaseous mixtures that play important role in applications of MEMS and NEMS.

Further development of the U3DSMC method will allow future investigations of more complex rarefied flows. These developments include:

1. Extension of the characteristics-based subsonic boundary condition without the approximations of the current implementation to allow the first-order space and time extrapolation of the characteristics variables. The improved boundary implementation will allow a complete parametric investigation of subsonic nanoscale flows.
2. Parallelization of the UP3DSMC code in order to take advantage of the geometric flexibility of the code.

7 REFERENCES

1. Alexander, F. J., Garcia, A. L., and Alder, B. J., "Cell size dependence of transport coefficients in stochastic particle algorithms," *Phys. Fluids,* Vol. 10, No. 6, 1998, pp.1540-1542.
2. Al-Kouz, W. G. and Gatsonis, N. A., "Scale Effects on Rarefied Supersonic Flows in Nanochannels," *Proc, of the 6th International Conf. on Nanochannels, Microchannels and Minichannels,* Dartmouth, Germany, June, 2008.
3. Arkilic, E. B., Shmidt, M. A. and Breuer, K. S., "Measurement of the TMAC in Silicon Microchannels, *Rarefied Gas Dynamics,* Peking University Press, pp. 983- ,1997.
4. Arkilic, E. B., Measurement of the Mass Flow and Tangential Momentum Accommodation Coefficient in silicon Microchannels, Ph.D. Thesis, MIT, 1997.
5. Baker, L. L, Hadjiconstantinou, N.G, "Variance Reduction for Monte Carlo Solutions of the Boltzmann Equation," *Phys. Fluids*, Vol. 17, No. 6, pp.1-4. 2005.
6. Beskok, A. "Simulations and Models for Gas Flows in Microgeometries" PhD Thesis, Princeton University, 1996.
7. Bird, G. A., "Monte Carlo simulations in an engineering context," *Progr. in Astro. Aero.*, Vol. 74, 1981, pp. 239-255.
8. Bird, G. A., *Molecular Gas Dynamics and the Direct Simulation of Gas Flows,* Oxford Univ. Press, Oxford, 1994.
9. Bird, G.A., M. A. Gallis, J. R. Torczynski, and D. J. Rader, Accuracy and efficiency of the sophisticated direct simulation Monte Carlo algorithm for simulating noncontinuum gasflows, Phys. Fluids 21, 017103, 2009.

10. Borgnakke, C., and Larsen, P. S., “Statistical collision model for Monte Carlo simulation of polyatomic gas mixture,” *J. Comp. Phys.*, Vol. 18, 1975, pp.405-420.
11. Burgers, J. M., Flow Equations for Composite Gases, Academic Press, 1969.
12. Cercignani, S. and Lampis, M., *Rarefied gas dynamics*, Academic Press, New York, 1974.
13. Chamberlin, R. and Gatsonis, N. “DSMC Simulation of Microjet Expansion and the Design of a Micro Pitot Probe,” *Proc. of the 9th AIAA/ASME Joint Thermophysics and Heat Transfer Conf.*, San Francisco, CA, June, 2006 (a).
14. Chamberlin, R. and Gatsonis, N. “Numerical Modeling of Gas Expansion from Microtubes,” *Proc. of the 4th International Conf. on Nanochannels, Microchannels and Minichannels*, Limerick, Ireland, June, 2006 (b).
15. Chamberlin, R. and Gatsonis, N. “Numerical Modeling of Gaseous Expansion from Micro and Nano Nozzles,” *Proc. of the 25th Int. Symp. on Rarefied Gas Dynamics*, Saint-Petersburg, Russia, July, 2006 (c)
16. Chamberlin, R. E., and Gatsonis, N. A., “Numerical Modeling of Gas Expansion from Microtubes," *Journal of Nanoscale and Microscale Thermophysical Engineering*, Vol. 12, No. 2, pp. 170-185, 2008.
17. Chamberlin, R., *A three dimensional direct simulation Monte Carlo methodology on unstructured Delaunay grids with applications to micro and nano flows*, Ph.D. Dissertation, WPI, 2007.
18. Chapman, S. and Cowling, T., *The Mathematical Theory of Non-Uniform Gases*, Cambridge University Press, London, 1939.
19. Chen, G. and Boyd, I., “Statistical error analysis for the direct simulation Monte Carlo technique,” *Journal of Computational Physics*, Vol. 126, 1996, pp. 434-448.

20. Clausing, P., “The Flow of Highly Rarefied Gases through Tubes of Arbitrary Length,” *Ann. Physik*, Vol.5, No.12, pp. 961-973, 1932.
21. COMSOL Multiphysics User’s Guide, 1994–2007 by COMSOL AB.
22. Gad-el-Hak, M., The MEMS Handbook, CRC Press, 2002
23. Garcia, A. L., and Wagner, W., “Time step truncation error in direct simulation Monte Carlo,” *Phys. Fluids,* Vol. 12, No. 10, 2000, pp.2621-2633.
24. Garcia, A. L., “Estimating Hydrodynamic Quantities in the Presence of Microscopic Fluctuations,” *Comm. App. Math and Comp. Sci*. Vol. 1, No. 1, 2006.
25. Gatsonis, N. A., Maynard, E., and Erlandson, R. E., “Monte Carlo Modeling and Analysis of Pressure Sensor Measurements During Suborbital Flight,” *Journal of Spacecraft and Rockets*, Vol. 34, No.1, 1997, pp.83-91.
26. Gatsonis, N. A. and A. Spirkin, “A Three-dimensional Electrostatic Particle-in-Cell Methodology on Unstructured Delaunay-Voronoi Grids”, Journal of Computational Physics, Volume 228, Issue 10, 1 June 2009, Pages 3742-37613, 2009.
27. Gatsonis, N. A., Al-Kouz, W. G. and Chamberlin, R. E., “Rarefied Supersonic Flows Into Rectangular Nanochannels Using Three-Dimensional Direct Simulation Monte Carlo Computations,” *under review in the Physics of Fluids*, 2009.
28. Gombosi, T. I.**,** *Gaskinetic Theory,* Cambridge University Press, Cambridge, MA, 1994.
29. Hadjiconstantinou, N. G., “Analysis of discretization in the direct simulation Monte Carlo,” *Phys. Fluids,* Vol. 12, No. 10, 2000, pp. 2634-2638.
30. Hadjiconstantinou, N. G., Garcia, A. L., Bazant, M. Z., and He, G., “Statistical error in particle simulations of hydrodynamic phenomena,” *Journal of Computational Physics.*, Vol. 187, 2003, pp. 274-297.

31. Hammel, J., "Development of Unstructured 3-D Direct Simulation Monte Carlo/Particle-In-Cell Code and the Simulation of Microthruster Flows," M.S. Thesis, Worcester Polytechnic Institute, 2002.
32. Hammel, J., Kovalev, K., and Gatsonis, N. A., "Unstructured Adaptive Monte Carlo Simulations of Flows in Micronozzles," *Proc. of the 35th AIAA Thermophysics Conference*, Anaheim, CA, 2001.
33. Hughes, P. C. and de Leeuw, J. H., "Theory for the Free Molecule Impact Probe at an Angle of Attack," *Rarefied Gas Dynamics*, Vol. I, Academic Press, New York, 1965, pp. 653-676.
34. Incropera, F., Dewitt, D. and Bergman, T., Introduction to Heat Transfer. John Wiley and Sons, 2006.
35. John , J., and Keith, T., G., Gas Dynamics, Prentice Hall, 2006.
36. Kalos, M. H., and P.A. Whitlock, *Monte Carlo Methods, Volume 1: Basics,* John Wiley & Sons, New York, 1986.
37. Kannenberg, K. C., and Boyd, I.D., "Monte Carlo Computation of Rarefied Supersonic Flow into a Pitot Probe," *AIAA Journal*, Vol. 34, No. 1, 1996, pp. 83-88.
38. Kannenberg, K. C., and Boyd, I.D., "Three Dimensional Monte Carlo Simulations of Plume Impingement," *Journal of Thermophysics and Heat Transfer*, Vol. 13, 1999, pp. 226-235.
39. Karniadakis, G. E., Beskok, A., MICRO FLOWS Fundamentals and Simulation, Springer-Verlag, New York, 2003.
40. Karniadakis, G., Beskok, A., and Aluru, N., Microflows and Nanoflows, Springer, 2005.

41. Kovalev, K., “Development of a 2-D/3-D Unstructured Adaptive Grid Generator for Direct Simulation Monte Carlo Computations,” Master’s Thesis, Worcester Polytechnic Institute, 2000.
42. Le, M., Hassan, I., “Simulation of heat transfer in high speed microflows”, *Applied Thermal Engineering* 26,pp. 2035-2044, 2006 Le, M., Hassan, I., Esmail, E., “The effects of outlet boundary conditions on simulating supersonic microchannel flows using DSMC”, *Applied Thermal Engineering* 27,pp. 21-30, 2007.
43. Le, M., Hassan, I., Esmail, E., “The effects of outlet boundary conditions on simulating supersonic microchannel flows using DSMC”, *Applied Thermal Engineering* 27, pp. 21-30, 2007.
44. Liou, W. and Fang, Y. “Implicit Boundary Conditions for Direct Simulation Monte Carlo Methods in MEMS Flow Predictions,” *CMES*, Vol. 1, 2000, pp. 119-128.
45. Liou, W. W. and Fang, Y, *Microfluid Mechanics*, McGraw-Hill, New York, 2005.
46. Liou, W. W., Fang, Y.C., “Heat transfer in microchannel devices using DSMC,” *Microelectromechanical systems,* 10-2, pp. 274-279, 2001.
47. Mansour, M. M., Garcia, A. L., Lie, G. C., Clementi, E., “Fluctuating Hydrodynamics in a Dilute Gas,” *Physical review Letters,* Vol. 58, No. 9, pp. 874-877, 1987.
48. Mavriplis, C., Ahm, J. C., Goulard, R., Heat transfer and flow fields in short microchannels using direct simulation Monte Carlo, *Thermophysics and heat transfer*, 11-4,pp. 489-496,1997.
49. Moss, J.N., and Bird, G.A., “Monte Carlo Simulations in Support of the Shuttle Upper Atmospheric Mass Spectrometer Experiment,” *Journal of Spacecraft and Rockets*, Vol. 34, No. 1, pp. 83-91, 1997.

50. Nance, R., Hash, D., and Hassan, H., "Role of Boundary Conditions in Monte Carlo Simulations of MEMS Devices," *Proc. of the 35th Aerospace Sciences Meeting and Exhibit*, Reno, NV, 1997.
51. Oh, C.K., Oran, E.S., Sinkovits, R.S., Computations of high-speed, high Knudsen number microchannel flows, *Thermophysics and Heat Transfer*, 11-4, pp. 497-505, 1997.
52. Pong, K. C., Ho, C. M., Liu, J. Q. and Tai, Y. C., "Non-linear Pressure Distribution in Uniform Micro-channels, *ASME-FED*, Vol. 197, pp. ,1994.
53. Rubinstein, R. Y., *Simulation and the Monte Carlo method*, John Wiley & Sons, New York, 1981.
54. Schaaf, S. and Chambre, P., *Flow of Rarefied Gases*, Princeton Univ. Press, Princeton, 1961.
55. Shen, C., Fan, J. and Xie, C., "Statistical Simulation of rarefied gas flows in Micro-Channels," Journal of Computational Physics, Vol. 189, pp. 512-526, 2003.
56. Shih, J. C., Ho, C. M., Liu, J. Q. and Tai, Y. C., "Monatomic and Polyatomic Gas Flow through Uniform Microchannels," *ASME-DSC*, Vol. 59, pp.197- ,1996.
57. Spirkin, A. M., "A Three-dimensional Particle-In-cell Methodology on Unstructured Voronoi Grids with Applications to Plasma Microdevices," Ph.D. Dissertation, Worcester Polytechnic Institute, 2006.
58. Tyssanner, M. W. and Garcia, A. L., "Measurement of Fluid Velocity in Molecular simulations," *Journal of Computational Physics*, Vol. 196, pp. 173-183, 2004.
59. Wang, M. and Li, Z. "Simulations for gas flows in microgeometries using the direct simulation Monte Carlo method," *Int. Journal of Heat and Fluid Flow*, Vol. 25, 2004, pp. 975-985.

60. White, F., *Fluid Mechanics,* WCB/McGraw-Hill, Boston, 1999.

61. Whitfield, D. and Janus, J., “Three-Dimensional Unsteady Euler Equation Solutions Using Flux Vector Splitting,” *AIAA*, Paper 84-1552, 1984

62. Wu, J. S., Tseng, K. C., and Kuo, C. H., “The direct simulation Monte Carlo method using unstructured adaptive mesh and its application,” *International Journal for Numerical Methods in Fluids,* Vol. 38, 2002, pp. 351-375.

63. Yee, H. C., Beam, R. M. and Warming, R. F., “Boundary Approximations for Implicit Schemes for One-Dimensional Inviscid Equations of Gasdynamics,” *AIAA Journal,* Vol. 20, No. 9, pp. 1203-1211, 198.